universität wien

DIPLOMA THESIS/DIPLOMARBEIT

Title of the Diploma Thesis/Titel der Diplomarbeit

Hard and soft magnets and their interfaces

submitted by/verfasst von

Dipl.-Ing. Dr.techn. Soner Özcan

in partial fulfillment of the requirements for the degree of/angestrebter akademischer Grad

Magister (Mag.)

Vienna, 2016/ Wien (2016)

program code as it appears on the student record sheet/Studienkennzahl lt. Studienblatt:	A 190406412
degree programme as it appears on the student record sheet/Studienrichtung lt. Studienblatt:	Lehramtsstudium UF Mathematik UF Physik
Supervisor:	Univ. Prof. Dipl. Ing. Dr. Techn. Georg Kresse

Kurzfassung

Das Hauptarbeitsgebiet dieser Diplomarbeit war es zu zeigen, dass mit dem Programmpaket "Vienna ab initio Simulation package" (VASP) [1, 2] genaue Berechnungen der magnetischen Anisotropie für diverse bulk Materialien durchgeführt werden können. Um dies zu zeigen wurde die Substitutionslegierung $Fe_{1-x}Co_x$ für $(x = 0.0, 0.1, \ldots, 1.0)$ ausgewählt. Dies wurde Anhand von drei unterschiedlichen Modellen oder Rechnungsansätzen gezeigt. Als erstes haben wir mit der sogenannten "virtual crsytal approximation" (VCA) [3, 4, 5, 6, 7] gezeigt, dass eine Rechnung mit VASP, die in der wissenschaftlichen Literatur publizierten Ergebnisse reproduziert [8, 9, 10]. Als zweites haben wir mit einer erweiterten VCA Methode [11] auch die Ergebnisse der wissenschaftlichen Literatur reproduziert [8, 9, 10]. Diese Ergebnisse geben die Berechnungen in der Literatur wieder aber nicht die Experimentellen Werte. Aus diesem Grund wurde ein weiteres Modell zur Beschreibung der magnetischen Anisotropie der Substitutionslegierung $Fe_{1-x}Co_x$ herangezogen, nämlich die Unordnung im Kristallgitter, die mit VCA nicht erfasst werden kann, Anhand von Superzellen mit zufällig gesetzten Atomen auf Gitterplätze zu simulieren. Dafür wurden 8×16 Atom Superzellen, welche einer $2 \times 2 \times 2$ kubisch raumzentrierten Kristallstruktur entsprechen, erzeugt. Durch diese Modellierung der Unordnung im Kristallgitter konnten wir viel näher an die experimentellen Ergebnisse herankommen. Aber nicht nur das, wir konnten auch zeigen, dass wir mit dieser Superzellen Mittelungsmethode auch sogenannte "coherent potential approximation" (CPA) [12] Rechnungen überraschenderweise sehr gut wiedergeben [9]. Grundsätzlich sind CPA-Rechnungen viel besser geeignet um physikalische Eigenschaften von Legierungen zu beschreiben.
Diese Ergebnisse wurden in

- Soner Özcan, Sergii Khmelevskyi, Martijn Marsmann, Georg Kresse, "Calculation of the magnetic anisotropy with PAW method: the case study of tetragonally distorted disordered alloys $Fe_{1-x}Co_x$" submitted to *Phys. Rev. B*, x, xxx, (2016).

publiziert.
Um dieser Diplomarbeit einen Charakter von Vollständigkeit zu verleihen, wurde diese Arbeit um einige Kapitel erweitert.
Ein theoretisches Kapitel wurde den Hauptergebnissen der Dichtefunktionaltheorie gewidmet und eines der Spindichtefunktionaltheorie.
Ein Kapitel wurde dem Magnetismus da aber hauptsächlich der magnetischen Anisotropie und den Anwendungen der hart- und weichmagnetischen Materialien und deren Anwendungen gewidmet.

Zusätzlich wurde der Versuch unternommen ein phänomenologisches Modell von Néel [13] an die Superzellendaten $Fe_{1-x}Co_x$ anzupassen. Wir haben versucht mit den Anisotropiedaten der Superzellen für die Legierung mit der Konzentration $Fe_{0.125}Co_{0.875}$ phänomenologische Fitparameter L_{ij} anzupassen und diese dann zu verwenden um die Anisotropie der anderen Superzellen beschreiben zu können. Also eine Art selbstkonsistene Beschreibung zu erreichen. Dies gelang uns relativ gut.
Das letzte Kapitel ist ein kleiner Ausblick für zukünftige Arbeiten, die auf diese Arbeit aufbauen könnten.

Abstract

The main activity of this thesis was to show that it is possible to calculate the magnetic anisotropy energy of different bulk materials by using the Vienna ab initio simulation package (VASP) [1, 2]. For this purpose we have chosen the substitutional alloy $Fe_{1-x}Co_x$ for $(x = 0.0, 0.1, \ldots, 1.0)$. We have explored this using three different models or calculational approaches. First we have used the so called "virtual crsytal approximation" (VCA) [3, 4, 5, 6, 7] and reproduced the ab initio results in the scientific literature [8, 9, 10]. Secondly we have used an advanced VCA method [11] and also reproduced the numerically results of the scientific literature [8, 9, 10]. Our calculated results of the magnetic anisotropy energy with VCA and advanced VCA reproduce the scientific results but not the experimental results. For this reason, we have used another model to describe the magnetic anisotropy energy in the substitutional alloy $Fe_{1-x}Co_x$, namely a supercell method to capture the disorder in the alloy, which can not be captured with the VCA methods. In the supercell method, the atoms are randomly distributed on the lattice sites. For that we have used eight 16 atom supercells, where each supercell is a $2 \times 2 \times 2$ body centered cubic crystal lattice. With this modeling of the disorder in the alloy, we could reproduce the experimental results much better. Additionally, we could also show that with our averaging supercell method, coherent potential approximation (CPA) [12] results could be well reproduced. This result was surprising because usually CPA calculations are much more suited to describe physical quantities in substitutional alloys.
These results were published in

- Soner Özcan, Sergii Khmelevskyi, Martijn Marsmann, Georg Kresse, "Calculation of the magnetic anisotropy with PAW method: the case study of tetragonally distorted disordered alloys $Fe_{1-x}Co_x$" submitted to *Phys. Rev. B*, x, xxx, (2016).

In order to give this thesis a character of completeness, this work has been extended with several chapters.
A chapter was dedicated to the main results of density functional theory and one for the spin density functional theory.
A chapter was dedicated to magnetism but mainly to the magnetic anisotropy and to the applications of hard and soft magnetic materials.
In addition, we have made the attempt to fit our supercell data $Fe_{1-x}Co_x$ to a phenomenological model of Néel [13]. We tried to use the the anisotropy data of the supercell with the alloy concentration $Fe_{0.125}Co_{0.875}$ to fit the phenomenological parameters L_{ij} of the Néel model [13]

and use those parameters to recalculate the anisotropy data for the supercells with different alloy concentrations. We have tried to reach some kind of self-consistency. This worked quite well. The probability that this adaptation of the Néel model for the magnetic anisotropy to other alloys such as $Fe_{1-x}Si_x$ oder $Fe_{1-x}Pd_x$ is quite high.
The last chapter is a short outlook for future work that could build on this work.

Acknowledgements

Being aware that this thesis would not have been possible without the support of many people, I would like to mention at least some of them. First of all, I would like to thank my supervisor, Univ.-Prof Dr. Georg Kresse, for making this thesis possible. I would also like to express my gratitude to Dr. Martijn Marsman. I want to thank Privdoz. Dr.Dr. Sergii Khmelevskyi, who supported me very much in writing the paper.
Finally I would like to thank my family, especially my wife Adrienn and my newly born daughter Emilia and for their increasing moral support.

Contents

Chapter 1

Density functional theory, highlights

The main statement of the density functional theory (DFT) is that the ground state energy of a many-body system can be expressed as a function of the electron density. The roots of this approach go back to Thomas [14], Fermi [15], Dirac [16] and Wigner [17]. Thomas and Fermi introduced the DFT-method into quantum physics. But the prove that the energy of an $N-$electron system can be formulated as a function of the electron density $\rho(\mathbf{r})$ was provided by Hohenberg and Kohn [18, 19]. These two papers [18, 19] laid the foundation of modern DFT-methods.
Up to those two papers [18, 19] most of the calculations done on atoms and or molecules were wavefunction or semiempirical methods. However a wavefunction is not a measurable feature of an atom, molecule or bulk solid system, it is not what we call in physics an "observable", in fact there is no general agreement among many physicists what a wavefunction is [20, 21, 22, 23, 24, 25].
The electron density $\rho(\mathbf{r})$ on the other hand is not only the basis for DFT, but at the core of a whole suite of methods of regarding and studying atoms and molecules [26], and unlike the wavefunction, is measurable, e.g. by X-Ray diffraction or electron diffraction, ultra-high vacuum photoemission spectroscopy [27, 28, 29, 30, 31], ballistic electron emission microscopy / spectroscopy (BEEM/BEES) [32, 33, 34, 35, 36, 37, 38] and many more methods [39, 40].
Apart from being an experimental measurable physical quantity and being easily understood [41], the electron density has another property suitable for any method with claims to be competitive to wavefunction methods. DFT is definitely generally less accurate than the wavefunction based methods, but the DFT is often traceable where wavefunction methods fail. The electron density is a function of the position only, which means it is only a function of three spatial variables (x, y, z). The wavefunction on the other hand is a function of $4n$ coordinates, three spatial and one spin coordinate, for each electron. No matter how big the considered molecule or system is, the electron density $\rho(\mathbf{r})$ stays a function of three coordinates, while the number of coordinates in the wavefunction grows with the number of electrons.
DFT in Physics or Chemistry transforms the conventional use of quantum mechanics, in which the wavefunction plays the major role, in a form in which the electron density $\rho(\mathbf{r})$ plays the major role [42].
It should be noted that the 1998 Nobel Prize for Chemistry was awarded to John Pople [43]

for his role in the development of ab initio wavefunction methods and to Walter Kohn, for his development of DFT methods [18, 19].
DFT is not regarded as an ab initio method, because the correct mathematical form of the DFT functional is not known, in contrast to that in wavefunction methods the fundamental equation, namely the Schrödinger equation, is known. On the other hand, I would say that the Schrödinger equation is also just an approximation to model atoms, molecules and eventually matter. This statement can of course be disputed. On the other hand there is not any evidence that the many body Schrödinger equation is not as essentially exact in agreement with experiment like the wavefunction methods. However often it can not be solved. So in that sense DFT deserves to be called an ab initio method just as the wavefunction methods do.
DFT seeks to calculate all the properties of atoms and molecules from the electron density $\rho(\mathbf{r})$.
The first Hohenberg-Kohn theorem [18] says that all the properties of a molecule in the electronic ground state are determined by the ground state electron density $\rho_0(\mathbf{r})$. Consequentially, for given a $\rho_0(\mathbf{r})$ one can in principle calculate any ground state property like the ground state energy E_0.

$$E_0 = F[\rho_0(\mathbf{r})] = E[\rho_0(\mathbf{r})], \tag{1.1}$$

which means that E_0 is a functional of $\rho_0(\mathbf{r})$. In the mathematical formulation, the first Hohenberg-Kohn theorem [18] says, that any ground state property of a molecule is a functional of the ground state electron density $\rho_0(\mathbf{r})$.
The theorem says that there exists a functional, but it says nothing about the mathematical form of the functional. The essence of the theorem is that it guarantees us that there is a way to calculate molecular properties from the electron density $\rho(\mathbf{r})$. From that we can conclude that approximate functionals will give at least approximate answers.
The second Hohenberg-Kohn theorem says that any trial electron density different from the ground state density will give an energy higher or equal to the true ground state energy. The nuclear potential is called the external potential and designated by $V(\mathbf{r})$ and the the electron energy is denoted by $E_V = E_V[\rho_0(\mathbf{r})]$, which means that the E_V is a functional of the ground state density $\rho(\mathbf{r})$. So the second theorem can be stated as

$$E_V[\rho_t(\mathbf{r})] \geq E_0[\rho_0(\mathbf{r})]. \tag{1.2}$$

The trial electron density $\rho_t(\mathbf{r})$ must satisfy the conditions

$$\int \rho_t(\mathbf{r})\, d^3r = n \quad \ldots \quad n \text{ is the number of electrons in the molecule} \tag{1.3}$$

and

$$\rho_t(\mathbf{r}) \geq 0, \forall \mathbf{r}, \tag{1.4}$$

because the number of electrons per unit volume can not be negative.
A variational approach led 1965 to the Kohn-Sham equations [19], which is the basis of current DFT methods. Modern DFT calculations and the basic ideas behind the Kohn-Sham theorem can be summarized in the following way:

- Express the molecular energy as a sum of terms, only of which, a small term, involves the unknown functional.
- Use an initial guess of the electron density in the Kohn-Sham equations, this initial guess is then used to regenerate the orbitals.
- The final Kohn-Sham orbitals are then used to calculate the electron density that in turn is used to calculate the energy.

When putting all together in a mathematical form, the total energy functional is

$$E[\rho(\mathbf{r})] = T[\rho(\mathbf{r})] + E_H[\rho(\mathbf{r})] + E_{xc}[\rho(\mathbf{r})] + \int V(\mathbf{r})\rho(\mathbf{r})\, d^3r, \tag{1.5}$$

with

- $T[\rho(\mathbf{r})] \ldots$ kinetic energy,
- $E_H[\rho(\mathbf{r})] \ldots$ Hartree energy (electron-electron repulsion),
- $E_{xc}[\rho(\mathbf{r})] \ldots$ exchange and correlation energies,
- $V(\mathbf{r}) \ldots$ external potential of the ion cores.

By inserting the kinetic energy $T[\rho(\mathbf{r})]$ and the Hartree energy $E[\rho(\mathbf{r})]$ one gets

$$E[\rho(\mathbf{r})] = -\frac{1}{2}\sum_i \int \Phi_i^*(\mathbf{r})\, \nabla^2\, \Phi_i(\mathbf{r}) + \frac{e^2}{2} \iint \frac{\rho(\mathbf{r})\rho(\mathbf{r}')}{|\mathbf{r}-\mathbf{r}'|}\, d^3r\, d^3r' + E_{xc}[\rho(\mathbf{r})] + \int V(\mathbf{r})\rho(\mathbf{r})\, d^3r, \tag{1.6}$$

the first term is the kinetic energy of the N non interacting electrons with the same electron density [44],

$$\rho(\mathbf{r}) = \sum_i |\Phi_i(\mathbf{r})|^2. \tag{1.7}$$

The second term in equation (1.6) is the Coulomb interaction between two electron densities $\rho(\mathbf{r})$ and $\rho(\mathbf{r}')$, the third term contains the exchange correlation energy, the functional $E_{xc}[\rho(\mathbf{r})]$ and the last term characterizes the potential $\mathbf{r}$ which comes from the ionic cores. The units of the energy in equation (1.6) is Hartree.
The $\Phi_i(\mathbf{r})$are solutions of the one-electron Kohn Sham equation

$$H_{KS}\Phi_i(\mathbf{r}) = \left[-\frac{1}{2}\nabla^2 + \int \frac{\rho(\mathbf{r}')}{|\mathbf{r}-\mathbf{r}'|}\, d^3r' + V_{xc}(\mathbf{r}) + \int V(\mathbf{r})\, d^3r\right] \Phi_i(\mathbf{r}) = \varepsilon_i \Phi_i(\mathbf{r}), \tag{1.8}$$

where the exchange-correlation operator $V_{xc}(\mathbf{r})$ is defined as the functional derivative of the exchange correlation energy, $E_{xc}[\rho(\mathbf{r})]$

$$V_{xc}[\rho(\mathbf{r})] = \frac{\delta E_{xc}[\rho(\mathbf{r})]}{\delta \rho(\mathbf{r})}. \tag{1.9}$$

Equations (1.6) - (1.9) have to be solved iteratively, these give the structure for self consistent field (SCF) calculations.
The Kohn-Sham-formalism is here only specified for the non spin polarized case. Including spin polarization leads to the generalized form of the KS-equation [45, 46, 47, 48, 49, 50], which will be discussed in the next chapter.
The KS-equations describe the energy of an N electron system better then the Hartree-Fock (HF) method [51, 52, 53, 54, 55]. The reason for that is the consideration of the exchange correlation potential $V_{xc}[\rho(\mathbf{r})]$ as a function of the electron density in the Hamilton operator, with this we are in theory capturing all electron correlations. The only problem is that no one knows the exact mathematical form of $E_{xc}[\rho(\mathbf{r})]$ or $V_{xc}[\rho(\mathbf{r})]$.
For the exchange correlation energy there are many approximations, only the local density approximation (LDA) is presented here. If the electron density is uniform or in other words only varying very slowly with position.

$$E_{xc}^{LDA}[\rho(\mathbf{r})] = \int \rho(\mathbf{r})\varepsilon_{xc}[\rho(\mathbf{r})]\, d^3r, \tag{1.10}$$

where $\varepsilon_{xc}[\rho(\mathbf{r})]$ is the exchange-correlation energy of a homogeneous electron gas with the local density $\rho(\mathbf{r})$ [56, 57]. Than the LDA exchange-correlation energy functional $E_{xc}^{LDA}[\rho(\mathbf{r})]$ and its derivative $V_{xc}^{LDA}[\rho(\mathbf{r})]$ can be precisely calculated [58, 42]. For the exchange-part, HF calculations for a uniform electron gas with the density $\rho(\mathbf{r})$ leads to

$$\varepsilon_x^{LDA}[\rho(\mathbf{r})] = -\frac{3e^2}{4\pi}(3\pi^2\rho(\mathbf{r}))^{\frac{1}{3}}. \tag{1.11}$$

The LDA method describes binding energies relatively good [59, 60], although it is a very rough approximation.
More advanced exchange-correlation approximations not only describe the electron density locally but also take into account its gradient or slope (first derivative with respect to position). These functionals are called generalized-gradient approximation (GGA). They are also called nonlocal functionals [42, 61, 62].
Good descriptions of DFT and the implementation in the Vienna ab initio simulation package (VASP) can be found in [63, 64, 65, 2, 66].

Chapter 2

Spin density functional theory

In fact, here we will use spin density functional theorem (SDFT), which is a generalized form of the Kohn-Sham DFT [67, 68]. Within SDFT the spin up and down electron densities are treated separately. First we show a generalized form of the Hohenberg Kohn theorem [18] including the spin the of electrons [67]. Secondly a generalized version of the Kohn Sham [19] equations is introduced.
Essentially most modern DFT programs like the Vienna ab inito simulation package (VASP) [63, 65, 2, 66], the full-potential (linearized) augmented plane-wave ((L)APW) code Wien2k [69], and many more are in fact SDFT programs.
Calculations done in this work are also in the framework of the SDFT method.

2.1 Generalized Hohenberg Kohn scheme

We are starting with the Kohn Sham equations for the non spin polarized case.

$$H_{KS}\Phi_i(\mathbf{r}) = \left[-\frac{1}{2}\nabla^2 + \int \frac{\rho(\mathbf{r}')}{|\mathbf{r}-\mathbf{r}'|}\, d^3r' + V_{xc}(\mathbf{r}) + \int V(\mathbf{r})\, d^3r\right] \Phi_i(\mathbf{r}) = \varepsilon_i \Phi_i(\mathbf{r}), \qquad (2.1)$$

with

$$\rho(\mathbf{r}) = \sum_i |\Phi_i(\mathbf{r})|^2. \qquad (2.2)$$

For the generalization the external potential $V(\mathbf{r})$ is replaced by $V_{\alpha\beta}(\mathbf{r})$ and $\rho(\mathbf{r})$ by $\rho_{\alpha\beta}(\mathbf{r})$. But in fact there is no one to one relationship between $V_{\alpha\beta}(\mathbf{r})$ and $\rho_{\alpha\beta}(\mathbf{r})$ like in the non spin polarized case. Now an abbreviation for the electron electron repulsion term is introduced, which is the Hartree term in equation (2.1), namely instead of $V_H(\mathbf{r})$ we write $V_H(\mathbf{r}-\mathbf{r}')$. With this

one can write the Hamilton operator using the language of second quantization [70, 71, 72, 73].

$$H = \sum_{\alpha} \int \psi_{\alpha}^{\dagger}(\mathbf{r}) \left(-\frac{1}{2}\nabla^2 \right) \psi_{\alpha}(\mathbf{r})\, d^3r + \frac{1}{2} \sum_{\alpha\beta} \int \psi_{\alpha}^{\dagger}(\mathbf{r}) \psi_{\beta}^{\dagger}(\mathbf{r}^{'}) V_H(\mathbf{r} - \mathbf{r}^{'}) \psi_{\beta}(\mathbf{r}^{'}) \psi_{\alpha}(\mathbf{r})\, d^3r\, d^3r^{'} + \sum_{\alpha\beta} \int \psi_{\alpha}^{\dagger}(\mathbf{r}) V_{\alpha\beta}(\mathbf{r}) \psi_{\beta}(\mathbf{r})\, d^3r, \tag{2.3}$$

with $V_H(\mathbf{r} - \mathbf{r}^{'})$ being the Coulomb electron electron repulsion potential, essentially the Hartree term and $V_{\alpha\beta}(\mathbf{r})$ being a 2×2 Hermitian matrix, representing the spin dependent external potential.
The expectation value of the Hamilton operator in equation 2.3 is:

$$\langle \Psi | E | \Psi \rangle = \langle \Psi | T | \Psi \rangle + \langle \Psi | V_H | \Psi \rangle + \sum_{\alpha\beta} \int V_{\alpha\beta}(\mathbf{r}) \rho_{\alpha\beta}(\mathbf{r})\, d^3r, \tag{2.4}$$

with the density matrix $\rho_{\alpha\beta}(\mathbf{r})$ given by

$$\rho_{\alpha\beta}(\mathbf{r}) = \langle \Psi | \psi_{\beta}^{\dagger}(\mathbf{r})\, \psi_{\alpha}(\mathbf{r}) | \Psi \rangle\,, \tag{2.5}$$

from which follows that $\rho_{\alpha\beta}(\mathbf{r})$ is also Hermitian.
With the above equations (2.1) - (2.5) we can formulate the results from Barth et al. [67] as a generalized Hohenberg Kohn Theorem.

Theorem 1. *The ground state total energy is a functional of the electron spin density matrix $\rho_{\alpha\beta}(\mathbf{r})$ with the auxiliary condition that the number of electrons is conserved*

$$N = \sum_{\alpha} \int \rho_{\alpha\alpha}(\mathbf{r})\, d^3r.$$

Proof. The proof is by reductio ad absurdum.
Assume that there are two different ground states $|\Psi\rangle$ and $|\Psi^{'}\rangle$ corresponding to the Hamilton operators H and $H^{'}$. In those Hamilton operators are two external potential matrices $V_{\alpha\beta}(\mathbf{r})$ and $V^{'}_{\alpha\beta}(\mathbf{r})$ and they both give the same electron density matrix $\rho_{\alpha\beta}(\mathbf{r})$. From which follows

$$\langle \Psi | H | \Psi \rangle < \langle \Psi^{'} | H | \Psi^{'} \rangle = \langle \Psi^{'} | H^{'} | \Psi^{'} \rangle + \langle \Psi^{'} | H - H^{'} | \Psi^{'} \rangle\,, \tag{2.6}$$

or

$$E < E^{'} + \sum_{\alpha\beta} \int \left[V_{\alpha\beta}(\mathbf{r}) - V^{'}_{\alpha\beta}(\mathbf{r}) \right] \rho_{\beta\alpha}(\mathbf{r})\, d^3r. \tag{2.7}$$

Interchanging primed and unprimed quantities ($\rho^{'}_{\alpha\beta}(\mathbf{r}) = \rho_{\alpha\beta}(\mathbf{r})$)

$$E^{'} < E + \sum_{\alpha\beta} \int \left[V^{'}_{\alpha\beta}(\mathbf{r}) - V_{\alpha\beta}(\mathbf{r}) \right] \rho^{'}_{\beta\alpha}(\mathbf{r})\, d^3r. \tag{2.8}$$

adding equations (2.7) and (2.8), one gets:

$$E + E^{'} < E^{'} + E, \tag{2.9}$$

which is impossible and therefore the starting assumption that $|\Psi\rangle$ and $|\Psi^{'}\rangle$ are different is false. □

This proof can than be used to create generalized Kohn-Sham equations for spin systems.

2.2 Generalized Kohn-Sham equations

Like in the original paper of Kohn and Sham [19] we use the minimal property of the functional

$$\langle\Psi|H|\Psi\rangle < \langle\Psi^{'}|H|\Psi^{'}\rangle + \sum_{\alpha\beta}\int V_{\alpha\beta}(\mathbf{r})\rho_{\alpha\beta}(\mathbf{r})\,d^3r, \tag{2.10}$$

with the constraint

$$N = \sum_{\alpha}\int \rho_{\alpha\alpha}(\mathbf{r})\,d^3r, \tag{2.11}$$

which gives

$$V_{\alpha\beta}(\mathbf{r}) + \sum_{\gamma}\int \rho_{\gamma\gamma}(\mathbf{r}^{'})V_H(\mathbf{r}-\mathbf{r}^{'})\,d^3r^{'}\,\delta_{\alpha\beta}(\mathbf{r}) + \frac{\delta T_0}{\delta\rho_{\alpha\beta}(\mathbf{r})} + \frac{\delta E_{xc}}{\delta\rho_{\alpha\beta}(\mathbf{r})} = \lambda\,\delta_{\alpha\beta}(\mathbf{r}), \tag{2.12}$$

with $\delta_{\alpha\beta}(\mathbf{r})$ being the Kronecker delta and $\frac{\delta}{\delta\rho_{\alpha\beta}(\mathbf{r})}$ being the first Variation with respect to $\rho_{\alpha\beta}(\mathbf{r})$. T_0 is the kinetic energy functional for a system of noninteracting Fermi particles, E_{xc} is defined from the relation

$$T + V = T_0 + V_C + E_{xc}, \tag{2.13}$$

with V_C being the classical Coulomb energy. The constant λ is the Lagrange parameter associated with the auxiliary condition $N = \sum_\alpha \int \rho_{\alpha\alpha}(\mathbf{r})$, namely the particle conservation.
The electron density matrix $\rho_{\alpha\beta}(\mathbf{r})$ can be calculated by solving the coupled set of one particle Schrödinger equations:

$$\sum_{\beta}\left[-\frac{1}{2}\nabla^2\,\delta_{\alpha\beta}(\mathbf{r}) + \sum_{\gamma}\int \rho_{\gamma\gamma}(\mathbf{r}^{'})V_H(\mathbf{r}-\mathbf{r}^{'})\,d^3r^{'}\,\delta_{\alpha\beta}(\mathbf{r}) + V_{\alpha\beta}(\mathbf{r}) + \frac{\delta E_{xc}}{\delta\rho_{\alpha\beta}(\mathbf{r})}\right]\Phi_{\beta}^{(i)}(\mathbf{r}) = E^{(i)}\,\Phi_{\beta}^{(i)}(\mathbf{r}), \tag{2.14}$$

and then summing up all the $\Phi_{\beta}^{(i)}(\mathbf{r})$ up to the Fermi energy

$$\rho_{\alpha\beta}(\mathbf{r}) = \sum_{E^{(i)}<E_F}\Phi_{\alpha}^{(i)}(\mathbf{r})\Phi_{\beta}^{(i)*}(\mathbf{r}). \tag{2.15}$$

Above procedure is a perfectly well defined and exact way to calculate the electron density matrix. The only drawback like in the non spin polarized case is that no one knows the exact

form of $E_{xc}[\rho_{\alpha\beta}(\mathbf{r})]$ nor the exact form of the exchange correlation potential $V_{xc}^{\alpha\beta}(\mathbf{r})$, which is defined as the first variation with respect to the electron density matrix:

$$V_{xc}^{\alpha\beta}(\mathbf{r}) = \frac{\delta E_{xc}}{\delta \rho_{\alpha\beta}(\mathbf{r})}. \tag{2.16}$$

One way to obtain a reasonable approximation for the exchange correlation energy E_{xc} is to assume that the external potential is varying slowly [67]. With this assumption it is possible to divide the electronic system into small boxes in which the electrons form a spin polarized homogeneous electron gas with spin up and spin down densities, $\rho_{\uparrow}(\mathbf{r})$ and $\rho_{\downarrow}(\mathbf{r})$. $\rho_{\uparrow}(\mathbf{r})$ and $\rho_{\downarrow}(\mathbf{r})$ are given by the eigenvalues of the electron density matrix $\rho_{\alpha\beta}(\mathbf{r})$. Let's say $\varepsilon_{xc}(\rho_{\uparrow}(\mathbf{r}), \rho_{\downarrow}(\mathbf{r}))$ is the exchange correlation energy per particle of a spin polarized electron gas, then for the electronic system in the limit of slowly varying electron density, the exchange correlations energy is [67]:

$$E_{xc}[\rho_{\alpha\beta}(\mathbf{r})] = \int \left\{\rho_{\uparrow}(\mathbf{r}) + \rho_{\downarrow}(\mathbf{r})\right\} \varepsilon_{xc}[\rho_{\uparrow}(\mathbf{r}), \rho_{\downarrow}(\mathbf{r})] \; d^3r. \tag{2.17}$$

By choosing a local coordinate system with the z-axis along the direction of the local spin $\sum_{\alpha\beta} \sigma_{\alpha\beta}^{(i)} \rho_{\alpha\beta}(\mathbf{r})$, one gets with equations 2.16 and 2.17:

$$V_{xc}^{(\alpha)}(\mathbf{r}) = \frac{\partial}{\partial \rho^{(\alpha)}} \left\{\left(\rho_{\uparrow}(\mathbf{r}) + \rho_{\downarrow}(\mathbf{r})\right) \varepsilon_{xc}[\rho_{\uparrow}(\mathbf{r}), \rho_{\downarrow}(\mathbf{r})]\right\}. \tag{2.18}$$

$\sigma_{\alpha\beta}^{(i)}$ is the cartesian component of the Pauli spin vector operator.

Chapter 3

Magnetism

This thesis is not an introduction in magnetism instead of this, the goal of this chapter is to get a better understanding of the mechanism called the anisotropy. Additionally, we aim to discuss the difference between hard and soft magnetic materials and give some overview about applications of magnetic materials. There are several outstanding textbooks on magnetism, e.g [74, 75, 76, 77, 78], and many more.

3.1 Magnetic anisotropy energy

Magnetic anisotropy energy arises in ferromagnetic materials, because magnetization does not have to be necessarily parallel to the applied field. Magnetization and applied field are parallel when the field is applied to the direction of the so called easy axes of the magnetization. In ferromagnetic or antiferromagnetic materials these axes lie along some fixed directions. In Figure 3.1 such a situation is depicted.

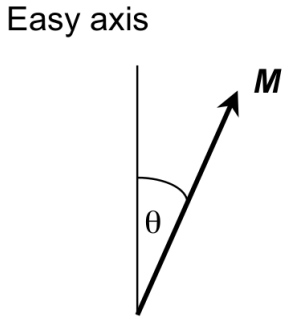

Figure 3.1: The direction of the magnetization $\mathbf{M}(\mathbf{r})$ in a ferromagnetic domain, the easy axis and the angle between them is shown.

The magnetic anisotropy has three sources:

- Shape anisotropy (is not an intrinsic property of the material).

- Magnetocrystalline anisotropy.
- Induced anisotropy, due to stress of field annealing.

The magnetocrystalline anisotropy is an intrinsic property. The magnetization is different when the field is applied to a different crystallographic directions, which means that the magnetocrystalline anisotropy could be seen as a reflection of the crystals symmetry. Its origin lies in the crystal-field interaction, spin-orbit coupling, and or in the interatomic dipole-dipole interaction [74, 75, 76, 77, 78, 79]. For us the most important anisotropy type is the magnetocrystalline anisotropy which will be discussed in more detail in this work. For the other types of anisotropy see [74, 75, 76, 77, 78, 79].

3.1.1 Magnetocrystalline anisotropy

The free energy of an undisturbed ferromagnetic crystal depends on the direction of the spontaneous magnetization with respect to the crystal axes.

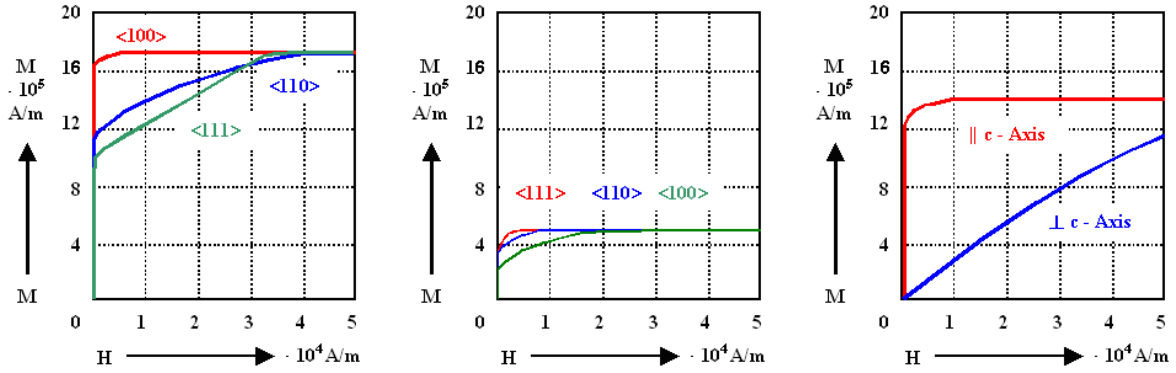

Figure 3.2: From left to right: magnetization curves of Fe, Ni and Co single crystals measured in the easy and hard directions. This picture is taken from [80].

In Figure 3.2, the dependency of the magnetization of the crystallographic directions for Fe, Ni and Co is plotted, the magnetization plots of Figure 3.2 are taken from [80]. One can see clearly that some directions are preferred, these are the directions with the highest magnetization. These are the so called easy directions of anisotropy, these are also the directions in which the free energy has its smallest values. The easy direction for Fe is $[100]$, $[111]$ for Ni and $[0001]$ (this is the hexagonal axis, the c-direction) for Co respectively.

Crystal energy function

The crystal energy function is a crystal energy density, and has units crystal energy per volume [79, 40]. We make no distinction between a crystal under stress and a crystal with a constant crystal shape. Constant crystal shape means here, no change in length and shape of the crystal.

The crystal energy function is denoted by F_K and is a function of the crystallographic directions $\alpha_1, \alpha_2, \alpha_3$ of the spontaneous magnetization.

$$F_K = F_K(\alpha_1, \alpha_2, \alpha_3). \tag{3.1}$$

In the above equation (3.1) $\alpha_1, \alpha_2, \alpha_3$ are the cosines of the angles with respect of the three cartesian directions of the spontaneous magnetization. Up to now there is no satisfying theory for the crystal energy. One can only say that the function F_K has to have the symmetry of the crystal. A mathematical formulation one can get by making a power series ansatz. This ansatz can only have even powers of the α_i, because crystallographic equivalent directions are also energetic equivalent.

Cubic crystals

In cubic crystals, the expression of the crystal energy function F_K has to satisfy two restrictions:

- The expression must contain only even-power terms of the direction cosines $\alpha_1, \alpha_2, \alpha_3$ of the spontaneous magnetization.
- It must be invariant for any interchange of the α_i among themselves.

$$\alpha_1^2 + \alpha_2^2 + \alpha_3^2 = 1, \tag{3.2}$$

With the relation

$$(\alpha_1^2 + \alpha_2^2 + \alpha_3^2)^2 = 1 = \alpha_1^4 + \alpha_2^4 + \alpha_3^4 + 2(\alpha_1^2\alpha_2^2 + \alpha_2^2\alpha_3^2 + \alpha_3^2\alpha_1^2), \tag{3.3}$$

one obtains the form of the crystal energy function for cubic crystals as follows:

$$F_K = K_0 + K_1(\alpha_1^2\alpha_2^2 + \alpha_2^2\alpha_3^2 + \alpha_3^2\alpha_1^2) + K_2\alpha_1^2\alpha_2^2\alpha_3^2 + \ldots \tag{3.4}$$

Equation 3.4 is a long known expression [81, 82] of the crystal energy function for cubic crystals. Terms of higher order than in Equation 3.4 are usually not necessary for describing experimental results.

Hexagonal crystals

Crystal energy function of hexagonal crystals have the following form

$$F_K = K_0 + K_1 \sin^2\varphi + K_2 \sin^4\varphi + K_3 \sin^6\varphi + K_4 \sin^4\varphi \cos^6\psi \quad , \tag{3.5}$$

φ is the angle between the magnetization and the hexagonal axis $[0001]$ and ψ is the angle between the magnetization and one of the hard axis $[1000]$ [83]. Equation 3.5 can for example be used for the magnetic anisotropy properties of pyrrhotite ($Fe_{1-x}Sx$). Whereas for hexagonal Cobalt there is almost no anisotropy in the basal plane, $[1000]$ and $[0100]$. So the crystal energy is only a function of φ and for most cases the F_K becomes

$$F_K = K_0 + K_1 \sin^2\varphi + K_2 \sin^4\varphi \quad . \tag{3.6}$$

Tetragonal crystals

For tetragonal crystals like for example Mn_2Sb [84] the crystal energy function has the form

$$F_K = K_0 + K_1 \sin^2\theta + K_2 \sin^4\theta + K_3 \cos^2\alpha \cos^2\beta \quad . \tag{3.7}$$

With θ being the angle between the magnetization and the tetragonal axis $[001]$ and α and β are the angles between the magnetization and the other axes $[100]$ and $[010]$.

3.1.2 Magnetic anisotropy calculations within the PAW method using VASP

The magnetocrystalline anisotropy energy (MAE) can be calculated with the VASP program. The MAE can be determined using the so called magnetic force theorem [85, 86], by running a fully self-consistent calculation for the collinear case and in the second step freezing the potential charge density for different orientations of the magnetization and then taking the energy differences, $K_u = E^{[100]} - E^{[001]}$, where $E^{[100]}$ and $E^{[001]}$ are the energies with the magnetization in the $[100]$ and $[001]$ directions of the bct structure respectively.

3.2 Hard and soft magnetic materials

3.2.1 Ferromagnetic hysteresis loop

The hysteresis loop shows the response of a ferromagnet to a magnetic field. The hysteresis loop of a magnetization curve is irreversible, it can be seen as the nonlinear response of a ferromagnet to a magnetic field. It reflects the arrangement of the magnetization in ferromagnetic domains [80]. The ferromagnetic material cannot be in thermodynamic equilibrium anywhere around the open part of the hysteresis curve.

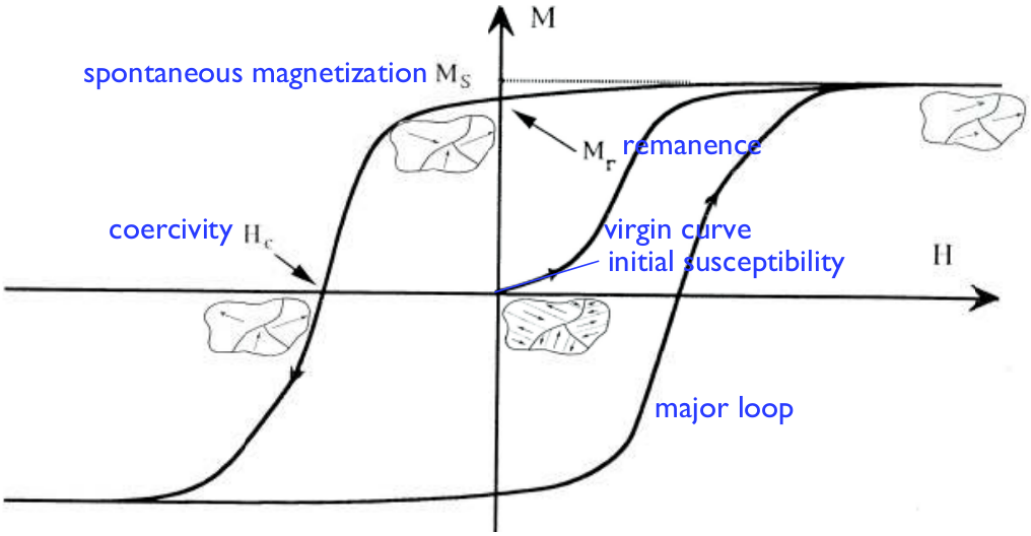

Figure 3.3: The hysteresis loop of a ferromagnetic material, it shows the irreversible, nonlinear response of a ferromagnet to a magnetic field. The Magnetization $\mathbf{M}$ and the magnetic field $\mathbf{H}$ have the same units $[\frac{A}{m}]$. This picture is taken from [80].

Starting from the thermally-demagnetized state, the following magnetization processes are involved around the hysteresis curve:

- virgin curve, reversible wall motion,
- irreversible wall motion,
- coherent rotation, reaching spontaneous or saturation magnetization M_S,
- passing remanence M_r
- nucleation, irreversible wall motion, passing coercivity H_c.

In bulk material it is practically impossible to calculate the exact values of the hysteresis and the coercivity [74, 79, 75, 76, 77, 78].

3.2.2 Hard magnetic materials

Hard magnetic materials are ferromagnets with a wide hysteresis loop. The name hard comes from the fact, that these kind of magnetic materials need higher magnetic fields to get magnetized, unlike the soft magnetic materials, they get magnetized very easy.

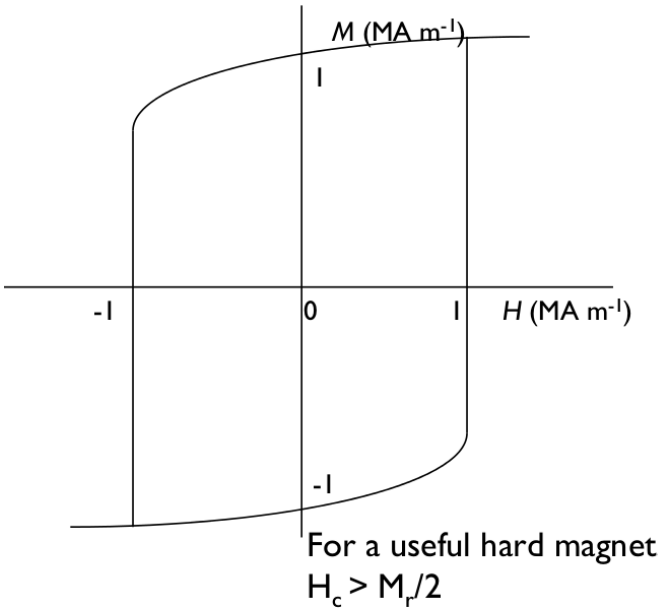

Figure 3.4: The area of the hysteresis loop represents the energy loss per cycle. For hard magnetic materials, this needs to be as big as possible. The Magnetization $\mathbf{M}$ and the magnetic field $\mathbf{H}$ have the same units $[\frac{A}{m}]$. This picture is taken from [80].

3.2.3 Soft magnetic materials

Soft magnetic materials have a very narrow hysteresis loop and like mentioned above they get magnetized with low magnetic fields.

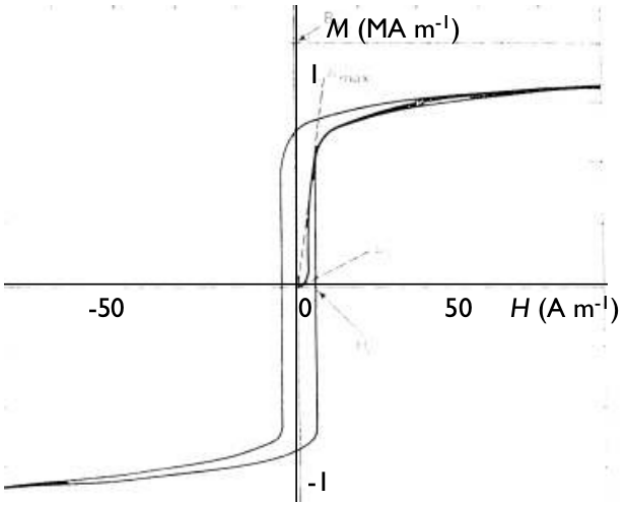

Figure 3.5: The area of the hysteresis loop represents the energy loss per cycle. For soft magnetic materials, this needs to be as small as possible. The Magnetization $\mathbf{M}$ and the magnetic field $\mathbf{H}$ have the same units $[\frac{A}{m}]$. This picture is taken from [80].

Soft materials are used for static and AC applications. Static and low-frequency applications are such as electromagnets and relays. Major AC applications include cores for transformers, electric motors and generators and many more.

3.2.4 Magnetic applications

Magnets play a major role in our civilization, most of us use many tools without knowing that that magnetic materials are integrated in that tool, e.g. in every car are at least two or three different magnetic materials integrated. Soft magnets are used among many other things to generate electricity, and convert electrical energy into mechanical energy. Hard magnets are used among many other things to generate magnetic fields.

Permanent magnets

Permanent magnets are ferromagnets with a wide hysteresis loop. Some examples of permanent magnet applications are:

- magnetic resonance imaging,
- magnetic powder alignment,
- sensors,
- motors,
- generators,

- beam control,
- holding magnets,
- and several more, see [74, 79, 40].

Of course there are several other uses of magnets, which can not be all listed here. Some additional applications of permanent magnetic materials can be found in [74, 80, 79, 78].

Applications of soft magnets

Soft materials are mainly used for static and AC applications. Some examples of soft magnetic applications are:

- electromagnets,
- relays,
- inductors,
- antenna rods,
- and several more, see [74, 79, 40] .

Magnetic recording

Digital and analog recording vie magnetic materials has already been used several decades ago. Magnetic recording has the advantage of being indefinitely rewritable. Nowadays magnetic recording is a huge industry, with large quantities of different magnetic materials in need. Additionally very sophisticated miniature magnetic circuits are used and developed in the read and write heads.

Figure 3.6: Nowadays it is easy to get a 1 Tb hard disk, left picture. But just a few decades ago a computer as big as a room could only store 40 Mb, right picture. Pictures taken from [80].

In Figure 3.6 a modern digital magnetic magnetic hard disk and a few decades old computer is shown. The sizes of the hard disks shrunk a lot thankfully. Nowadays almost all magnetic records are digital, magnetic tapes and alike are not present anymore.

Chapter 4

DFT in action

4.1 Equation of state

A very simple equation of state is

$$E(a) = E(a_0) + \beta(a - a_0)^2, \tag{4.1}$$

with E_0, β and a_0 as the fitting parameters. Equation (4.1) is a very simple dependence between the total ground state energy and the lattice constant and is only valid for a small range of lattice constants around the equilibrium. For greater variations of the lattice parameter one needs a better model because the relationship between the energy and lattice constant is not just a quadratic one. A better model is the so called Birch-Murnagham [87, 88] equation of state:

$$E(a) = E(a_0) + \frac{9}{16} B_0 a_0^3 \left(\left[\left(\frac{a_0}{a} \right)^2 - 1 \right]^3 B_0' + \left[\left(\frac{a_0}{a} \right)^2 - 1 \right]^2 \left[6 - 4 \left(\frac{a_0}{a} \right)^2 \right] \right), \tag{4.2}$$

In this equation (4.2), a_0 is the equilibrium lattice constant, B_0 is the bulk modulus at zero pressure and $B_0' = \left(\frac{\partial B}{\partial P}\right)_T$. To apply equation (4.2) to a set of data from density functional theory calculations one treats a_0, B_0, B_0' and E_0 as fitting paramaters.

4.2 DFT calculation of bcc sodium

As an example how the Birch-Murnagham equation works, the relaxation of bcc sodium is shown. The primitive cell for an bcc metal can be defined by the following cell vectors:

$$\vec{a}_1 = a(-\frac{1}{2}, \frac{1}{2}, \frac{1}{2}) \qquad \vec{a}_2 = a(\frac{1}{2}, -\frac{1}{2}, \frac{1}{2}) \qquad \vec{a}_3 = a(\frac{1}{2}, \frac{1}{2}, -\frac{1}{2}). \tag{4.3}$$

With one atom at $(0, 0, 0)$. The calculations were done with the PAW PBE GGA pseudopotential, with a cutoff energy of 265 eV, with $11 \times 11 \times 11$ k-points and a Monkhorst pack grid.

The total energy over the lattice parameters were fitted with Birch-Murnagham equation (4.2). Results of this fit are shown in Figure 4.1.

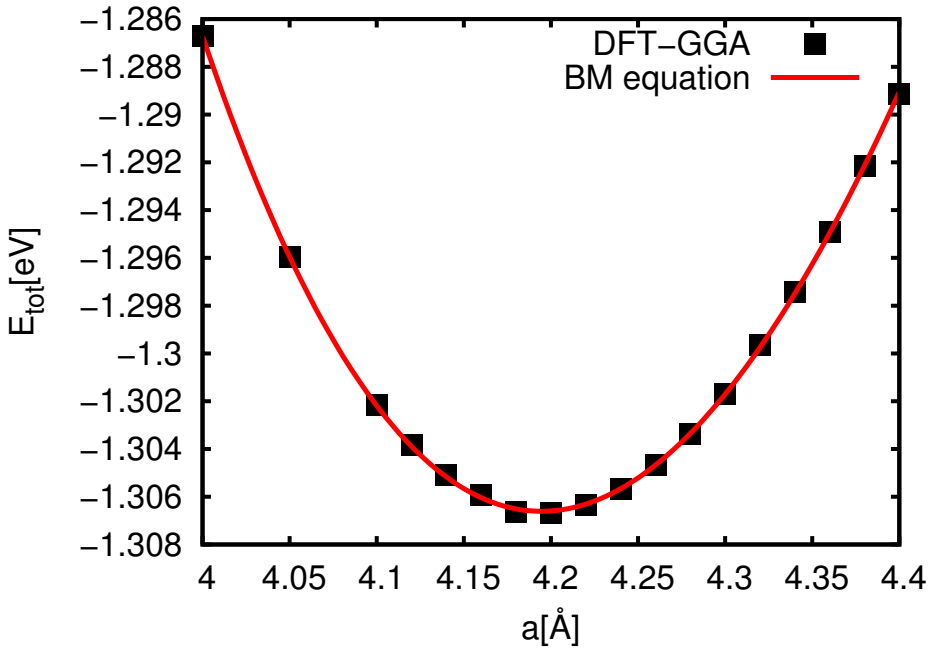

Figure 4.1: Total energy, E, of Na in the bcc crystal structure as a function of the lattice parameter a. The data points are from a DFT calculation done with PAW GGA PBE pseudopotential and the solid line is a least square fit with Birch-Murnagham eqation 4.2.

Predicted parameters from this fit are: $a_0 = 4.19$ Å and $B = 7.068$ GPa. Experimental values for Na are $a_0 = 4.2906$ Å and $B = 6.3$ GPa [89], the calculated values are in good agreement with the experimental values.

4.2.1 Calculation details

In the following listing of a shell script, all the information to run this calculation is listed. It generates the required INCAR and KPOINTS files and then a loop for different POSCAR files is run to vary the lattice constant then the OUTCAR files are stored. The information needed is the total energy for each run and the corresponding volume, these are read and printed to a separate file, which can be used to fit to the Birch-Murnagham [87, 88] equation of state.

```
#!/bin/bash

cat >INCAR <<!
System          = bcc Na
ISTART          = 0
ICHARG          = 2
ENCUT           = 265
LMAXMIX         = 4
ISMEAR          = -5
```

```
GGA_COMPAT     = .FALSE.
!

cat >KPOINTS <<!
K-Points
0
Monkhorst Pack
11 11 11
0 0 0
!


for i in 4.00 4.05 4.12 4.14 4.16 4.18 4.45
do
cat >POSCAR <<!
bcc Na:
$i
-0.5   0.5   0.5
 0.5  -0.5   0.5
 0.5   0.5  -0.5
1
cartesian
0 0 0
!

rm WAVECAR
rm CHG CHGCAR
./../vasp

cat POSCAR INCAR CONTCAR OUTCAR >> bccNa.rel.OUTCAR.$i

e1=`grep TOTEN bccNa.rel.OUTCAR.$i | tail -1 | cut -c30-44`
v1=`echo "$i * $i * $i" | bc -l`

a1=($i $v1 $e1)
echo ${a1[*]} >> energy_bccNa.rel.ev.dat

done
```

4.3 DFT calculation of fcc copper

Here we show some insight into the capabilities of DFT calculations nowadays using the Vienna ab initio simulation package (VASP). Cu is a great example of a simple metal with an electronic structure very similar to a free electron gas.

4.3.1 Density of states and band structure of copper

The primitive vectors for the fcc structure are:

$$\vec{a}_1 = a(\frac{1}{2}, \frac{1}{2}, 0) \qquad \vec{a}_2 = a(0, \frac{1}{2}, \frac{1}{2}) \qquad \vec{a}_3 = a(\frac{1}{2}, 0, \frac{1}{2}) \quad . \tag{4.4}$$

The lattice vector of Cu is $a = 3.61$ Å [40].

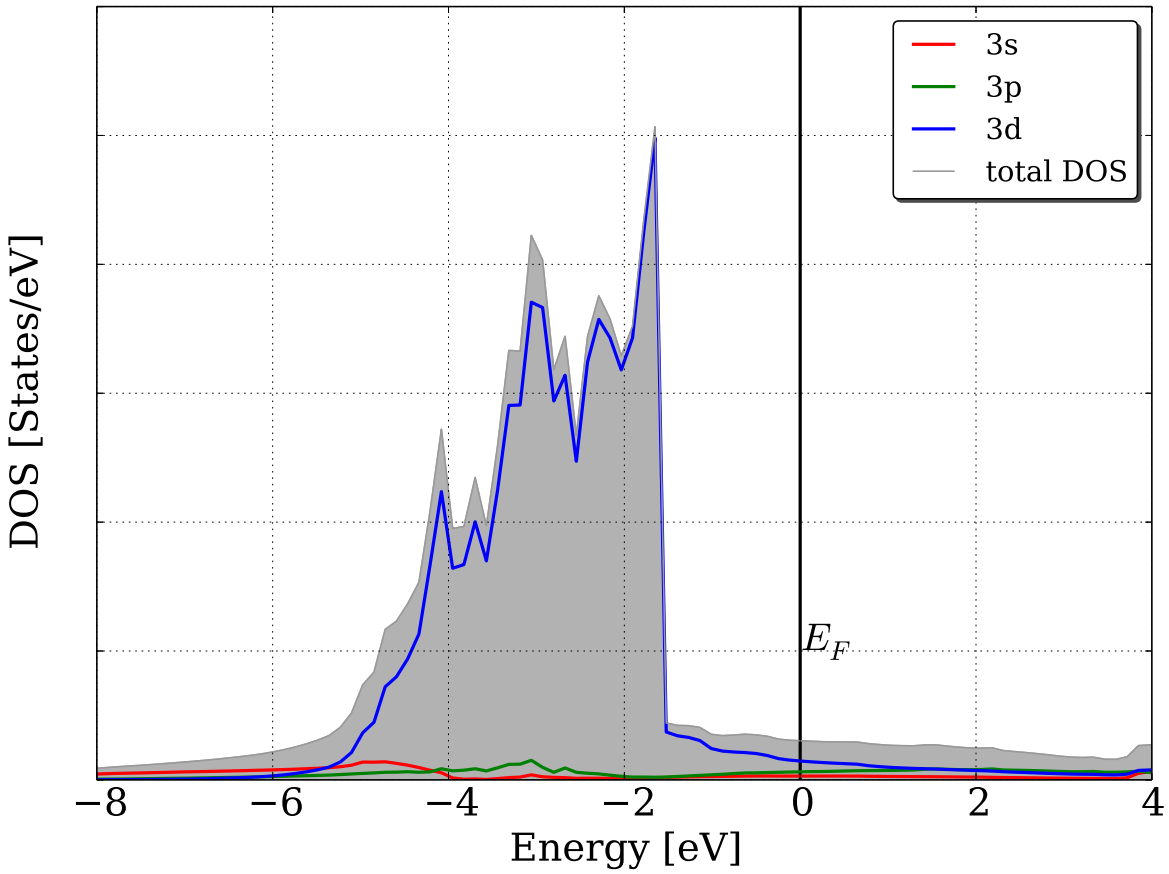

Figure 4.2: Density of states of fcc Cu calculated with VASP. A wide energy range is shown.

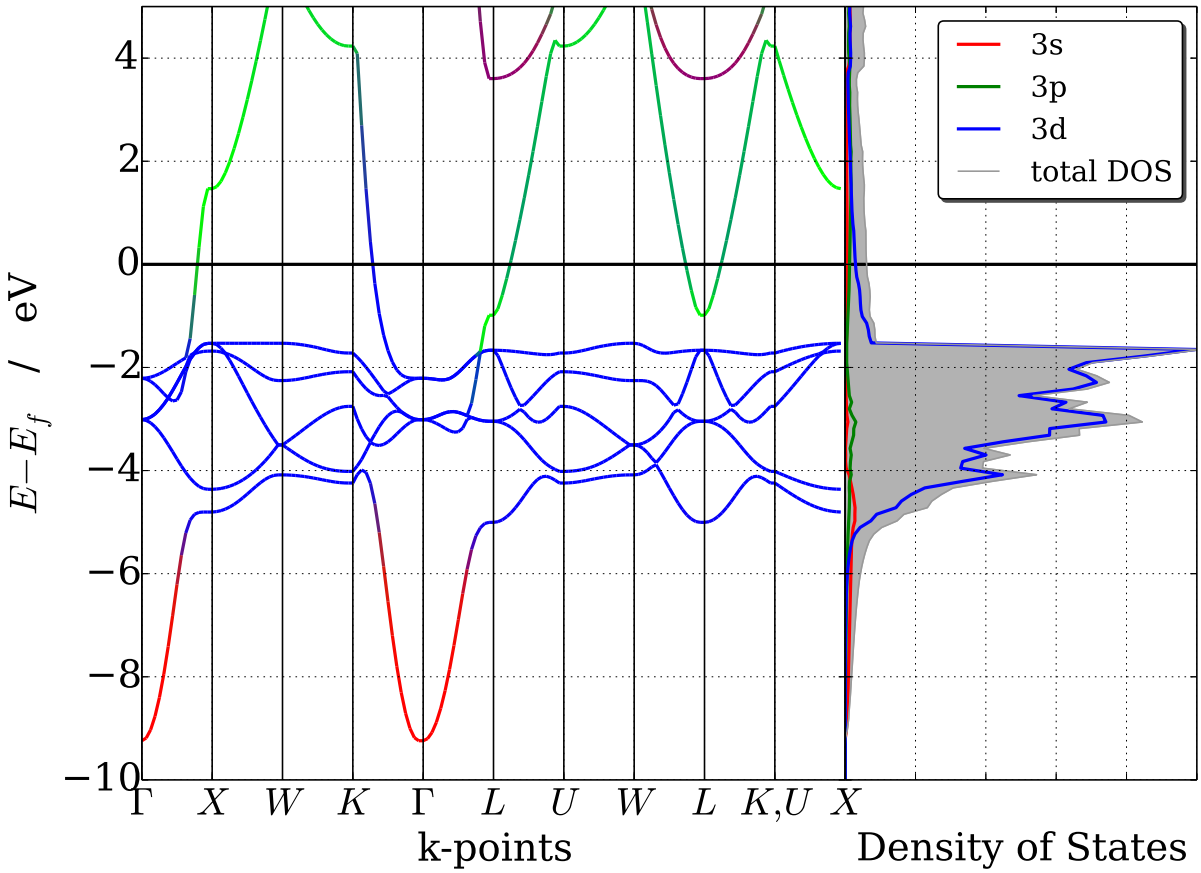

Figure 4.3: Left plot: band structure of fcc Cu calculated with VASP, right plot: corresponding density of states.

In Figure 4.2 the density of states of Cu calculated with VASP is shown and in Figure 4.3 the band structure is shown. The resemblance to the free electron gas can be clearly seen in the band structure, especially at the Γ-Point in the Brillouin zone.

4.3.2 Calculation details

In the following shell script all the information needed to run above calculation is presented.

```
#!/bin/bash

cat >POSCAR <<!
fcc Cu
3.61
  0.5   0.5   0.0
  0.0   0.5   0.5
  0.5   0.0   0.5
1
direct
```

```
0.000  0.000  0.000
!


cat >KPOINTS <<!
K-Points
0
Gamma
16  16  16
0  0  0
!

# first calculation
cat >INCAR <<!
ISTART      = 0
ICHARG      = 1
EDIFF       = 1.0E-06
LMAXMIX     = 4             # all L quantum numbers in charge are written out
ISMEAR      = -5            # mp smearing, metal
EDIFF       = 1E-6            # tight convergence
LORBIT      = 11
!

rm WAVECAR
rm CHG CHGCAR
~/bin/vasp

cp OUTCAR OUTCAR.dos
cp EIGENVAL EIGENVAL.dos
cp DOSCAR DOSCAR.dos

#for bandstructure new kpoints file
cat >KPOINTS <<!
FCC (face-centered cubic) G-X-W-K-G-L-U-W-L-K U-X
16    ! 16 grids
Line-mode
reciprocal
    0.000    0.000    0.000    ! \Gamma
    0.500    0.000    0.500    ! X

    0.500    0.000    0.500    ! X
    0.500    0.250    0.750    ! W

    0.500    0.250    0.750    ! W
    0.375    0.375    0.750    ! K

    0.375    0.375    0.750    ! K
    0.000    0.000    0.000    ! \Gamma

    0.000    0.000    0.000    ! \Gamma
    0.500    0.500    0.500    ! L

    0.500    0.500    0.500    ! L
    0.625    0.250    0.625    ! U

    0.625    0.250    0.625    ! U
    0.500    0.250    0.750    ! W

    0.500    0.250    0.750    ! W
    0.500    0.500    0.500    ! L

    0.500    0.500    0.500    ! L
    0.375    0.375    0.750    ! K

    0.625    0.250    0.625    ! U
```

```
    0.500    0.000    0.500    ! X
!

cat >INCAR <<!
System          = fcc Cu
ICHARG          = 11
EDIFF           = 1.0E-06
ISPIN           = 1
LMAXMIX         = 4          # all L quantum numbers in charge are written out
ISMEAR          = 0
SIGMA           = 0.05
LORBIT          = 11
!

~/bin/vasp

cp OUTCAR OUTCAR.band
cp CHGCAR CHGCAR.band
cp EIGENVAL EIGENVAL.band
```

4.3.3 Fermi surface of Cu

It is also possible to calculate Fermi surfaces with VASP. One needs to run a self consistent run with a lot of k-points and than a non self consistent run with the symmetry turned off in the INCAR-file. I have used Xcrysden [90, 91] to plot the Fermi surface. To be able to do that the eigenvalues have to be in certain order for Xcrysden. For this purpose I have written a shell AWK script, which is presented in the appendix.

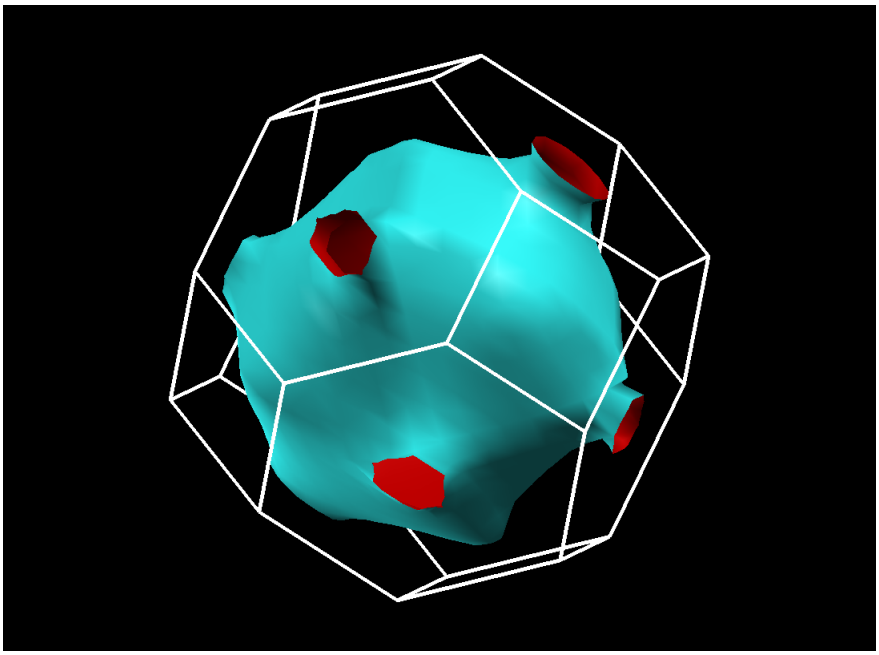

Figure 4.4: Fermi surface of fcc Cu calculated with VASP and plotted with Xcrysden.

In Figure 4.4 the Fermi surface of Cu is shown and one can see a sphere shape with some hole anomalies. This is because of the resemblance to the free electron gas.

4.3.4 Calculation details

The following shell script needs to be run and theirafter the shell AWK script presented in chapter E.4.

```
#!/bin/bash

cat >POSCAR <<!
Cu
3.61
   0.0  0.5  0.5
   0.5  0.0  0.5
   0.5  0.5  0.0
Cu
1
Direct
   0.0  0.0  0.0  Cu
!

cat >KPOINTS <<!
K-Points
0
Gamma
16 16 16
0 0 0
!

# first calculation
cat >INCAR <<!
ISTART      = 0
ICHARG      = 1
EDIFF       = 1.0E-06
LMAXMIX     = 4             # all L quantum numbers in charge are written out
ISMEAR      = -5            # mp smearing, metal
EDIFF       = 1E-6            # tight convergence
LORBIT      = 11
!

rm WAVECAR
rm CHG CHGCAR
~/bin/vasp


cat >INCAR <<!
ISTART      = 0
ICHARG      = 1
EDIFF       = 1.0E-06
LMAXMIX     = 4             # all L quantum numbers in charge are written out
ISMEAR      = -5            # mp smearing, metal
EDIFF       = 1E-6            # tight convergence
LORBIT      = 11
ISYM        = -1
!

~/bin/vasp
```

Chapter 5

The alloy system $Fe_{1-x}Co_x$

Fe-Co alloys are of special interest not only because of their magnetic properties but also because of their practical importance in structural and functional alloys. Special interest has been generated for Fe-Co alloys, because of contributions of magnetic and chemical ordering to the phase equilibria [92]. The phase diagram of the Fe-Co alloy system is shown in Figure 5.1, taken from [93].

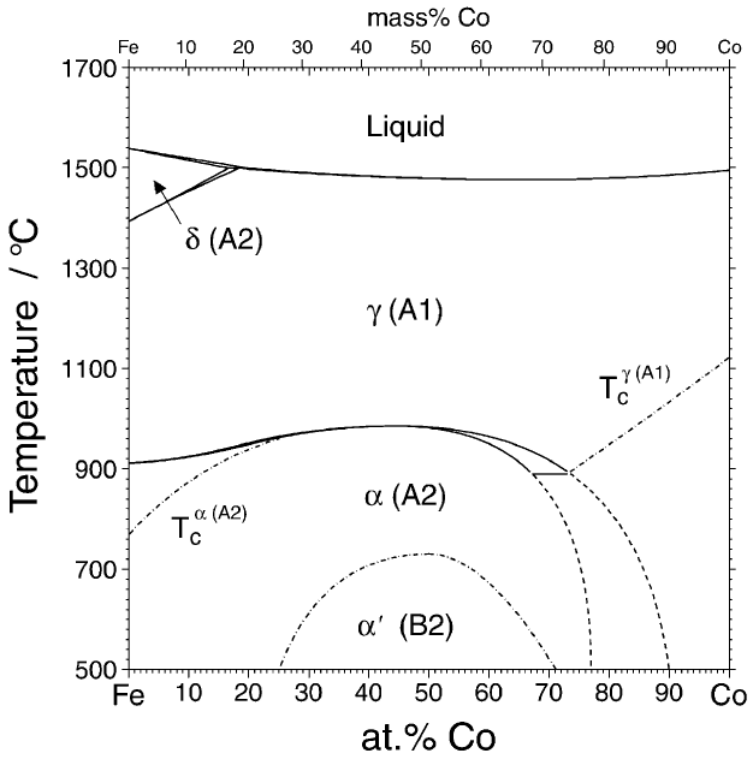

Figure 5.1: Phase diagram of the Fe-Co binary system, taken from [93]

Table 5.1: The different phases in the phase diagram of the Fe-Co alloy system, Figure 5.1.

phase	structure	order-disorder	modeling
γ A1	fcc(ccp) Fm$\bar{3}$m (225)	disorder	CPA or supercell
α A2	bcc Im$\bar{3}$m (229)	disorder	CPA or supercell
$\alpha^{'}$ B2	bcc (CsCl) Pm$\bar{3}$m (221)	order	CPA or VCA

In this work we are only concentrating on the α- and $\alpha^{'}$-phases, in table 5 we have listed the possible methods to model these phases. The ordered $\alpha^{'}$-phase will be modeled with the so called virtual crystal approximation (VCA), which will be explained in section 5.1.1. The disordered α-phase will be modeled with randomized supercells, which will be explained in section 5.3.

5.1 Lattice minimization with virtual crystal approximation

5.1.1 Virtual crystal approximation (VCA)

In the VCA, pseudopotentials of fictitious atoms of $Fe_{1-x}Co_x$ are created, these are special atoms with the atomic number $26 + x$ for each Co concentration. Since Fe and Co sit next to each other in the periodic table it is apparent that VCA should do a good job for the alloy $Fe_{1-x}Co_x$.
The complete system $Fe_{1-x}Co_x$ is calculated within the VCA approximation with the A2-structure, with primitive vectors:

$$\vec{a}_1 = \frac{a}{2}(-1,1,1), \quad \vec{a}_2 = \frac{a}{2}(1,-1,1), \quad \vec{a}_3 = \frac{a}{2}(1,1,-1),$$

and with the base vector:

$$\vec{b}_1 = (0,0,0).$$

The above structural data are actually the data from a A2-structure, but since in VCA we treat the alloy $Fe_{1-x}Co_x$ with one type of virtual atom, we actually model the ordered B2-structure (CsCl-structure) with the A2-structure.

5.1.2 Lattice minimization by using the Birch-Murnagham equation

The lattice minimization is done with the Birch-Murnagham [87, 88] equation of state:

$$E(a) = E(a_0) + \frac{9}{16}B_0 a_0^3 \left(\left[\left(\frac{a_0}{a}\right)^2 - 1 \right]^3 B_0^{'} + \left[\left(\frac{a_0}{a}\right)^2 - 1 \right]^2 \left[6 - 4\left(\frac{a_0}{a}\right)^2 \right] \right). \quad (5.1)$$

In this equation (5.1), a_0 is the equilibrium lattice constant, B_0 is the bulk modulus at zero pressure and $B_0' = \left(\frac{\partial B}{\partial P}\right)_T$. To apply equation (5.1) to a set of data from density functional theory calculations one treats a_0, B_0, B_0' and E_0 as fitting parameters.
On the following page some minimization for a few alloy compositions are shown:

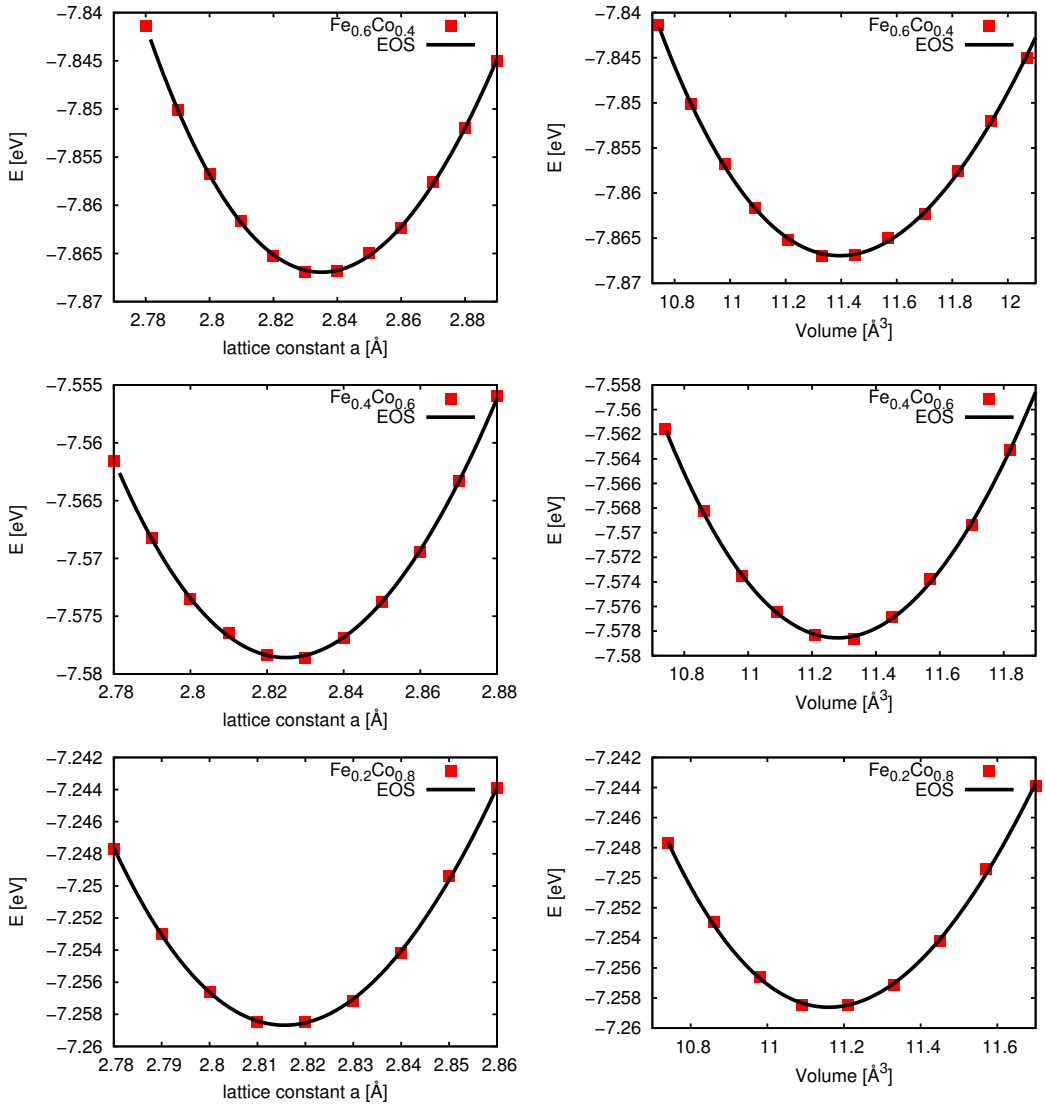

Figure 5.2: Volume and or lattice constant minimization with the Birch-Murnagham [87, 88] equation of state, denoted EOS in the plots.

One can see in the Figures in 5.2 the very good agreement between the Birch-Murnagham [87, 88] equation of state and our calculations. Energy over volume and over the lattice parameter are shown.
When putting all together, one can plot the volume, the lattice parameter, the magnetic moment

and the bulk modulus over the Co concentration.

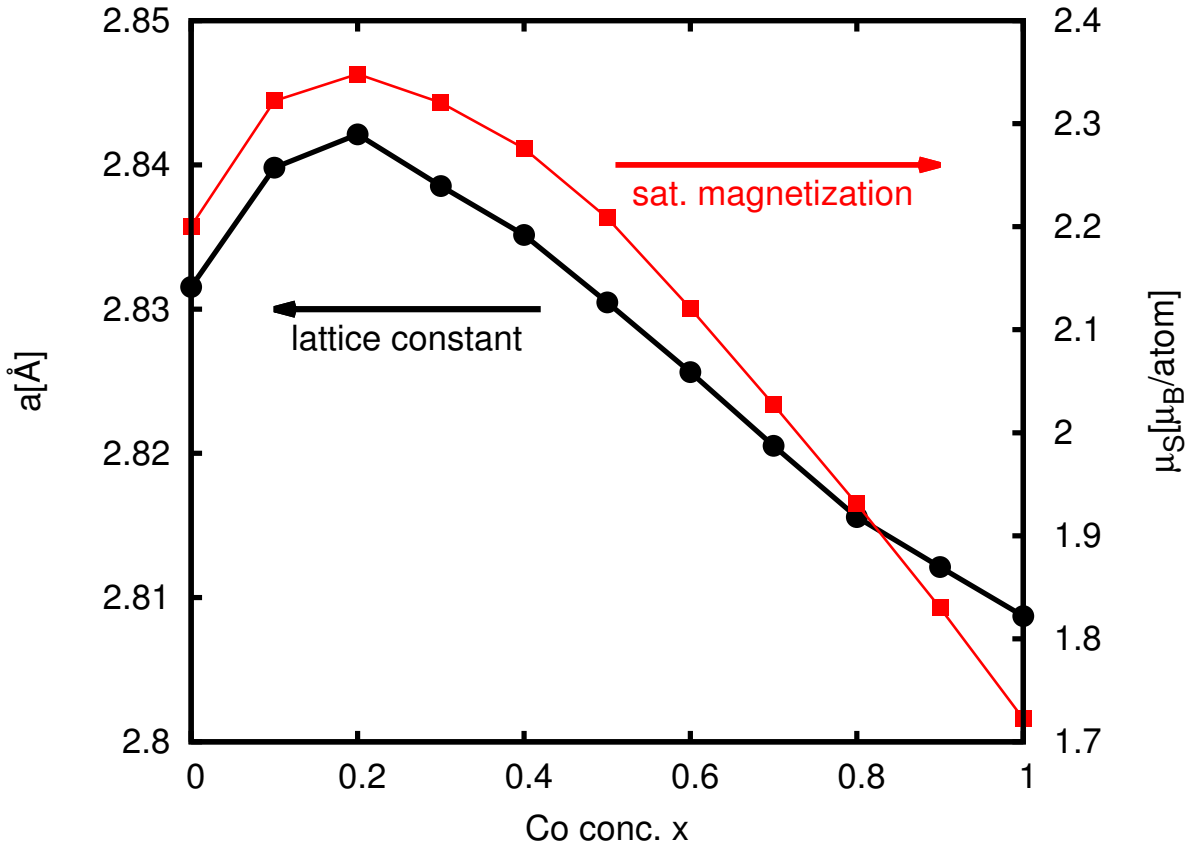

Figure 5.3: The minimized lattice constant and the equilibrium magnetic moments for the VCA calculations over the complete concentration range in the alloy $Fe_{1-x}Co_x$. The same trend for the lattice constants is experimentally observed in [92] and for the magnetic moment in [94].

In Figure 5.3 on the left y-axis the equilibrium lattice constants are shown. First the lattice constant increases until $Fe_{0.8}Co_{0.2}$ and then the continuously decreases, which is also found experimentally in [92]. Other groups had the same trend in their calculations [95]. In Figure 5.3 on the right y-axis the magnetic moments are presented a similar trend can be seen here, which is also experimentally asserted [94].
We have only modeled 10-alloys $Fe_{1-x}Co_x$, for $x = 0.0, 0.1, 0.2 \ldots, 1.0$. The actual composition, where the magnetic moment and the lattice constant have their maximum is for $x = 0.28$ [96], which we miss. To see this maximum one needs a much finer mesh for the alloy composition.

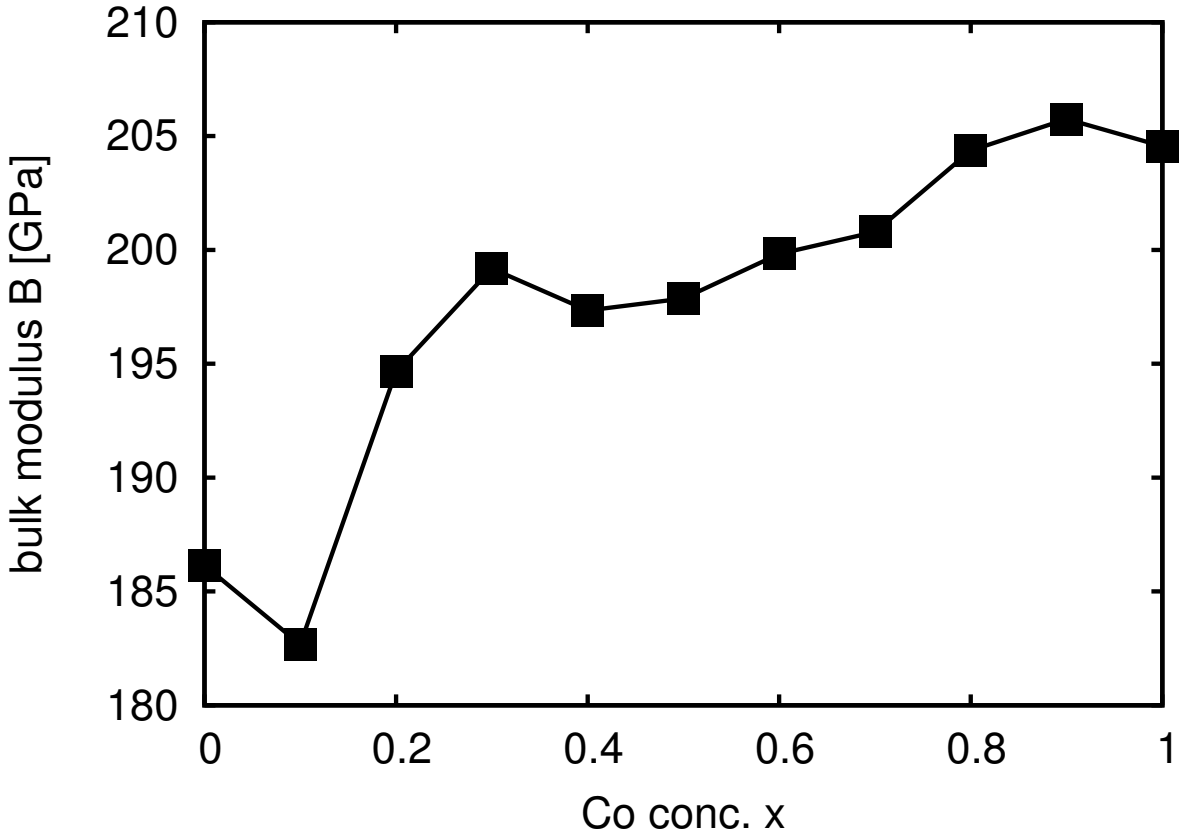

Figure 5.4: The equilibrium bulk moduli for the VCA calculations over the complete concentration range in the alloy $Fe_{1-x}Co_x$.

In Figure 5.4 the bulk moduli of the VCA minimization are shown, here we have a slightly decrease first up to $Fe_{0.9}Co_{0.1}$ and than an increase up to $Fe_{0.7}Co_{0.3}$, after that decreasing slightly again and then increasing. The bulk modulus of pure Fe is experimentally 173 [GPa] [97], which is lower than our results but still in the margin of error. For the alloys with Co concentrations there is not much experimental data available, that is because of the phase diagram of $Fe_{1-x}Co_x$. With VCA we model the ordered α'-phase which is encountered only for the Co concentration from $x = 0.25$ to $x = 0.7$ [92], the α-phase is a disordered phase, which is more likely a random alloy.

5.1.3 Electronic structure within the VCA approximation for the alloy $Fe_{1-x}Co_x$

In Figure 5.5 the spin density function for the majority spin up electrons is plotted. For $x = 0.0$ and $x = 1.0$ we have pure Fe and Co. For pure Fe we see weak ferromagnetism, the spin density of the majority electrons crosses the Fermi energy, this is because of the not completely filled

d-bands. With increasing x this crossing is moving below the Fermi energy and the spin density becomes strongly ferromagnetic, since pure Co is a strong ferromagnet. We see in Figure 5.5 that all five curves, for $x = 0.0, 0.2, 0.5, 0.7, 1.0$ respectively, have a pronounced peak. This central peak in the spin density is a peculiar feature of bcc structure intermetallic materials [75].

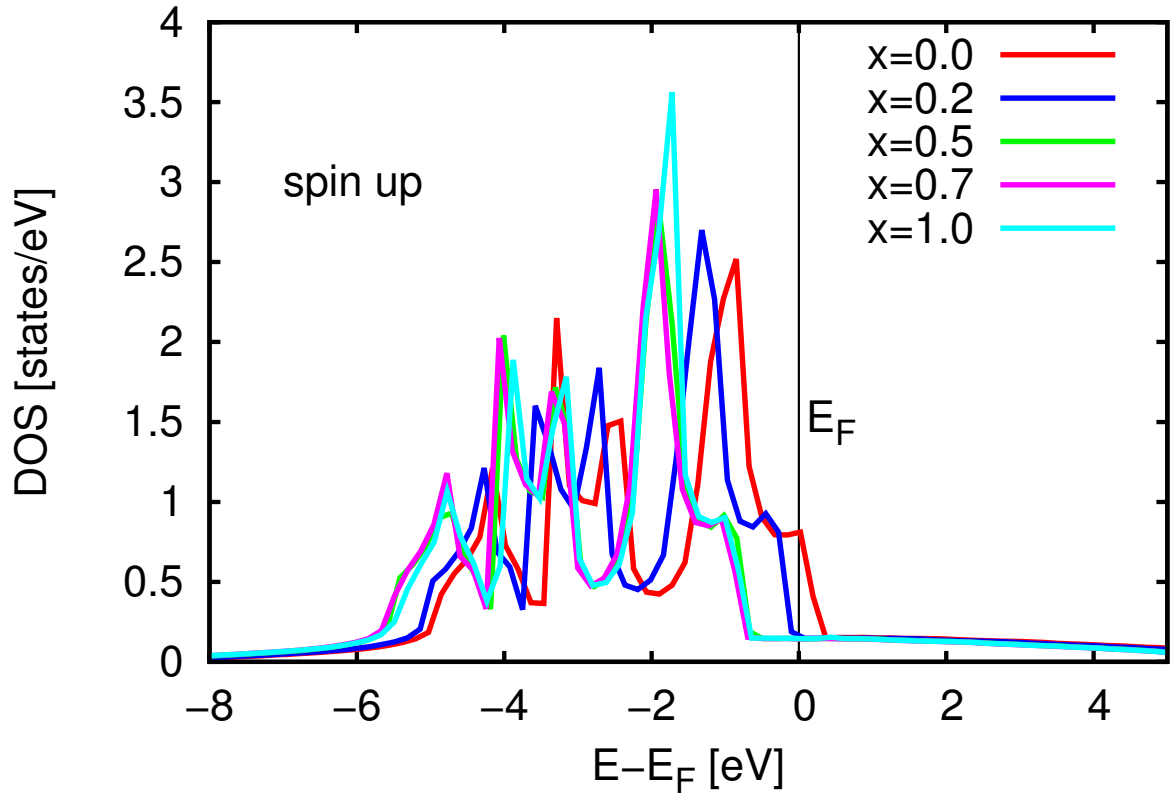

Figure 5.5: Spin up density of states of $Fe_{1-x}Co_x$ for the concentrations $x = 0.0, 0.2, 0.5, 0.7, 1.0$.

In Figure 5.6, we have plotted the spin density function for the minority spin down electrons. For pure Fe the Fermi energy crosses the spin down density in a minimum and for $x = 0.1$ also. For the concentrations $x = 0.5$ and $x = 0.7$ the Fermi level of the spin down density moves to the left. For pure Co the Fermi level of spin down density is almost in a maximum. These results are in agreement with earlier calculations done by Schwarz et al. [98] with the augmented plane wave (APW) approximation.

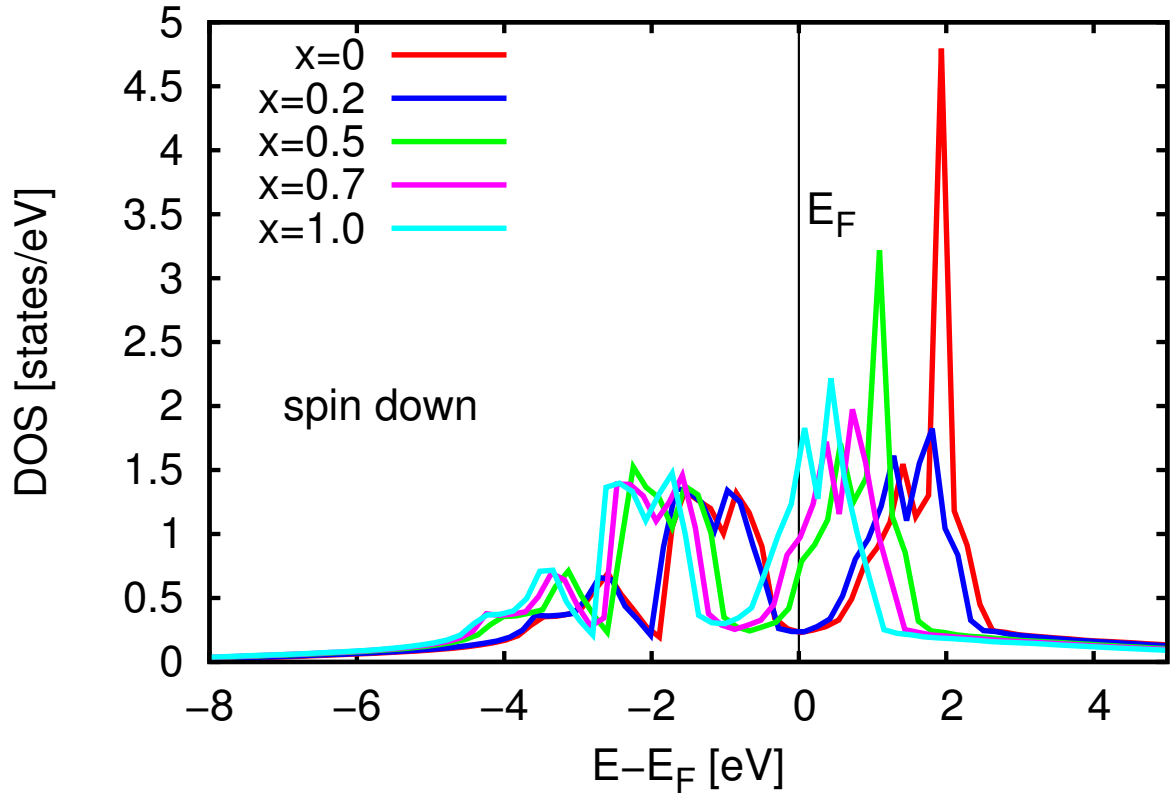

Figure 5.6: Spin down density of states of $Fe_{1-x}Co_x$ for the concentrations $x = 0.0, 0.2, 0.5, 0.7, 1.0$.

Since the Fe spin up band is filled and the spin down band is only partially filled, it is known from the theory of the chemical bond [96, 75], that the spin up electrons do not contribute to the bonding. Assuming Fe and Co having 5 electrons in the spin up band means that Fe has 3 and Co has 4 in the spin down band. From this fact follows that the spin up electrons do not contribute to the bulk modulus, so the bulk modulus decreases when starting to alloy, which can be seen in Figure 5.4. Accompanying with that fact is an increase in volume, an effect which is known as volume magnetostriction, which can be seen in Figure 5.3. Parallel with the magnetostriction also an increase in the magnetic moment is observed. Magnetostriction and the increase in the magnetic moment is not completely in accord with the observation in the bulk modulus, because the increase in the bulk modulus starts to early. We are assuming that all these three effects magnetostriction, magnetic moment increase and the bulk modulus decrease are turned around between $x = 0.2$ and $x = 0.3$. This can be seen in the Figure 5.7, where the spin down density crosses the Fermi energy after the minimum.

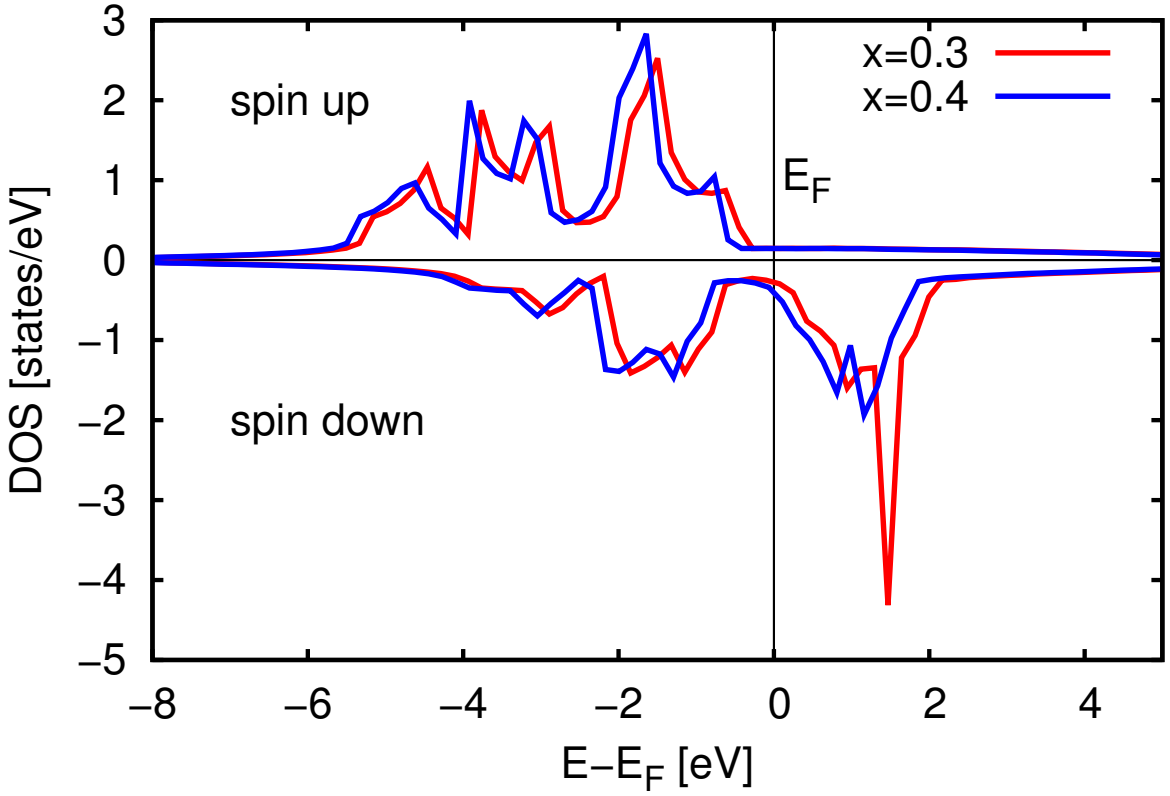

Figure 5.7: Spin up and down density of states of $Fe_{1-x}Co_x$ for the concentrations $x = 0.3, 0.4$ respectively.

We can say that already 10 % alloying of Co pushes the Fermi energy above the spin up band, but the spin down band stays pinned in a minimum for 10 % and 20 % Co. The transition to strong ferromagnetism starts to occur between 20 % and 30 % Co, the ferromagnetism gets stronger for more Co alloying.

5.1.4 Fermi surfaces of the alloy $Fe_{1-x}Co_x$ within the VCA approximation

In this section Fermi surfaces for pure Fe, for $Fe_{0.8}Co_{0.2}$, for $Fe_{0.5}Co_{0.5}$, for $Fe_{0.3}Co_{0.7}$ and for pure Co are shown. The Fermi surfaces for the other alloys will be presented in the appendix. Because of the different fillings of the spin up and spin down bands, the Fermi surfaces of course will be different for the spin up and spin down bands.

Fermi surfaces of Fe within the VCA approximation

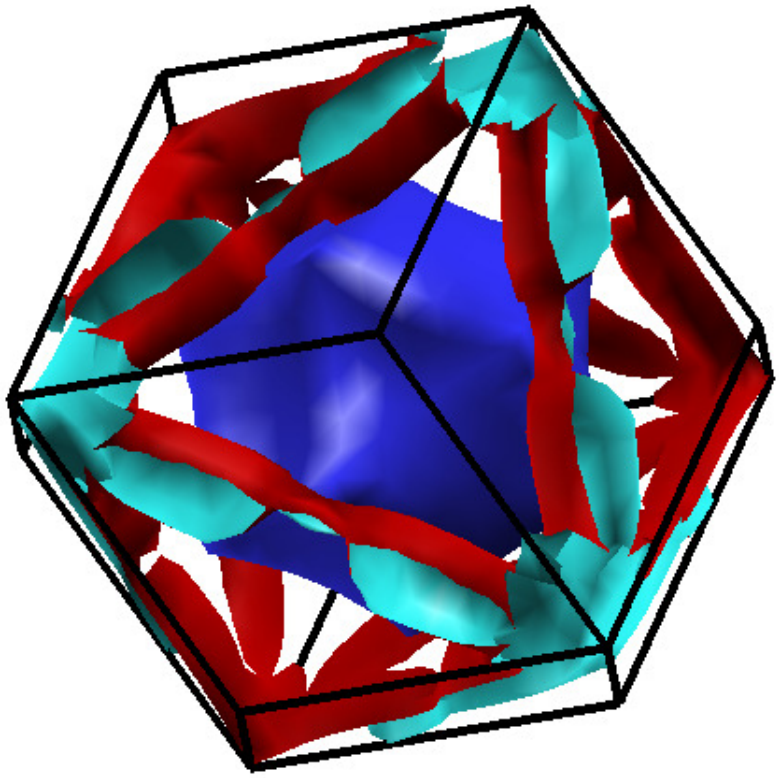

Figure 5.8: Fermi surface of Fe, spin up density. In the plot all the bands that cross the Fermi energy are merged in one plot.

For pure Fe we can see in Figure 5.8 the Fermi surface for the majority electrons and in Figure 5.9 we see the spin down Fermi surface. One can see immediately that the Fermi surface for the spin up electrons is much larger, because the density of the spin up electrons at the Fermi energy is much higher. And since the density of states at the Fermi level for the spin down electrons lies in a minimum, the Fermi surface is much smaller. The spherical part of the Fermi surface for the majority electrons in Figure 5.8 is the 4s character of the spin up bands, which is overshadowed by the 3d part of the spin up density.

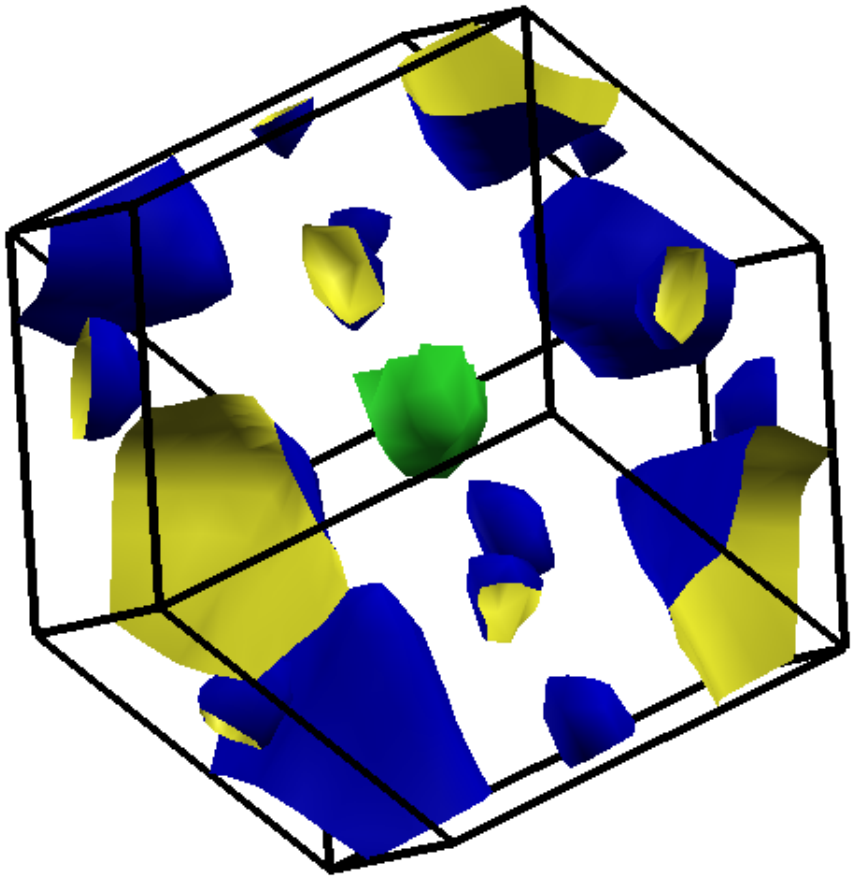

Figure 5.9: Fermi surface of Fe, spin down density. In the plot all the bands that cross the Fermi energy are merged in one plot.

Fermi surfaces of the alloy $Fe_{0.8}Co_{0.2}$ within the VCA approximation

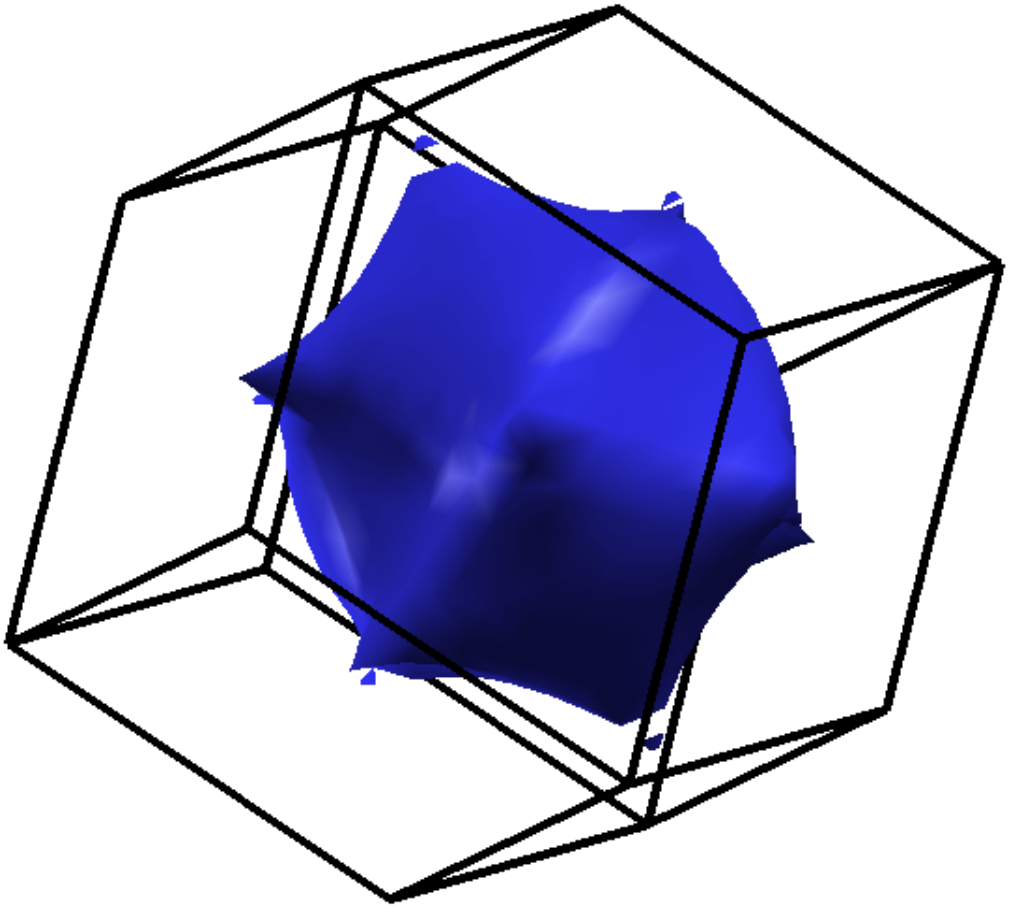

Figure 5.10: Fermi surface of $Fe_{0.8}Co_{0.2}$, spin up density. In the plot all the bands that cross the Fermi energy are merged in one plot.

In Figure 5.10 we see the the Fermi surface of $Fe_{0.8}Co_{0.2}$ for the majority electrons and in Figure 5.11 we see the spin down Fermi surface. The 3d character of the Fermi surface is gone and only the 4s character is left. For the spin down electrons in Figure 5.11 the Fermi surface got bigger. We will see this trend in this alloy $Fe_{1-x}Co_x$ until pure Co. This Figure 5.10 confirms our previous suspicion, that the sudden increase in volume from pure Fe to $Fe_{1-x}Co_x$ around $x \approx 0.1$ is related to the fact that the majority 3d electrons are pushed below the Fermi surface upon adding small amounts of Co to Fe. This obviously leads to an occupation of the

antibonding 3d states in the majority spin electrons.

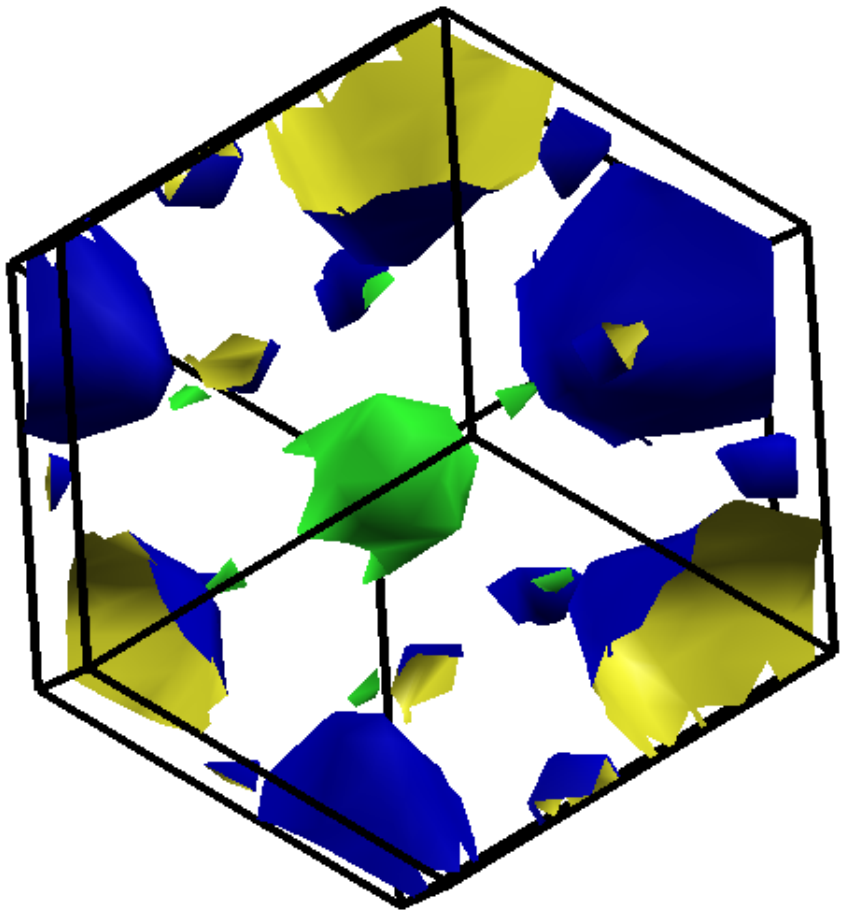

Figure 5.11: Fermi surface of $Fe_{0.8}Co_{0.2}$, spin down density. In the plot all the bands that cross the Fermi energy are merged in one plot.

Fermi surfaces of the alloy $Fe_{0.5}Co_{0.5}$ within the VCA approximation

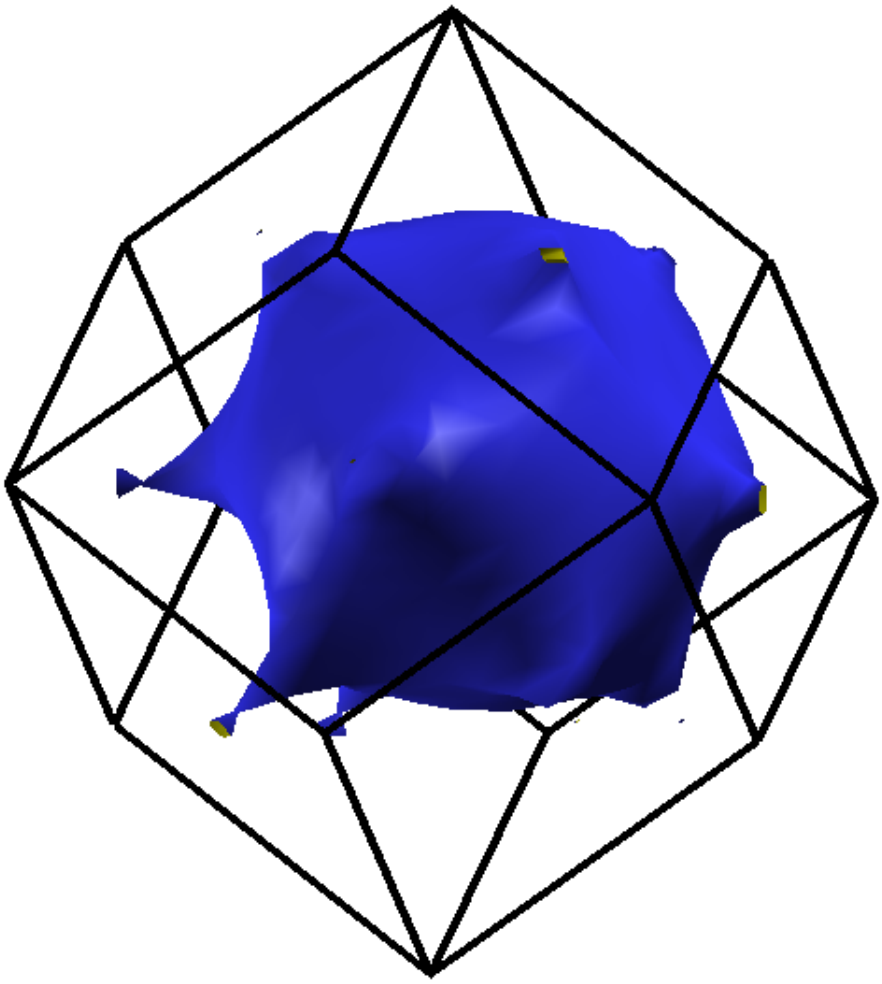

Figure 5.12: Fermi surface of $Fe_{0.5}Co_{0.5}$, spin up density. In the plot all the bands that cross the Fermi energy are merged in one plot.

In Figure 5.12 we see the the Fermi surface of $Fe_{0.5}Co_{0.5}$ for the majority electrons and in Figure 5.13 we see the spin down Fermi surface. The 3d character of the Fermi surface is still gone and only the 4s character is left. For the spin down electrons in Figure 5.13 the Fermi surface got much bigger and more complex, corresponding to a progressive occupation of e_g like states. We see practically no difference to the Figure 5.10, except a slightl increase in the size of the area.

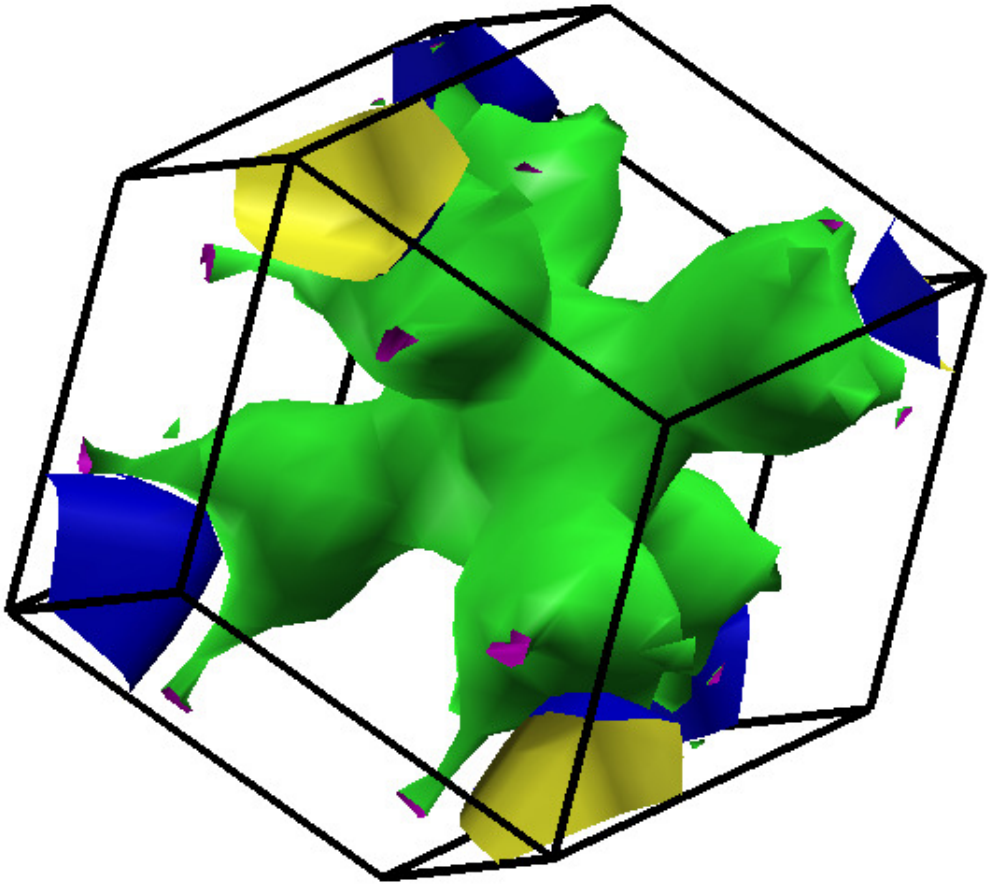

Figure 5.13: Fermi surface of $Fe_{0.5}Co_{0.5}$, spin down density. In the plot all the bands that cross the Fermi energy are merged in one plot.

Fermi surfaces of the alloy $Fe_{0.3}Co_{0.7}$ within the VCA approximation

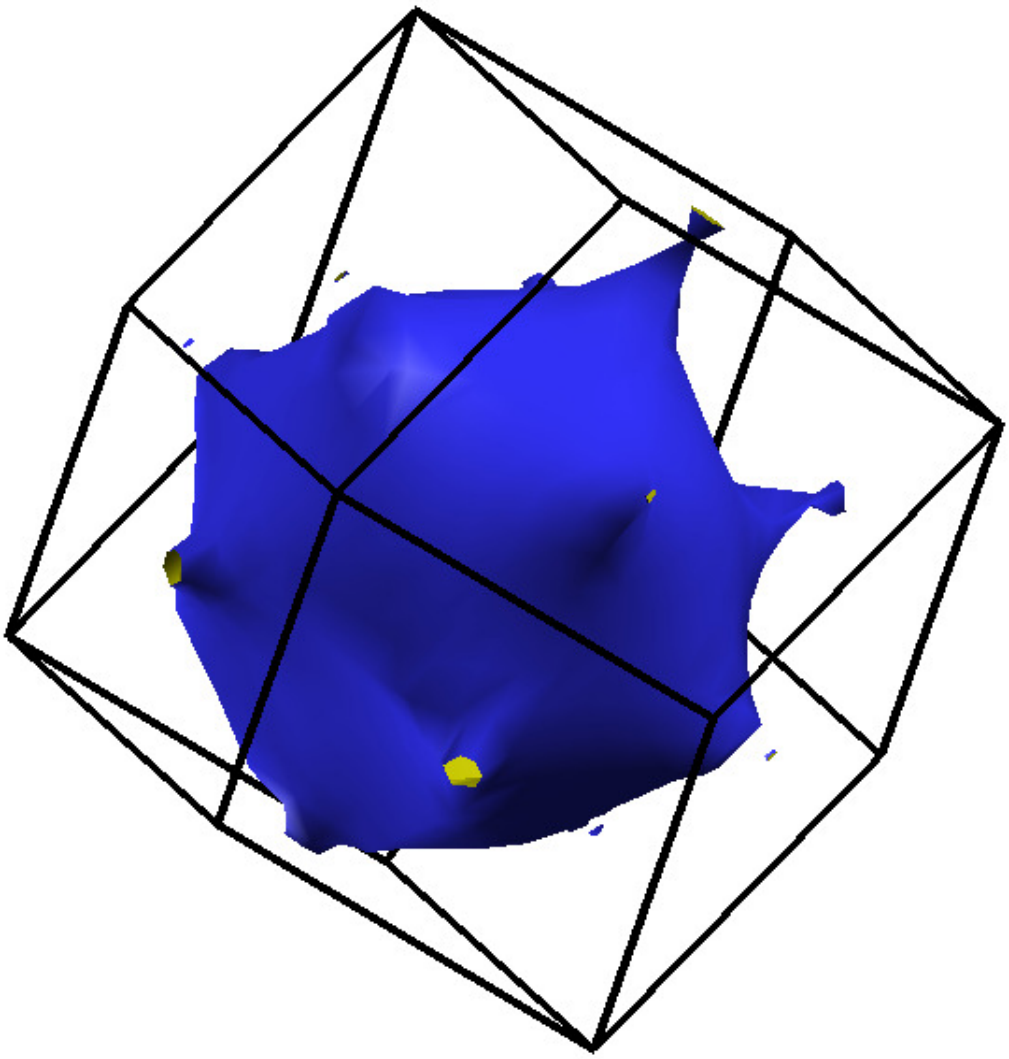

Figure 5.14: Fermi surface of $Fe_{0.3}Co_{0.7}$, spin up density. In the plot all the bands that cross the Fermi energy are merged in one plot.

In Figure 5.14 we see the the Fermi surface of $Fe_{0.3}Co_{0.7}$ for the majority electrons and in Figure 5.15 we see the spin down Fermi surface. For the spin down electrons in Figure 5.15 the Fermi surface got much bigger and more complex. For that reason the separate Fermi surfaces for the diverse bands are plotted in Figure 5.16, namely of the bands number 4, 5 and 6.

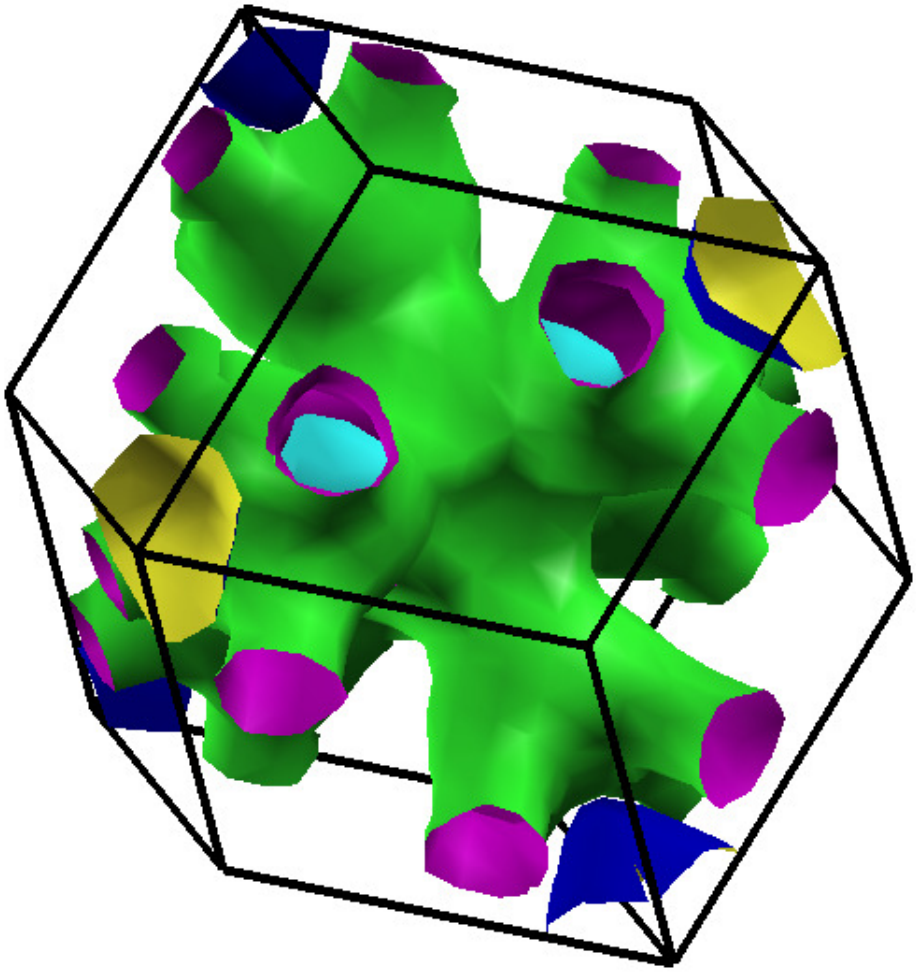

Figure 5.15: Fermi surface of $Fe_{0.3}Co_{0.7}$, spin down density. In the plot all the bands that cross the Fermi energy are merged in one plot.

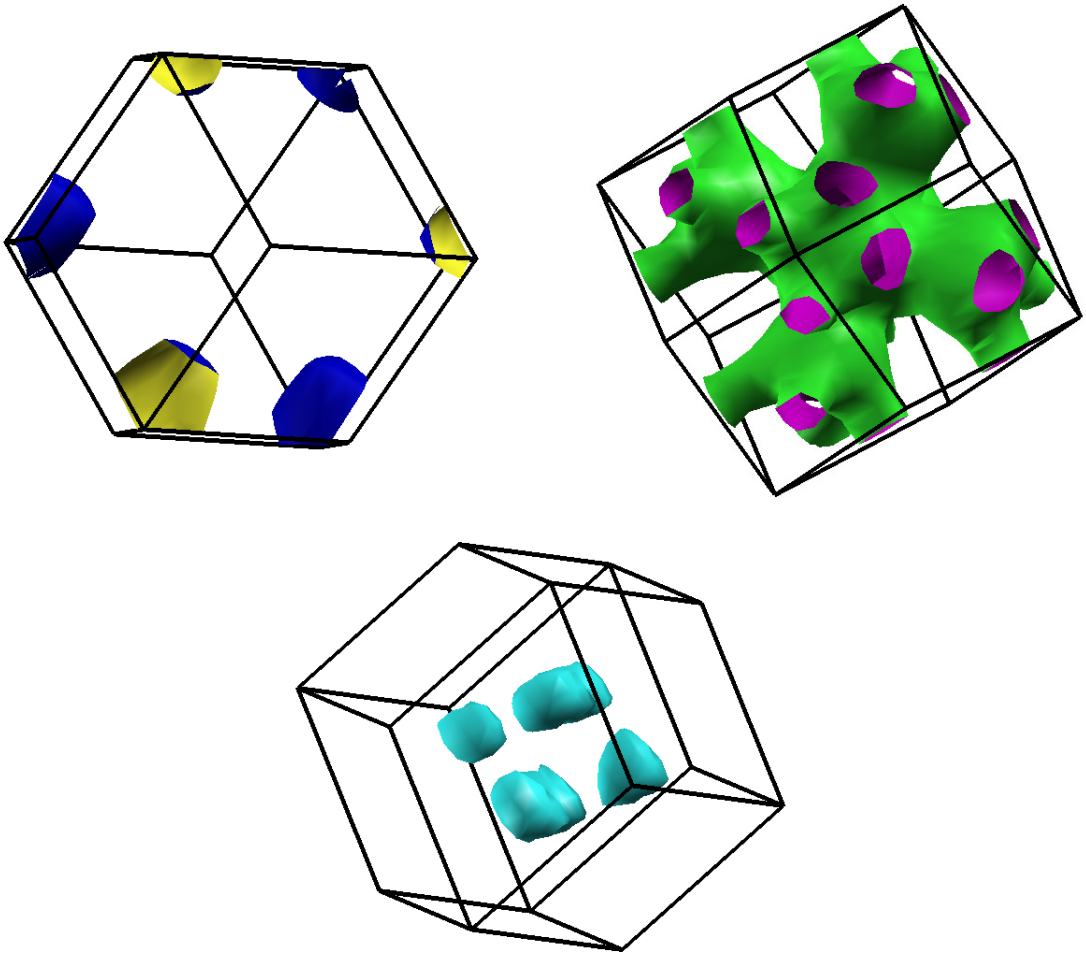

Figure 5.16: Fermi surface of $Fe_{0.3}Co_{0.7}$, spin down density. For the bands 4, 5 and 6.

Fermi surfaces of Co within the VCA approximation

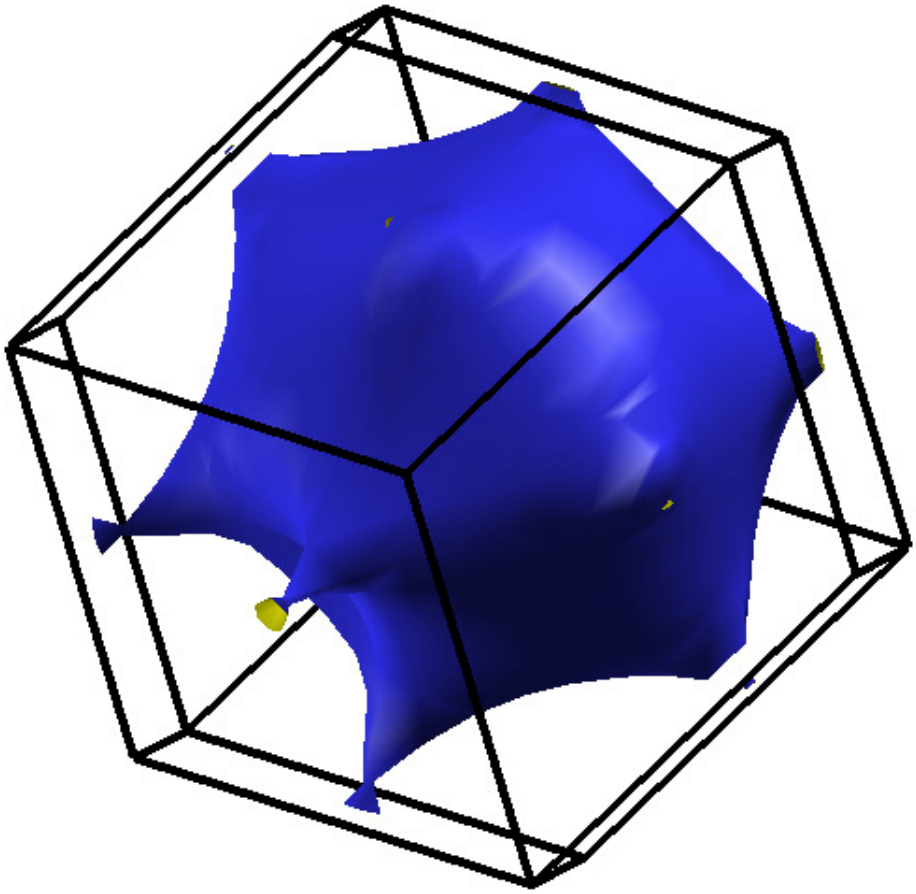

Figure 5.17: Fermi surface of Co, spin up density. In the plot all the bands that cross the Fermi energy are merged in one plot.

In Figure 5.17 we see the the Fermi surface of $Fe_{0.3}Co_{0.7}$ for the majority electrons and in Figure 5.18 we see the spin down Fermi surface. Also here we plot separate Fermi surfaces for the diverse bands which can be seen in Figure 5.19, these are Fermi surfaces of the bands with the numbers 4, 5 and 6. The volume has now extended towards the Brillouin zone boundaries, and electrons can thus move from one Brillouin zone to the next in an extended Brillouin zone scheme.

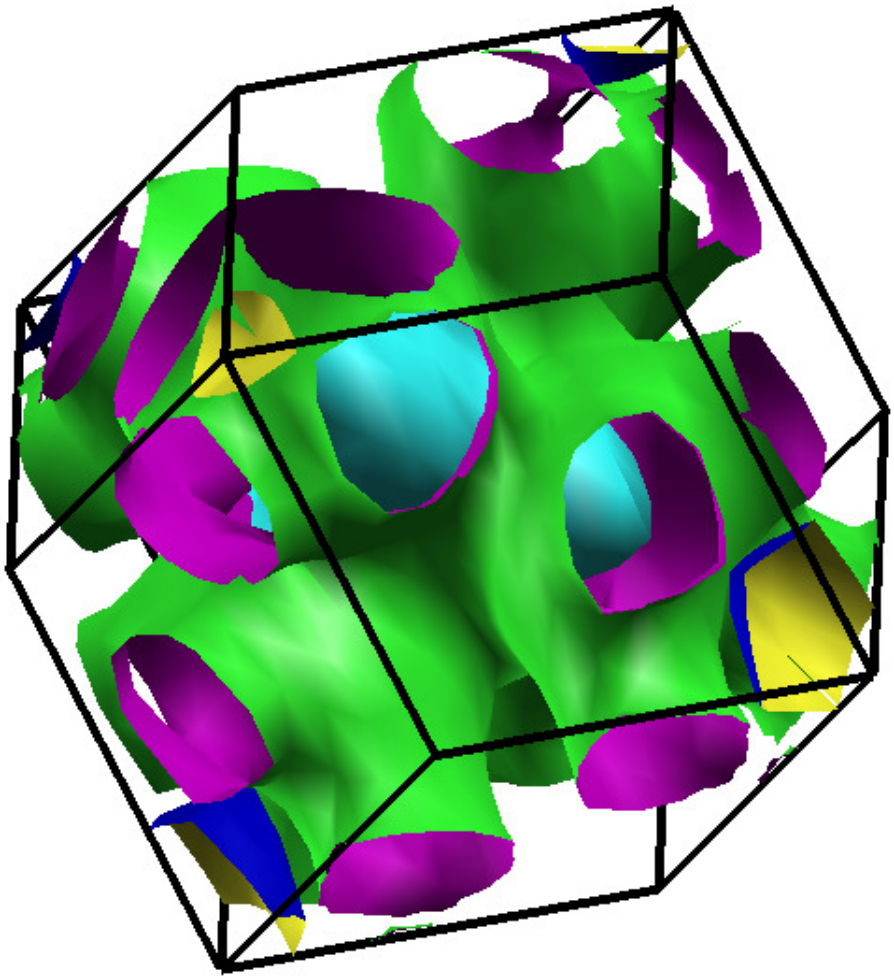

Figure 5.18: Fermi surface of Co, spin down density. In the plot all the bands that cross the Fermi energy are merged in one plot.

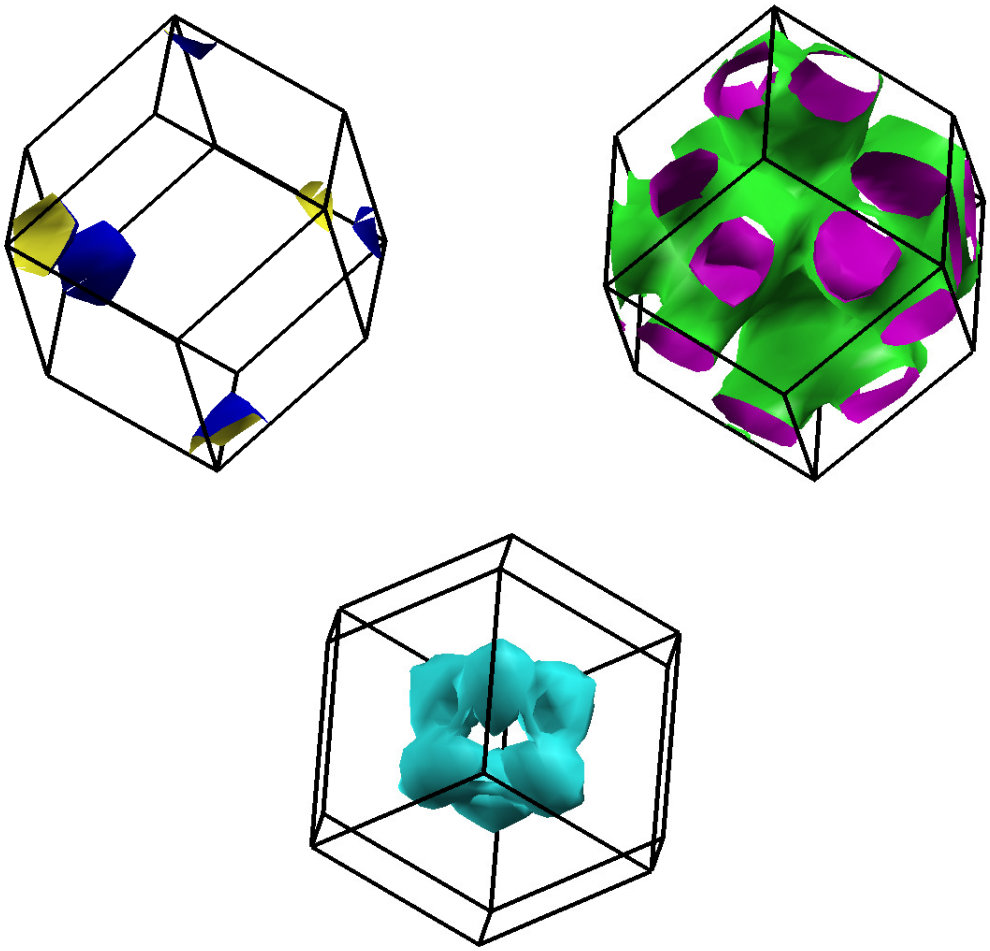

Figure 5.19: Fermi surface of Co, spin down density. For the bands 4, 5 and 6.

5.2 Advanced VCA of the alloy $Fe_{1-x}Co_x$

In the second type of VCA calculations done in this work the potential of the virtual system alloy is generated by compositionally averaging the potentials as described in [11]. Because of the small chemical differences between Fe and Co atoms, an actual configuration of $Fe_{1-x}Co_x$ can be achieved by weighting the pseudopotential of Fe with a factor of $(1-x)$ and the pseudopotential of Co by a factor of x. This type of VCA calculation will be contemplated as VCA2 in this work and the results of VCA2 will be presented together with the results of the VCA and supercell calculations.

5.3 Supercell simulation of the α-phase of $Fe_{1-x}Co_x$

We used supercells with 16 atomic sites to describe the chemical disorder by means of averaging. The positions of the Fe and Co atoms in the supercell are randomized and 8 different supercells are used for calculating the MAE by averaging. The randomization was done by generating series of 16 random numbers via random.org [99] and then arrange the particular number of Fe or Co, which is listed in table 5.2.

Table 5.2: A $2 \times 2 \times 2$ supercell with 16 atoms.

Number of Fe atoms	Number of Co atoms	$Fe_{1-x}Co_x$
16	0	Fe
14	2	$Fe_{0.8750}Co_{0.1250}$
13	3	$Fe_{0.8125}Co_{0.1875}$
11	5	$Fe_{0.6875}Co_{0.3125}$
10	6	$Fe_{0.6250}Co_{0.3750}$
8	8	$Fe_{0.5000}Co_{0.5000}$
6	10	$Fe_{0.3750}Co_{0.6250}$
5	11	$Fe_{0.3125}Co_{0.6875}$
3	13	$Fe_{0.1875}Co_{0.8125}$
2	14	$Fe_{0.1250}Co_{0.8750}$
0	16	Co

A $2\times2\times2$ supercell for the B2 structure has the following atomic positions in direct coordinates:

```
 0.00  0.00  0.00
 0.00  0.00  0.50
 0.00  0.50  0.00
 0.00  0.50  0.50
 0.50  0.00  0.00
 0.50  0.00  0.50
 0.50  0.50  0.00
 0.50  0.50  0.50
 0.25  0.25  0.25
 0.25  0.25  0.75
 0.25  0.75  0.25
 0.25  0.75  0.75
 0.75  0.25  0.25
 0.75  0.25  0.75
 0.75  0.75  0.25
 0.75  0.75  0.75
```

These 16 atomic positions are than randomly rearranged 8 times for 8 different supercells. This rearrangement is done with random lists of 16 elements. To get the alloy concentrations listed in table 5.2, e.g. for the alloy $Fe_{0.1250}Co_{0.8750}$ one puts 2 Fe atoms in the first 2 positions and 14 Co atoms to the remaining positions. This way we can implement all the alloy concentrations shown in table 5.2.

In Figure 5.20 some supercells for the alloy $Fe_{0.1250}Co_{0.8750}$, which means 2 Fe and 14 Co atoms, are shown.

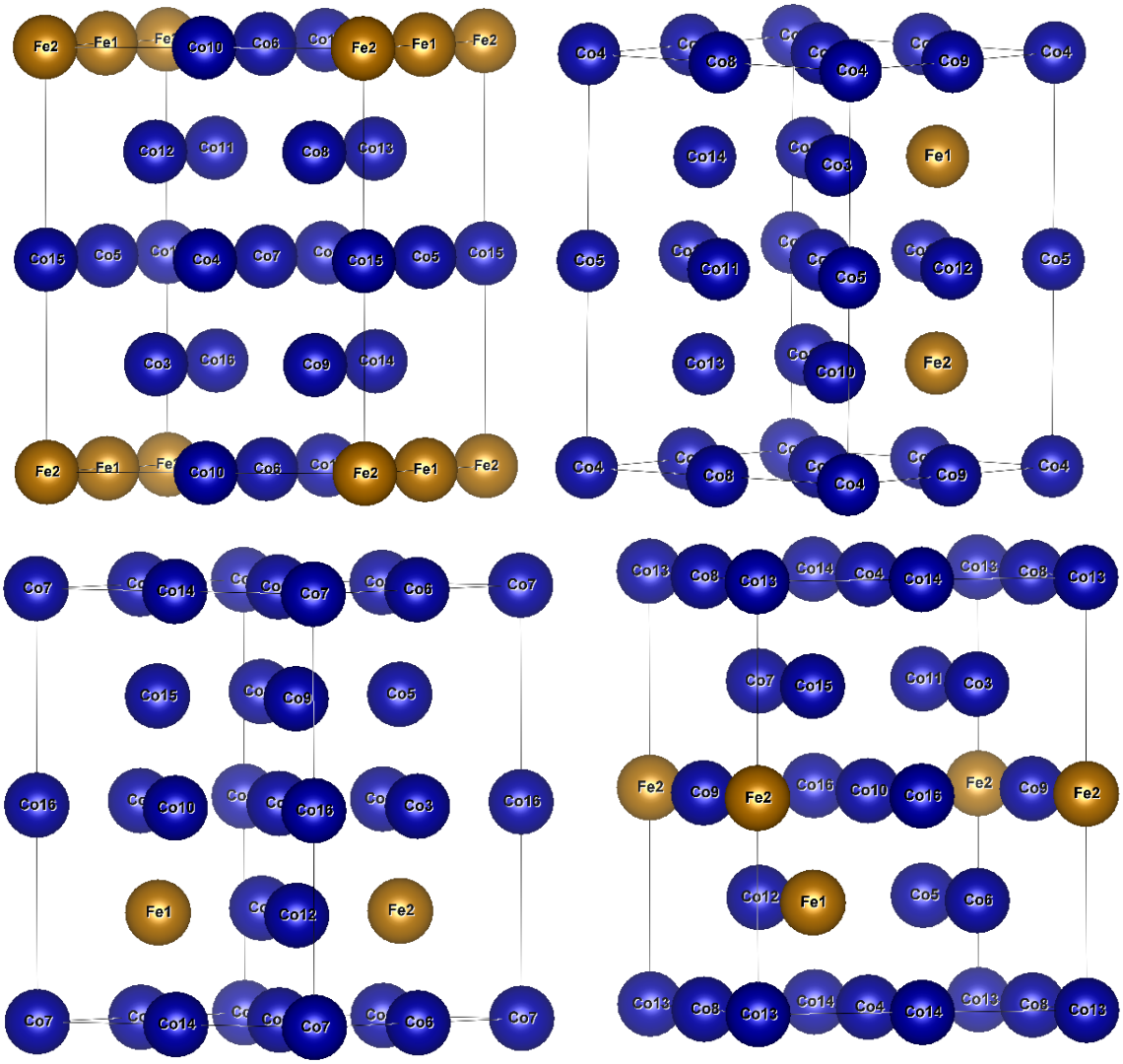

Figure 5.20: Four of our randomizations of the supercells for $Fe_{0.1250}Co_{0.8750}$, which means 2 Fe and 14 Co Atoms.

Chapter 6

Calculation of the magnetic anisotropy within the PAW method the case study of tetragonally distorted disordered alloys $Fe_{1-x}Co_x$

In this chapter the main output of this work is presented. The results of this chapter are submitted in a paper to the journal physical review B [100].
The magnetic anisotropy energy (MAE) of tetragonally distorted disordered alloys $Fe_{1-x}Co_x$ is calculated by two different virtual crystal approximation methods and an averaged supercell method within the projected augmented wave (PAW) methodology and the magnetic force theorem. We compare our results to recent coherent potential approximation (CPA), full potential linear combination of atom orbitals method calculations and to recent experiments. Good agreement between CPA and supercell averaging is found and discussed in detail.

6.1 Introduction

The magnetic anisotropy energy (MAE) of transition metal intermetallics and alloys is a key property defining the materials performance as a hard magnet as constituent of modern electronic memory devices [101, 102, 103, 104, 105]. With the development of highly efficient band structure codes extensive efforts have been made to calculate the magnetic anisotropy within the the local spin density approximation (LSDA) [19] and the corresponding generalized gradient approximation in various bulk, surface, and multilayer materials. In transition metal systems where the magnitude of the anisotropy is much smaller than in the rare-earths materials, the MAE appears only at second and higher orders of the perturbation expansion over the spin-orbit coupling (SOC) imposing stringent requirements for the computational accuracy. First-principles calculations of the MAE within a relativistic band structure theory based on LSDA were successful in d-transition metal based ferromagnetic multilayers [86, 106], surfaces and overlayers [107], low-dimensional nanostructures [108], and ad-atoms on the surfaces [109].

In these systems the MAE is two or three orders of magnitude larger than in the bulk elemental transition metals Fe, Ni and Co. However, for elemental cubic metals or hcp Co, were the MAE magnitude is of the order of few μeV/atom, the results of first-principles relativistic simulations are still very controversial [86, 110]. However, the LSDA calculations well predict the anisotropy in the ordered bulk alloys and in intermetallics where the anisotropy of the magnetic 3d-metal is enhanced due to for example lower crystal symmetry (e.g. tetragonal distortion) and/or another heavy element with strong SOC (e.g. Pt, Bi etc.).
One of the most prominent examples of the systems were the MAE has been extensively studied in the recent decades are the binary Fe-Co alloys. Since T. Burkert et al. [8] have shown from a first principles calculation a very strong anisotropy enhancement in these alloys due to tetragonal distortion, a number of studies has been done to investigate thin films of this material (see recent paper by E. Şaşıoğlu et al. [111], and references therein). On the basis of the calculations utilizing the Coherent Potential Approximation (CPA) [9] for disordered alloys in the framework of the Atomic Sphere Approximation (ASA), it has been shown, however, that the MAE in tetragonal FeCo significantly reduces as atomic disorder increases. Neise et al. [10] investigated the magnetic anisotropy in the distorted Fe-Co alloys using a full potential methodology in the framework of the Linear Combination of Atomic Orbitals methods (FPLO) [112]. To model the atomic disorder they used an averaging of the magnetic anisotropy calculated over the supercells with random distributions of Fe and Co atoms for three alloy compositions: $Fe_{1-x}Co_x$ with $x = 0.5$, $x = 0.625$ and $x = 0.75$. They also found that the atomic disorder leads to a decrease of the magnetic anisotropy compared to the atomically ordered alloys. Both methods CPA [9] and supercell averaging [10] predict the maximal MAE for the tetragonal distortion $\frac{c}{a}$ around 1.25 and for the Co concentration at compositions around $x = 0.6$. In both studies it has been demonstrated that the simple standard Virtual Crystal Approximation (VCA) gives a rather high value of the MAE compared to the more refined methods of treatment of the chemical disorder.
Although the CPA is often very successful for the description of the electronic structure of the disordered alloys it is an effective medium theory, which does not destroy the local symmetry around a given atomic site. Since the SOC on a given-atomic site may strongly depend on the symmetry of the local atomic environment of Fe or Co the MAE might be very sensitive on the way how alloy averaging is performed. The investigation of this topic is one of the issues of the present work. To compare the CPA-ASA results with averaging over supercells thoroughly, we investigate in this work a range of $Fe_{1-x}Co_x$ alloy compositions from $x = 0$ to $x = 1$. We will also compare the supercell averaging results for the MAE with the standard VCA [3, 4, 5, 6, 7] and a variant recently proposed [11]. This variant is not necessarily an improvement, but rather a convenient description within the PAW method.

6.2 Method

We use the VASP [2] within the projector augmented plane-wave (PAW) method [1, 113]. All calculations were performed using the PBE GGA [62] functional. The default energy cutoff of 280 eV was used. The k-point integration was done using the tetrahedron method with Blöchl

corrections [1].
The MAE was determined using the so called magnetic force theorem [85, 86], by running a fully self-consistent calculation for the collinear case and in the second step freezing the potential charge density for different orientations of the magnetization direction and then taking the energy differences, $K_u = E^{[100]} - E^{[001]}$, where $E^{[100]}$ and $E^{[001]}$ are the energies with the magnetization in the $[100]$ and $[001]$ directions of the bct structure respectively.
We achieve a convergence of the MAE energy of about 0.1 μeV/atom using 4096 k-points over the complete BZ for the VCA and VCA2 cases and 512 k-points for the SC. The convergence test has been performed for up to 32768 k-points for VCA and VCA2 and with 4096 k-points for the supercells.

6.3 Results and Discussion

The equilibrium lattice constants of the not distorted bcc $Fe_{1-x}Co_x$ alloys and magnetic moments of the fictitious atoms obtained with VCA calculations are presented in Figure 6.1. The corresponding unit cell volumes were used further in calculations of tetragonal bct structures with varying c/a ratios including supercell calculations. Interesting to note that the lattice constant is increasing up to the concentration $x = 0.2$ and then decreasing with increasing Co-concentration, which was shown in experiments [92]. A related tendency in the calculated values of the magnetic moment of the fictitious atom is observed. As we have discussed before , the increase in the volume is related to the majority d-states becoming fully occupied as the number of electrons is increased. Of course this increases the magnetic moment, and since the additionally occupied states are antibonding states the volume increases.

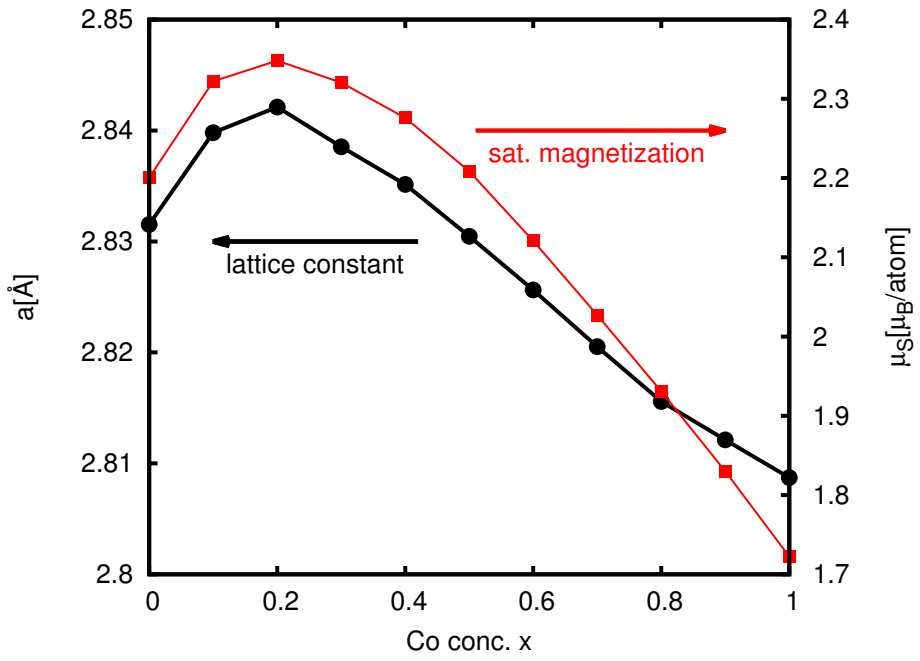

Figure 6.1: Left panel: calculated lattice constants, right panel: calculated total magnetic moment, as a function of the Co concentration x. The same trend has been shown experimentally in Ref. [92]

The dependence of the MAE of the bct alloy $Fe_{1-x}Co_x$ on the chemical composition and on the $\frac{c}{a}$-ratio is shown in Figure 6.2 calculated with VCA, VCA2 and the 16 atoms supercell models. Both VCA results are agreeing well with earlier VCA calculations [8, 10, 9]. The MAE has a maximum at about $x = 0.6$ and $\frac{c}{a} = 1.25$. There is no essential difference between VCA and VCA2 results. Although the VCA PAW value of the MAE at the maximum is somewhat smaller then in the TB-LMTO ASA calculations by Turek et al. [9], $K_u \approx 600$ μeV/atom vs. $K_u \approx 800$ μeV/atom respectively, it is still almost three times larger than the values obtained with more refined methods of chemical disorder treatment (CPA and supercell averaging). Since in this work we cover the whole range of the Fe-Co alloy concentrations we can conclude more on the general performance of the VCA methodology for the MAE calculations in disordered alloys. Indeed the VCA qualitatively well describes the trend of the MAE with the alloy concentration in Fe-Co (the physical reason for this is well described in the Ref. [9]). However, it largely overestimates the MAE value for almost all compositions, except the diluted Co rich regime ($x > 0.85$), see also figure (Figure 6.2(c)).

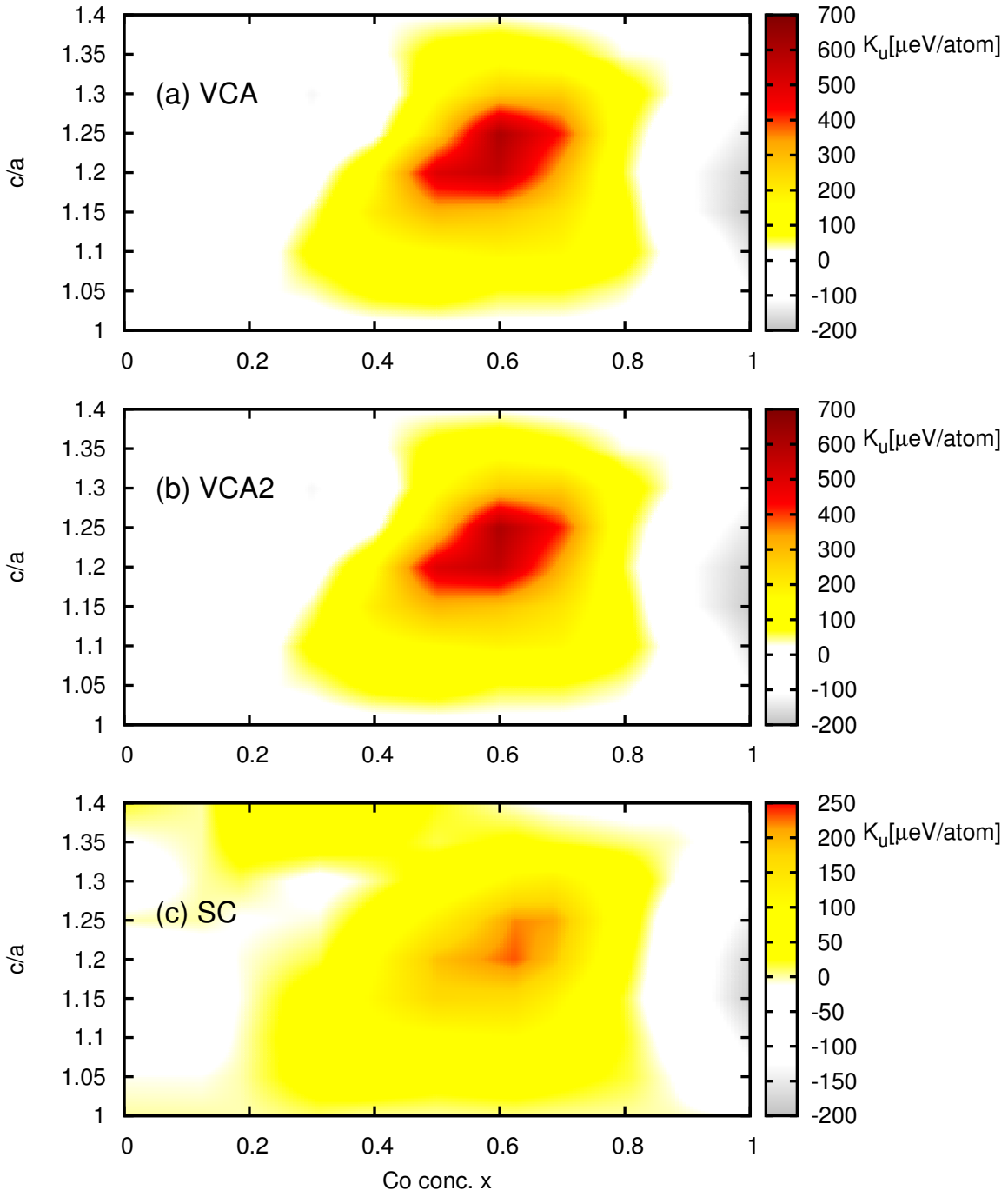

Figure 6.2: Calculated uniaxial MAE K_u of tetragonal $Fe_{1-x}Co_x$ as a function of the c/a-ratio and the Co concentration x. (a) VCA, (b) VCA2, and (c) supercell calculations.

More intriguing is the comparison of the CPA results by Turek et al. [9] and our supercell averaging. We get a close agreement in the position of the calculated MAE maximum with respect of the c/a ratio and the alloy concentration (around $\frac{c}{a} = 1.25$ and $x = 0.625$) between supercell PAW results and reported CPA calculations. The only difference is that the supercell PAW results give a more extended region of positive anisotropy (easy axis) towards the Co rich region. CPA gives positive MAE values in the range of $0.22 \leq x \leq 0.65$, whereas the supercell PAW have positive MAE values in the range $0.2 \leq x \leq 0.8$.
In Figure 6.3, we show the calculated MAE as a function of the concentration x for $\frac{c}{a} = 1.2$ and $\frac{c}{a} = 1.25$. We add on the figure also the results from VCA and CPA studies from Ref. [9] and available experimental results of $Fe_{0.5}Co_{0.5}$ on the $Pd(001)$ substrate [114] and $Fe_{0.36}Co_{0.64}$/Pt superlattice [106] for $\frac{c}{a} \approx 1.18$. We note the almost perfect agreement between the CPA and supercell averaged results. Some small numerical differences might be also related to the fact that the CPA results are derived in the ASA, since our VCA values and TB-LMTO VCA results of Ref. [9] show also some differences, that obviously cannot be ascribed to the difference in the model treatments of the atomic disorder. We also observe almost perfect agreement with the experimental results obtained for the MAE for films of tetragonally distorted Fe-Co grown on Pt and Pd substrates. This is also in-line with earlier full potential LCAO calculations by Neise et al. [10].

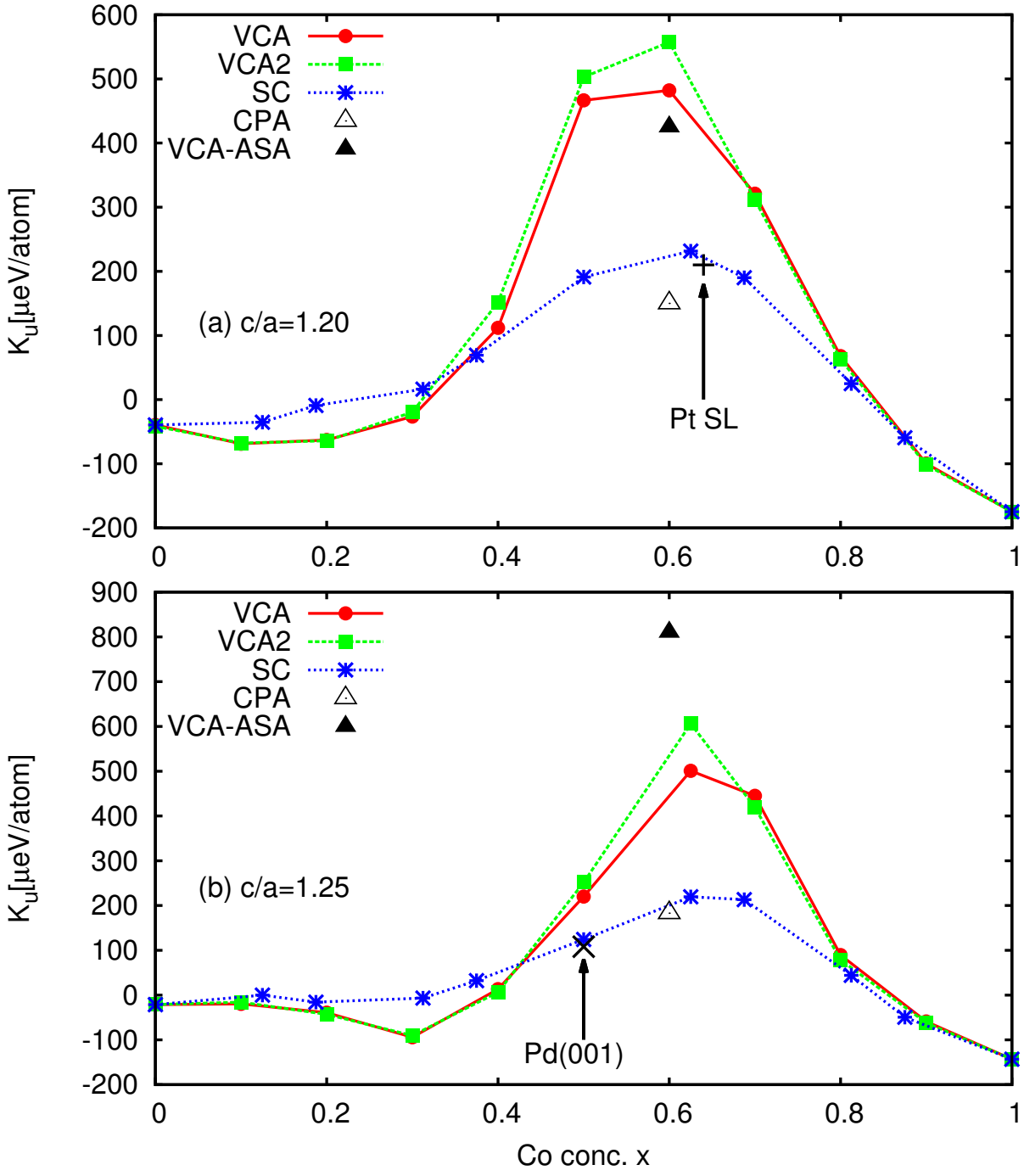

Figure 6.3: Calculated uniaxial MAE K_u of tetragonal $Fe_{1-x}Co_x$ as a function of the Co concentration x for VCA, VCA2 and the supercell. (a) Calculations for $\frac{c}{a} = 1.2$, the black plus sign denotes an experimental value obtained for $Fe_{0.36}Co_{0.64}$/Pt superlattice [106] for $\frac{c}{a} \approx 1.18$. (b) Calculations for $\frac{c}{a} = 1.25$, the black cross denotes an experimental value obtained for $Fe_{0.5}Co_{0.5}$ on $Pd(001)$ [114]. The filled triangle is a CPA calculation from Ref. [9], the white triangle indicates the VCA-ASA calculation also from Ref. [9].

Overall one might conclude that the simple supercell averaging scheme used in this work for the calculations of the MAE in disordered Fe-Co alloys in combination with the PAW as implemented in VASP performs very well compared to the experiments. The agreement with the CPA methodology is surprising but needs some further discussion. In Figure 6.4 we plot the values of the MAE calculated for the individual random supercells used in the averaging. One can see that in general the variation of the MAE values calculated for the individual random supercells around the average is not exceeding the difference between the CPA MAE and average supercell MAE. The main difference between CPA and average supercell results is caused, for this particular case, by one supercell (number 6), which has a significantly lower MAE than the rest of the supercells. Thus one would expect the good agreement between two methodologies (supercell averaging and CPA) only if the spread in the MAE is not to large. This condition is relatively well satisfied for concentrated alloy compositions but less for dilute ones. This might explain the deviation of our supercell averaging MAE from CPA results in the Co rich concentration regime.

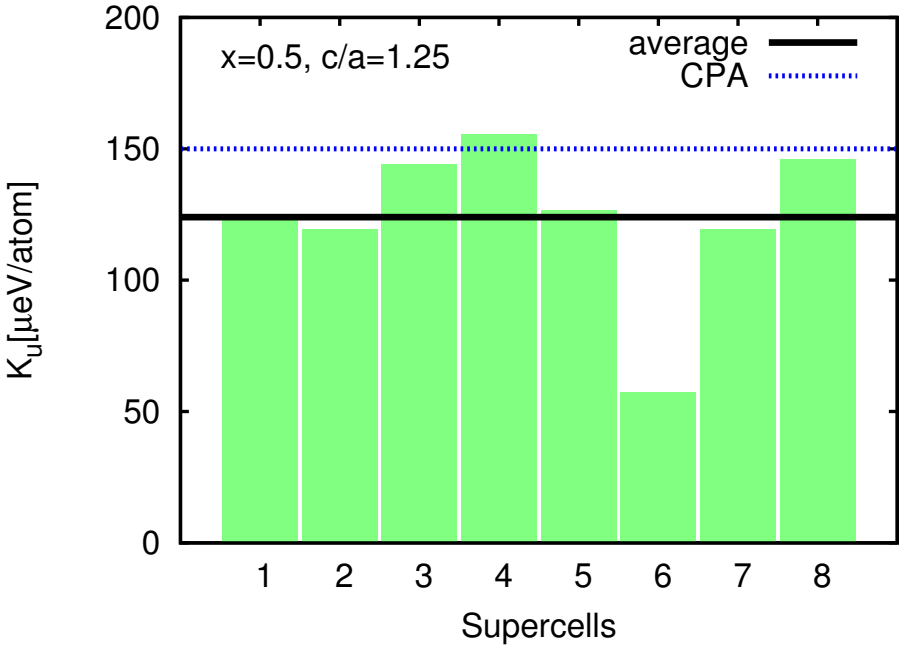

Figure 6.4: Calculated uniaxial MAE K_u for tetragonal $Fe_{0.5}Co_{0.5}$ and $\frac{c}{a} = 1.25$ with the 8 different random supercells. The black solid line denotes the average of the MAE of the supercells. The blue dashed line corresponds to CPA calculations done by Turek et al. [9] for $Fe_{0.5}Co_{0.5}$ and $\frac{c}{a} = 1.24$.

6.4 Summary

We can conclude that magnetic anisotropy energies derived within the PAW methodology with spin-orbit coupling as implemented in VASP are in good agreement with the results of other

full potential methods, and for Fe-Co, fairly well describe the experiments with tetragonally distorted thin films. For Fe-Co disordered alloys the simple averaging of the MAE calculated for randomly chosen supercells gives similar results as the calculations based on CPA, except at the dilute concentration limit.

Chapter 7

Néel theory of magnetic anisotropy

We want to fit our calculated data from the ab initio calculations for the different supercells to the model:

$$H_i = \frac{1}{2}\sum_{j=1}^{z_k}(\mathbf{s}_i \cdot \mathbf{e}_{ij})L_{ij}(\mathbf{r}_{ij}), \tag{7.1}$$

where z_k are the nearest neighbors of the Fe atoms in the supercell, $\mathbf{s}_i$ is the magnetization direction, which is either $\mathbf{s}_x$ or $\mathbf{s}_z$ (for a tetragonal supercell), the $\mathbf{e}_{ij} = \frac{\mathbf{r}_{ij}}{\|\mathbf{r}_{ij}\|}$ are the unit vectors to the corresponding nearest Fe neighbors. We consider only the Fe-Fe interactions. The $L_{ij}(\mathbf{r}_{ij})$ are the phenomenological parameters of the Néel model [13] that will be determined by our fitting, this Néel model was proposed for surface magnetic anisotropy, whereas we are using a slightly different setting and use the model for bulk magnetic anisotropy in a tetragonal supercell.
To calculate the L_{ij} we use the following expression:

$$H_x - H_z - \frac{2E_{\mathsf{Fe}}^{\mathsf{vasp}} + 14E_{\mathsf{Co}}^{\mathsf{vasp}}}{16} = E_{\mathsf{mae}}^{\mathsf{vasp}}, \tag{7.2}$$

H_x and H_z are the Néel anisotropy energies from (7.1), $E_{\mathsf{Fe}}^{\mathsf{vasp}}$ is the calculated MAE value for pure Fe, $E_{\mathsf{Co}}^{\mathsf{vasp}}$ is the calculated MAE value for pure Co and $E_{\mathsf{mae}}^{\mathsf{vasp}}$ is the calculated MAE for the supercell. With this expression, we can evaluate the different $L_{ij}(\mathbf{r}_{ij})$ parameters. These will than be used to calculate H_i energies with the Néel-model for the case of supercell with 3 Fe and 13 Co atoms. The fitting was done for a tetragonal cell with $\frac{c}{a} = 1.25$. This values can than be used to crosscheck the Néel-model for applicability in our case.
In order to accomplish this task not completely random supercell data were used. For 2 Fe and 14 in a 16 atom tetragonal supercell, only few symmetry inequivalent arrangements exist. We calculate all and determine from those the Néel parameters $L_{ij}(\mathbf{r}_{ij})$. This way all non equivalent Néel anisotropy parameters $L_{ij}(\mathbf{r}_{ij})$ can be calculated using equations (7.1) and (7.2).

Table 7.1: Non equivalent pseudo supercells, the calculated MAE of each supercell and the fitted Néel anisotropy parameters $L_{ij}(\mathbf{r}_{ij})$. Data and fitting for $\frac{c}{a} = 1.25$.

$\mathbf{r}_{ij}$ [in units of a and c]	VASP MAE [μeV]	fitted L_{ij} [μeV]
(001)	-57	72.5
(100)	-54	-38.5
(110)	-95	-174.5
(011)	-71	132
(101)	-70	334
(111)	-59	389
$(\frac{1}{2}\frac{1}{2}\frac{1}{2})$	-70	458

With the fitted Néel anisotropy parameters $L_{ij}(\mathbf{r}_{ij})$ we can now calculate with the equations (7.1) and (7.2) MAE values for the supercell with 3 Fe and 13 Co atoms, for all 8 randomized supercells.

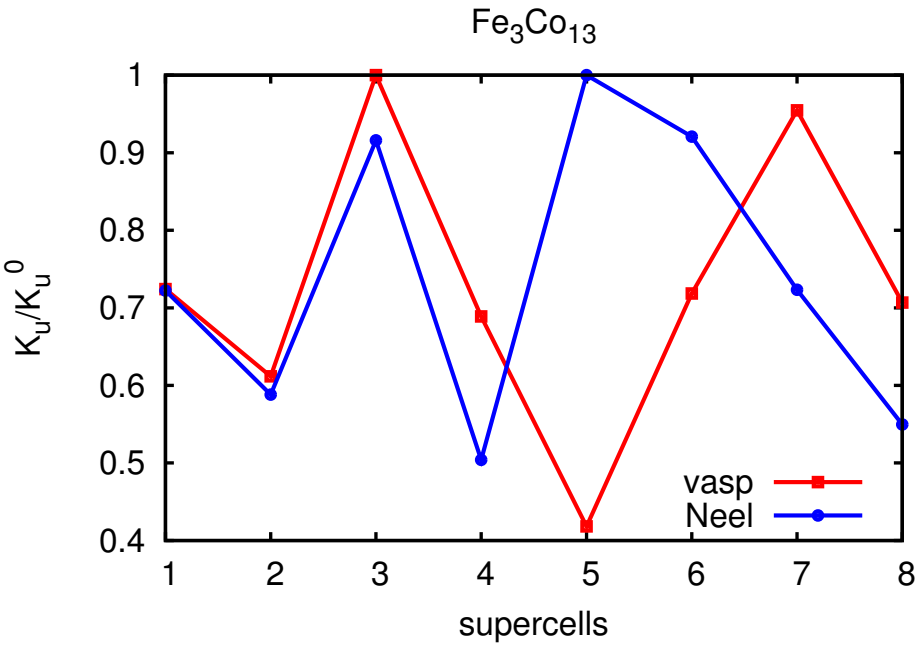

Figure 7.1: MAE values for the randomized supercells with 3 Fe and 13 Co atoms, which corresponds to the concentration of the alloy $Fe_{0.1875}Co_{0.8125}$. The red squares are the MAE values calculated with VASP and the the blue circles denote the results calculated with the Néel anisotropy parameters $L_{ij}(\mathbf{r}_{ij})$.

In the Figure 7.1 we show the results of the Néel model for the for the randomized supercells with 3 Fe and 13 Co atoms. The MAE values are normalized to one, so it is easier to match them. It can be seen that the agreement is good for the supercells $1, 2, 3$ and 4 but the supercell

5 is completely off with absolute error of 0.6. This is probably due to the fact that we only consider Fe-Fe interaction. One needs to beyond a simple pair model. In the next two pictures we show the results for randomized supercells with 5 Fe and 11 Co atoms and also results from the Fe rich case, namely the results for the randomized supercells with 14 Fe and 2 Co atoms.

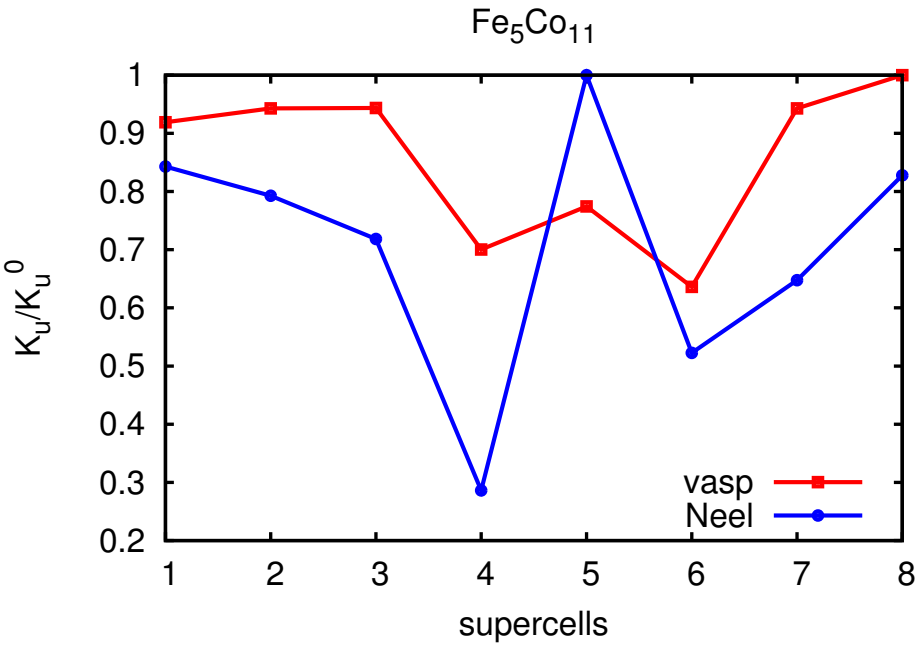

Figure 7.2: MAE values for the randomized supercells with 5 Fe and 11 Co atoms. The red squares are the MAE values calculated with VASP and the the blue circles denote the results calculated with the Néel anisotropy parameters $L_{ij}(\mathbf{r}_{ij})$.

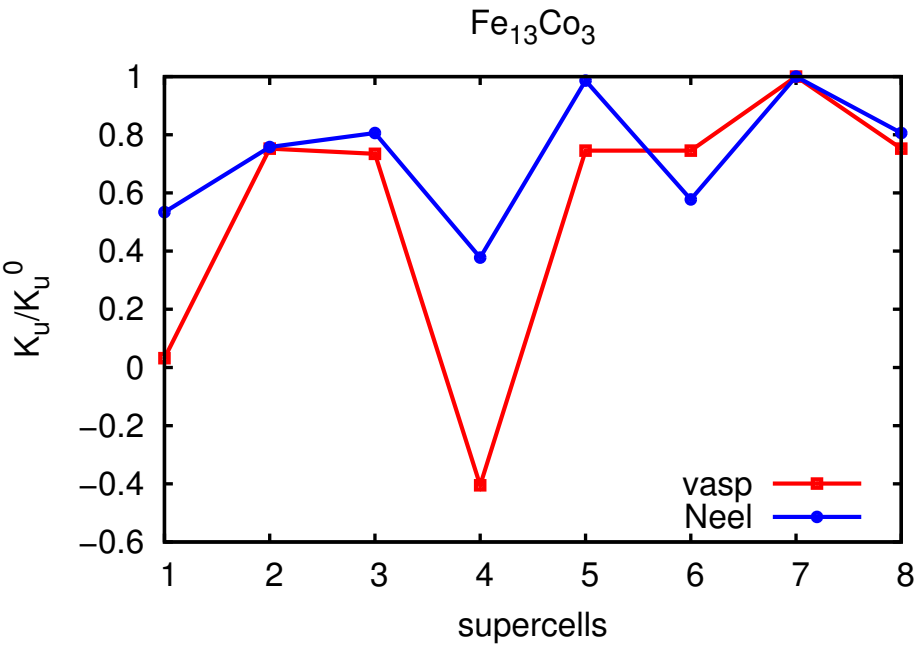

Figure 7.3: MAE values for the randomized supercells with with 13 Fe and 3 Co atoms, The red squares are the MAE values calculated with VASP and the the blue circles denote the results calculated with the Néel anisotropy parameters $L_{ij}(\mathbf{r}_{ij})$.

In Figure 7.2 we show the results for the alloy concentration $Fe_{0.3125}Co_{0.6875}$ (Fe_5Co_{11}) and in Figure 7.3 for the alloy concentration $Fe_{0.8125}Co_{0.1875}$ ($Fe_{13}Co_3$). We can clearly see that we have again a good agreement between the VASP calculated MAE values and the Néel anisotropy model, although we have only considered Fe-Fe interaction. But also in the case for Fe_5Co_{11} and $Fe_{13}Co_3$ are again outliners and they are the absolute error values are or even larger than for Fe_3Co_{13}.
A further improvement of the Néel model for the case of $Fe_{1-x}Co_x$ would be to add Co-Co interaction and Fe-Co interaction Néel parameters $L_{ij}(\mathbf{r}_{ij})$, so that:

$$H_i = \frac{1}{2}\sum_{i=1}^{z_i}(\mathbf{s}_i \cdot \mathbf{e}_{ij}) L_{ij}^{\text{Fe-Fe}}(\mathbf{r}_{ij}) L_{ij}^{\text{Co-Co}}(\mathbf{r}_{ij}) L_{ij}^{\text{Fe-Co}}(\mathbf{r}_{ij}). \tag{7.3}$$

With the improved Néel model in equation (7.3) it should be in principle possible to capture also the absolute values of the MAE. Overall we have done very well with equation (7.1), by capturing the trends of each supercell. The ion positions of all the 8 supercells are presented in the appendix.

Chapter 8

Outlook

The methods presented in this thesis could be used to investigate some other interesting systems. Some of them are presented here.

8.1 VCA and supercell simulation of the alloy $Fe_{1-x}Mn_xPt$

A very interesting alloy is the $L1_0$ FePt [115, 116, 117, 118] with high MAE values ([meV/f.u.]). A computationally not very demanding simulation would be VCA calculation of the alloy $Fe_{1-x}Mn_xPt$, calculating the MAE as a function of the Mn concentration for $0 \leq x \leq 0.25$. Additionally the alloying of FePt can be investigated with supercell calculations, the variation of the MAE with concentration and with tetragonal distortion. The dependence of the MAE on structural properties can be studied.

8.2 Supercell simulation of the alloy $Fe_{1-x}Si_x$

Supercell simulations of the alloy $Fe_{1-x}Si_x$, for $0 \leq x \leq 0.25$, and ordered structure calculations of $A2$, $B2$ and DO_3 structures for the compound Fe_3Si. Comparing all the results and finding out how the simulated disorder in the supercells describes the physical properties. Also very interesting are of course the magnetic properties and the MAE of $Fe_{1-x}Si_x$ [119, 120, 121, 122, 123].

8.3 Supercell simulation of the alloy $Fe_{1-x}Pd_x$

Supercell simulations of the alloy $Fe_{1-x}Pd_x$, for $0 \leq x \leq 0.25$, and ordered structure calculations of $L1_0$ structure for the compound FePd. FePd alloys are ferromagnetic, have remarkable mechanical properties and are also interesting for their magnetic anisotropy [124, 125, 126, 127, 128, 129].
In the case of $Fe_{1-x}Pd_x$, for $0 \leq x \leq 0.25$, also VCA simulations could be tried to describe the mechanical and magnetic properties.

8.4 Investigation of the spin arrangements in Ni_3Mn

There are still open questions concerning the ordered and disordered magnetic properties of Ni_3Mn [130, 131, 132, 133, 134, 135, 136, 137, 138, 139, 140].
With VASP the following calculations could be done: investigating the angle dependence of the antiferromagnetic spin coupling between Mn atoms at the Mn-sites and Mn-antisites in Ni_3Mn.

8.5 VCA simulations on $B2$ type Ni-Al alloys

In $B2$ type Ni-Al alloys are two atom-positions, an interesting question would be to alloy Co and Cu with VCA in both atom-positions and check the energies. Which position will be favored by Co and Cu? [141, 142].

Chapter 9

Conclusion

We have shown that it is possible to reach the required accuracy for magnetic anisotropy calculations within the VASP framework. This was done with the diluted disordered alloy $Fe_{1-x}Co_x$. We can conclude that magnetic anisotropy energies derived within the PAW methodology with spin-orbit coupling as implemented in VASP are in good agreement with the results of other full potential methods, and for Fe-Co, fairly well describe the experiments with tetragonally distorted thin films. For Fe-Co disordered alloys the simple averaging of the MAE calculated for randomly chosen supercells gives similar results as the calculations based on CPA, except at the dilute concentration limit. The results are well converged already with eight 16-atomic unit supercells.
We have also shown how to parametrize the VAPS magnetic anisotropy supercell data with the so called Néel magnetic surface anisotropy model (7.1). We have slightly extended this model to use for our supercell data. By just using Fe-Fe interaction we have shown, that it is possible to calculate the phenomenological Néel parameters and use them to recalculate magnetic anisotropy for supercells with different concentrations. Overall we have done very well with the slightly extended Néel model, by capturing the trends of each supercell.

Appendix A

Abbreviations & Symbols

A.1 Abbreviations

APW augmented plane wave

CPA coherent potential approximation

DFT density functional theory

SDFT spin density functional theory

EMTO exact muffin tin orbital

HBC hexa-*peri* hexabenzocoronene

KS Kohn-Sham

LMTO linear muffin tin orbital

MAE magnetic anisotropy energy

MBE molecular beam epitaxy

OFET organic field-effect transistor

OLED organic light emitting diode

PBE Perdew-Burke-Ernzerhof

PAW projector augmented plane-wave

SCF self consistent field

SBH Schottky barrier height

UHV ultra high vaccum

VCA virtual crystal approximation

VASP Vienna ab initio simulation package

A.2 Frequently Used Symbols

a_0 Bohr radius, $a_0 = \frac{4\pi\epsilon_0\hbar^2}{m_e e^2} = 0.529177$ Å

e elementary charge, $e = 1.60219 \times 10^{-19}$ C

m_e free electron mass, $m_e = 9.1095 \times 10^{-31}$ kg

m^* effective electron mass, $m^* = \hbar^2(\frac{d^2E}{dk^2})^{-1}$

s electron spin quantum number, $s = \frac{1}{2}$

$\frac{1}{2}\hbar$ electron spin angular momentum, $\frac{1}{2}\hbar = 5.273 \times 10^{-34}$ Js

g spin g-factor, $g = 2.0023$

k_B Boltzmann constant, $k_B = 1.38062 \times 10^{-23}$ J/K

E total energy

E_f Fermi energy

E_c conduction band edge

E_v valence band edge

f Fermi distribution/Fermi function $f(E) = \frac{1}{e^{\frac{E-E_f}{k_B T}}+1}$

k_i component of the wave vector parallel to the i-th axis ($i = x, y, z$)

N_A acceptor concentration

N_D donor concentration

eV_b (Schottky) barrier height (in eV).

Appendix B

Publications

B.1 Publications in Reviewed Journals within the Framework of this Thesis

- Soner Özcan, Sergii Khmelevskyi, Martijn Marsmann, Georg Kresse, "Calculation of the magnetic anisotropy with PAW method: the case study of tetragonally distorted disordered alloys $Fe_{1-x}Co_x$" submitted to *Phys. Rev. B*, x, xxx, (2016).

B.2 Other Publications by me

- H. Michor, T. Markota, I. M. Messner, S. Özcan, F. Schwarzböck, L Salamakha Z. S. Tako E. Bauer and O. Sologub,
"Ground state properties of $CeNi_{12}B_6$",
J. Phys: Conf. Ser. 592, 012043 2015

- Soner Özcan, Matteo Chiesa,
"Ballistic electron transport through Au/TiOPc/GaAs and Au/HBC/GaAs diodes", *International Journal of micro-nano scale transport*, 1, 171, 2010.

- S. Özcan, T. Khmelevska, S. Khmelevska and P. Mohn
"Site-preferences and local spin-polarization of transition metal solute atoms in B2 type Ni-Al alloys", *Intermetallics*, 14, 441, 2009.

- S. Özcan, J. Smoliner, M. Andrews, G. Strasser, T. Dienel and T. Fritz,
"Ballistic electron mean free path of titanylphthalocyanine films grown on GaAs",
phys. stat. sol. (c), 5, No. 1, $386-389$, 2008.

- S. Özcan, J. Smoliner, M. Andrews, G. Strasser, T. Dienel, R. Franke and T. Fritz,
"Ballistic Electron Attenuation Length in Titanylphthalocyanine films grown on GaAs",
Semicond. Sci. Technol., 23, 055008, 2008.

- S. Özcan, J. Smoliner, T. Dienel and T. Fritz,
"Temperature Dependent Schottky Barrier Height and Fermi Level Pinning on Au/H-BC/GaAs Diodes",
Appl. Phys. Lett., 92, 153309, 2008.

- S. Özcan, T. Roch, G. Strasser, J. Smoliner, R. Franke and T. Fritz,
"Ballistic Electron Emission Microscopy/Spectroscopy on Au/Titanylphthalocyanine/-GaAs Heterostructures",
J. Phys: Conf. Ser., 61, 1371, (2007).

- S. Özcan, J. Smoliner, M. Andrews, G. Strasser, T. Dienel, R. Franke and T. Fritz,
"Ballistic Electron Transport Through Titanylphthalocyanine films",
Appl. Phys. Lett., 90, 092107, selected for the "Virtual Journal of Nanoscale Science and Technology", March 12 (2007).

- M. El-Hagary, H. Michor, S. Özcan, M. Giovanni, A. Matar, Z. Heiba, P. Kerschl M. Schönhart, E. Bauer, R. Grössinger, G. Hilscher, J. Freudenberger and H. Rosner,
"Phase formation and ferrimagnetism of $GdCo_9Si_4$",
J. Phys.: Condens. Matter 18, 4567 2006

- R. Grössinger, M. Schönhart, M. El-Hagary, H. Michor, S. Özcan, M. Giovanni, A. Matar, Z. Heiba, P. Kerschl, E. Bauer, G. Hilscher, J. Freudenberger and H. Rosner,
"Phase formation and ferrimagnetism of $GdCo_{9-x}Si_{4+x}$",
J. Phys.: Conf. Ser. 51, 139 2006

- S. Özcan, T. Roch, G. Strasser, J. Smoliner, R. Franke and T. Fritz,
"Ballistic Electron Emission Microscopy/Spectroscopy on Au/Titanylphthalocyanine/-GaAs Heterostructures",
Proceedings of the GMe-Workshop, Vienna 13. 10. 2006 *,K. Riedling (Hrg.); (2006), SBN: 978-3-901578-17-5; S. 71 - 75.*.

- H. Michor, M. El-Hagary, S. Özcan, A. Horyn, E. Bauer, M. Reissner, G. Hilscher, S. Khmelevskyi, P. Mohn and P. Rogl,
"Weak itinerant ferromagnetism in YCo_9Si_4",
Physica B 359, 1177 2005

Appendix C

Curriculum Vitae

Dr. Soner Özcan

born: 03.03.1977
in: Çarşamba-Turkey
wife: Adrienn Zsiros
daughter: Emilia Özcan

- 1984 - 1987
  Primary school, Çarşamba-Turkey
- 1987 - 1988
  Primary school, Währingerstrasse 43, 1090 Wien
- 1988 - 1991
  After one year in the primary school, the teachers thought, that it would be better for me to change into a special school ("Sonderschule") for mentally retarded children. Without any justification actually!
  special school Anastasius-Grün-Gasse 10, 1180 Wien
- 1991 - 1992
  Middle school ("Hauptschule"), Leipziger Platz 1, 1200 Wien
- 1992 - 1997
  Several employers
  Bricklayer, Vienna
  Waiter, Vienna
  Windsurfing instructor, Marmaris-Turkey
  Windsurfing instructor, Lissabon-Portugal
- 1997 - 1998
  Austrian military service

- 1998 - 2001
  Several employers
  Waiter, Vienna
  Waiter, Geelong, Victoria-Australia

- 1999 - 2001
  High school diploma in second chance eduction.
  Externistenmatura, Oberstufenrealgymnasium Hegelgasse 14, 1010 Wien

- 10/2001 - 04/2005
  Diploma program in engineering physics, Vienna University of Technology
  Advisor: Prof. Dr. Herwig Michor and Prof. Dr. Gerfried Hilscher
  thesis title: Ferrimagnetismus in $GdCo_{9-x}Si_{4+x}$

- 05/2005 - 03/2006 (not finished)
  Doctoral studies in engineering, Vienna University of Technology
  Advisor: Prof. Dr. Mafred Deistler
  project: "Mathematical Modelling for Integrated Demand and Supply Chain Management"

- 03/2006 - 04/2008
  Doctoral studies in engineering, Vienna University of Technology
  Advisor: Prof. Dr. Jürgen Smoliner
  thesis title: "Ballistic Electron Emission Microscopy/Spectroscopy on Organic Semiconductors", completed with distinction

- 04/2008 - 03/2009
  Postdoc, Vienna University of Technology, Solid State Electronics Department

- 04/2009 - 02/2010
  Postdoc, MIST, Program of Material Science, Abu Dhabi-UAE

- 03/2010 - 12/2010
  IT-Consultant, Raiffeisen Bank International, Vienna

- 02/2011 - 10/2011
  IT-Consultant, Foxeye AG, Vienna-Linz-Frankfurt-Graz

- 02/2012 - 06/2012
  Postdoc, PUC-Rio, Rio de Janeiro-Brazil

- 01/2013 - 08/2014
  Vienna city school board (SSR-Wien), Mathematics and Physics teacher

- $09/2014$ - present
  Europaakademie Dr. Roland, Mathematics and Physics teacher, Vienna

- March 2013 - present
  Diploma program for the secondary teaching degree in Mathematics and Physics, University of Vienna
  thesis advisor: Prof. Dr. Georg Kresse
  title: "Hard and Soft Magnets and their Interfaces"

Appendix D

Positions of the 8 randomized supercells

The ion positions of the supercell 1:

```
  0.50   0.00   0.00  Fe
  0.00   0.00   0.00  Fe
  0.75   0.25   0.25  Co
  0.00   0.50   0.50  Co
  0.50   0.00   0.50  Co
  0.50   0.50   0.00  Co
  0.50   0.50   0.50  Co
  0.75   0.75   0.75  Co
  0.75   0.75   0.25  Co
  0.00   0.50   0.00  Co
  0.25   0.25   0.75  Co
  0.75   0.25   0.75  Co
  0.25   0.75   0.75  Co
  0.25   0.75   0.25  Co
  0.00   0.00   0.50  Co
  0.25   0.25   0.25  Co
```

The ion positions of the supercell 2:

```
  0.25   0.25   0.75
  0.75   0.75   0.75
  0.25   0.75   0.75
  0.75   0.75   0.25
  0.25   0.75   0.25
  0.50   0.50   0.50
  0.00   0.00   0.50
  0.00   0.50   0.50
  0.00   0.50   0.00
  0.25   0.25   0.25
  0.50   0.50   0.00
  0.75   0.25   0.25
  0.00   0.00   0.00
  0.50   0.00   0.50
  0.75   0.25   0.75
  0.50   0.00   0.00
```

The ion positions of the supercell 3:

```
  0.75   0.25   0.25
```

```
0.50    0.50    0.00
0.75    0.25    0.75
0.00    0.50    0.50
0.25    0.75    0.75
0.25    0.75    0.25
0.00    0.00    0.50
0.75    0.75    0.75
0.25    0.25    0.75
0.50    0.00    0.50
0.00    0.00    0.00
0.25    0.25    0.25
0.50    0.00    0.00
0.50    0.50    0.50
0.75    0.75    0.25
0.00    0.50    0.00
```

The ion positions of the supercell 4:

```
0.75    0.75    0.75
0.75    0.75    0.25
0.75    0.25    0.75
0.00    0.00    0.00
0.00    0.00    0.50
0.50    0.50    0.00
0.50    0.50    0.50
0.50    0.00    0.00
0.00    0.50    0.00
0.75    0.25    0.25
0.50    0.00    0.50
0.00    0.50    0.50
0.25    0.25    0.25
0.25    0.25    0.75
0.25    0.75    0.25
0.25    0.75    0.75
```

The ion positions of the supercell 5:

```
0.25    0.25    0.25
0.75    0.75    0.25
0.00    0.50    0.50
0.50    0.50    0.50
0.75    0.75    0.75
0.00    0.50    0.00
0.00    0.00    0.00
0.25    0.75    0.25
0.75    0.25    0.75
0.50    0.00    0.50
0.25    0.75    0.75
0.75    0.25    0.25
0.50    0.50    0.00
0.50    0.00    0.00
0.25    0.25    0.75
0.00    0.00    0.50
```

The ion positions of the supercell 6:

```
0.00    0.00    0.50
0.25    0.25    0.25
```

```
    0.50    0.00    0.00
    0.75    0.25    0.25
    0.25    0.75    0.25
    0.50    0.50    0.00
    0.75    0.75    0.25
    0.00    0.50    0.50
    0.50    0.50    0.50
    0.25    0.75    0.75
    0.75    0.25    0.75
    0.25    0.25    0.75
    0.00    0.50    0.00
    0.50    0.00    0.50
    0.75    0.75    0.75
    0.00    0.00    0.00
```

The ion positions of the supercell 7:

```
    0.25    0.25    0.25
    0.25    0.25    0.75
    0.75    0.25    0.25
    0.75    0.25    0.75
    0.25    0.75    0.25
    0.00    0.00    0.00
    0.50    0.50    0.00
    0.50    0.00    0.00
    0.50    0.50    0.50
    0.00    0.50    0.50
    0.50    0.00    0.50
    0.75    0.75    0.25
    0.25    0.75    0.75
    0.00    0.00    0.50
    0.75    0.75    0.75
    0.00    0.50    0.00
```

The ion positions of the supercell 8:

```
    0.75    0.25    0.25
    0.00    0.00    0.50
    0.75    0.75    0.75
    0.50    0.50    0.00
    0.25    0.75    0.25
    0.75    0.75    0.25
    0.25    0.25    0.75
    0.50    0.00    0.00
    0.50    0.00    0.50
    0.50    0.50    0.50
    0.25    0.75    0.75
    0.25    0.25    0.25
    0.00    0.00    0.00
    0.00    0.50    0.00
    0.75    0.25    0.75
    0.00    0.50    0.50
```

Appendix E

Additional code and scripts for running the calculations

E.1 Shell script for magnetic anisotropy VCA calculations

The following bash script is for a VCA calculation for the alloy $Fe_{0.8}Co_{0.2}$. For the other compositions only the corresponding POTCAR files have to be in the same directory and one needs to change the volume in the POSCAR file, because the volume is kept constant during the tetragonal distortion.

```
#!/bin/bash

#$ -N FeCo.2
#$ -pe ort* 32
#$ -q super.q

cat >KPOINTS <<!
Automatic mesh
0
G
16  16  16
0. 0. 0.
!

for i in 0.500 0.525 0.550 0.575 0.600 0.625 0.650 0.675 0.700
do cat >POSCAR <<!
bcc FeCo.2
-11.48
-0.5  0.5  $i
 0.5 -0.5  $i
 0.5  0.5 -$i
1
direct
0.00 0.00 0.00
!

# first calculation collinear
rm WAVECAR
rm CHGCAR
cat >INCAR <<!
PREC       = Accurate
LMAXMIX    = 4
```

```
ISMEAR     = -5
EDIFF      = 1E-6
GGA_COMPAT=.FALSE.
ISPIN      = 2
MAGMOM     = 3
!

~/bin/vasp
rm OUTCAR.FeCo.2.vca.rel.$i
cat POSCAR KPOINTS INCAR OUTCAR >>  OUTCAR.FeCo.2.vca.rel.$i
cp EIGENVAL EIGENVAL.FeCo.2.vca.rel.$i
cp DOSCAR DOSCAR.FeCo.2.vca.rel.$i
cp vasprun.xml vasprun.FeCo.2.vca.rel.$i.xlm

# first calculation in x-direction
rm WAVECAR
cat >INCAR <<!
PREC            = Accurate
LMAXMIX         = 4
ISMEAR          = -5
EDIFF           = 1E-6
GGA_COMPAT      =.FALSE.
LNONCOLLINEAR =.TRUE.
LSORBIT         = .TRUE.
MAGMOM          = 0 0 3
SAXIS           = 1 0 0 ;
ICHARG          = 11
LORBMOM         = .TRUE.
ISYM            = -1
!

~/bin/vasp
rm OUTCAR.FeCo.2.vca.rel.an.x.$i
cat POSCAR KPOINTS INCAR OUTCAR >> OUTCAR.FeCo.2.vca.rel.an.x.$i
cp EIGENVAL EIGENVAL.FeCo.2.vca.rel.an.x.$i
cp DOSCAR DOSCAR.FeCo.2.vca.rel.an.x.$i
cp vasprun.xml vasprun.FeCo.2.vca.rel.ab.x.$i.xlm

# second calculation in y-direction
rm WAVECAR
cat >INCAR <<!
PREC            = Accurate
LMAXMIX         = 4
ISMEAR          = -5
EDIFF           = 1E-6
GGA_COMPAT      =.FALSE.
LNONCOLLINEAR =.TRUE.
# perform calculations non collinear
LSORBIT         = .TRUE.
MAGMOM          = 0 0 3
SAXIS           = 0 1 0
ICHARG          = 11
LORBMOM         = .TRUE.
ISYM            = -1
!

~/bin/vasp
rm OUTCAR.FeCo.2.vca.rel.an.y.$i
cat POSCAR KPOINTS INCAR OUTCAR >> OUTCAR.FeCo.2.vca.rel.an.y.$i
cp EIGENVAL EIGENVAL.FeCo.2.vca.rel.an.y.$i
cp DOSCAR DOSCAR.FeCo.2.vca.rel.an.y.$i

# third calculation in z-direction
rm WAVECAR
cat >INCAR <<!
```

```
PREC            = Accurate
LMAXMIX         = 4
ISMEAR          = -5
EDIFF           = 1E-6
GGA_COMPAT      =.FALSE.
LNONCOLLINEAR =.TRUE.
# perform calculations non collinear
LSORBIT         = .TRUE.
MAGMOM          = 0 0 3
SAXIS           = 0 0 1
ICHARG          = 11
LORBMOM         = .TRUE.
ISYM            = -1
!

~/bin/vasp
rm OUTCAR.FeCo.2.vca.rel.an.z.$i
cat POSCAR KPOINTS INCAR OUTCAR >> OUTCAR.FeCo.2.vca.rel.an.z.$i
cp EIGENVAL EIGENVAL.FeCo.2.vca.rel.an.z.$i
cp DOSCAR DOSCAR.FeCo.2.vca.rel.an.z.$i
cp vasprun.xml vasprun.FeCo.2.vca.rel.ab.z.$i.xlm

done
```

E.2 Shell script for magnetic anisotropy VCA2 calculations

The following bash script is for a VCA2 calculation for the alloy $Fe_{0.8}Co_{0.2}$. For the other compositions the TAG VCA for the INCAR needs to be changed. And of course one needs to change the volume in the POSCAR file, because the volume is kept constant during the tetragonal distortion.

```
#$ -N FeCo.2
#$ -pe ort* 32
#$ -q super.q

#  VASP executable

for i in 0.500 0.525 0.550 0.575 0.600 0.625 0.650 0.675 0.700
do
cat >POSCAR <<!
bcc Fe
-11.87
-0.5   0.5   $i
 0.5  -0.5   $i
 0.5   0.5  -$i
1 1
direct
0.00  0.00  0.00
0.00  0.00  0.00
!
# first calculation non collinear
rm WAVECAR
cat >INCAR <<!
VCA          = 0.8  0.2
PREC         = Accurate
```

```
LMAXMIX      = 4
ISMEAR       = -5
EDIFF        = 1E-6
GGA_COMPAT   =.FALSE.
KPAR         = 8
ISPIN        = 2
MAGMOM       = 3 3
!

mpirun -np 32 ~/vasp
cat POSCAR KPOINTS INCAR OUTCAR >> OUTCAR.FeCo.2.vca2.rel.$i


# first calculation in x-direction
rm WAVECAR
cat >INCAR <<!
VCA              = 0.8 0.2
PREC             = Accurate
LMAXMIX          = 4
ISMEAR           = -5
EDIFF            = 1E-6
GGA_COMPAT       = .FALSE.
KPAR             = 8
LNONCOLLINEAR    = .TRUE.
# perform calculations non collinear
LSORBIT          = .TRUE.
MAGMOM           = 0 0 3 0 0 3
SAXIS            = 1 0 0
ICHARG           = 11
!

mpirun -np 32 ~/vasp
cat POSCAR KPOINTS INCAR OUTCAR >> OUTCAR.FeCo.2.vca2.rel.an.x.$i


# third calculation in z-direction
rm WAVECAR
cat >INCAR <<!
VCA              = 0.8 0.2
PREC             = Accurate
LMAXMIX          = 4
ISMEAR           = -5
EDIFF            = 1E-6
GGA_COMPAT       =.FALSE.
KPAR             = 8
LNONCOLLINEAR    =.TRUE.
# perform calculations non collinear
LSORBIT          = .TRUE.
MAGMOM           = 0 0 3 0 0 3
SAXIS           = 0 0 1
ICHARG           = 11
!

mpirun -np 32 ~/vasp
cat POSCAR KPOINTS INCAR OUTCAR >> OUTCAR.FeCo.2.vca2.rel.an.z.$i

done
```

E.3 Shell script for magnetic anisotropy supercell calculations

The following shell script is for the $Fe_{0.5}Co_{0.5}$ alloy, which means 8 Fe and 8 Co atoms. For the other compositions the scripts look similar, with only different number of atoms and different volume. For this script to work the supercells need to be stored in files named: pos_r1.dat for the randomization 1. These files are then read in with the cat command in grav quotes, otherwise the script gets just longer and unreadable! NOTE that these are grav quotes and not single quotes, there is a big difference in shell, Latex listing shows them as single quotes!

```
#$ -N FeCo.5
#$ -pe ort* 16
#$ -q super.q


for i in 2.0 2.1 2.2 2.3 2.4 2.5 2.6 2.7 2.8
do
for j in 1 2 3 4 5 6 7 8 9
do

cat >POSCAR <<!
FeCo.5
-181.44
   2.0   0.0   0.0
   0.0   2.0   0.0
   0.0   0.0   $i
8 8
Direct
`cat pos_r$j.dat`
!

# first calculation collinear
cat >INCAR <<!
PREC          = Accurate
LMAXMIX       = 4
ISMEAR        = -5
EDIFF         = 1E-6
GGA_COMPAT    =.FALSE.
KPAR          = 4
ISPIN         = 2
MAGMOM        = 16*3
ISYM          = -1
!

rm WAVECAR
rm CHGCAR
mpirun -np 16 ~/vasp
cat POSCAR KPOINTS INCAR OUTCAR >> OUTCAR.FeCo.5.sc.rel.an.lorb.r$j.$i


# first calculation in x-direction
cat >INCAR <<!
PREC          = Accurate
LMAXMIX       = 4
ISMEAR        = -5
EDIFF         = 1E-6
GGA_COMPAT    =.FALSE.
KPAR          = 4
ISYM          = -1
LNONCOLLINEAR =.TRUE.
```

```
# perform calculations non collinear
LSORBIT          = .TRUE.
MAGMOM           = 0 0 3 0 0 3 0 0 3 0 0 3 0 0 3 0 0 3 0 0 3 0 0 3 0 0 3 0 0 3 0 0 3 0 0 3 0
     0 3 0 0 3 0 0 3 0 0 3 0 0 3 0 0 3
SAXIS            = 1 0 0
ICHARG           = 11
LORBMOM          = .TRUE.
!

rm WAVECAR
mpirun -np 16 ~/vasp
cat POSCAR KPOINTS INCAR OUTCAR >> OUTCAR.FeCo.5.sc.rel.an.lorb.x.r$j.$i
cp EIGENVAL EIGENVAL.FeCo.5.sc.rel.an.lorb.x.r$j.$i
cp DOSCAR DOSCAR.FeCo.5.sc.rel.an.x.lorb.r$j.$i



# third calculation in z-direction
rm WAVECAR
cat >INCAR <<!
PREC             = Accurate
LMAXMIX          = 4
ISMEAR           = -5
EDIFF            = 1E-6
GGA_COMPAT       =.FALSE.
KPAR             = 4
ISYM             = -1
LNONCOLLINEAR    =.TRUE.
# perform calculations non collinear
LSORBIT          = .TRUE.
MAGMOM           = 0 0 3 0 0 3 0 0 3 0 0 3 0 0 3 0 0 3 0 0 3 0 0 3 0 0 3 0 0 3 0 0 3 0 0 3 0
     0 3 0 0 3 0 0 3 0 0 3 0 0 3 0 0 3
SAXIS            = 0 0 1
ICHARG           = 11
LORBMOM          = .TRUE.
!

rm WAVECAR
mpirun -np 16 ~/vasp
cat POSCAR KPOINTS INCAR OUTCAR >> OUTCAR.FeCo.5.sc.rel.an.lorb.z.r$j.$i
cp EIGENVAL EIGENVAL.FeCo.5.sc.rel.an.lorb.z.r$j.$i
cp DOSCAR DOSCAR.FeCo.5.sc.rel.an.lorb.z.r$j.$i


done
done
```

E.4 Fermi surface script

```

#!/bin/bash
KPOINTS1=16
KPOINTS2=16
KPOINTS3=16

# from this band on
BANDNUMBER=4
# the bands for FS
BANDS_x=4
```

```
# all the bands in the eigenval file
NBANDS=10
# 2 for spin up and 3 for spin down
SPIN=2

if [ $SPIN == "2" ]
then
 OUTPUT="FS_spin_up.bxsf"
 > $OUTPUT
fi

if  [ $SPIN == "3" ]
then
 OUTPUT="FS_spin_down.bxsf"
 > $OUTPUT
fi

echo "BEGIN_INFO"
echo "BEGIN_INFO" >> $OUTPUT

Efermi=`grep E-fermi OUTCAR | cut -c14-20`

echo "  Fermi Energy:" $Efermi
echo "  Fermi Energy:" $Efermi >> $OUTPUT
echo "END_INFO"
echo "END_INFO" >> $OUTPUT
echo "" >> $OUTPUT

echo "BEGIN_BLOCK_BANDGRID_3D"
echo "BEGIN_BLOCK_BANDGRID_3D" >> $OUTPUT
echo "   one_word_comment"
echo "   one_word_comment" >> $OUTPUT
echo "   BEGIN_BANDGRID_3D"
echo "   BEGIN_BANDGRID_3D" >> $OUTPUT

echo "   " $BANDS_x
echo "   " $KPOINTS1 " " $KPOINTS2 " " $KPOINTS3
echo "   0 0 0"

echo "   " $BANDS_x >> $OUTPUT
echo "   " $KPOINTS1 " " $KPOINTS2 " " $KPOINTS3  >> $OUTPUT
echo "   0 0 0" >> $OUTPUT

awk '\
{while(getline == 1)\
 {if($1=="direct" && $2=="lattice" && $3=="vectors" && $4=="reciprocal" && $5=="lattice")\
  {getline ; \
   print $4 " " $5 " " $6 ;\
   getline ; \
   print $4 " " $5 " " $6 ;\
   getline ; \
   print $4 " " $5 " " $6 ;\
   exit 2 \
  }\
 }   \

}\
' < OUTCAR

awk '
{while(getline == 1)\
 {if($1=="direct" && $2=="lattice" && $3=="vectors" && $4=="reciprocal" && $5=="lattice")\
  {getline ; \
   print $4 " " $5 " " $6 ;\
   getline ; \
```

```
    print $4 " " $5 " " $6 ;\
    getline ; \
    print $4 " " $5 " " $6 ;\
    exit 2 \
  }\
 }   \

}\
' < OUTCAR >> $OUTPUT

echo "BAND " $BANDNUMBER >> $OUTPUT
if [ $SPIN == "2" ]
then
 awk ' BEGIN {
    getline; getline; getline; getline; getline; getline; getline; getline;
    }
    {while(getline == 1)
    {while($1<'$NBANDS')
     {getline;
      if($1=='$BANDNUMBER'){print $2}
     }
    }
}' < EIGENVAL >> $OUTPUT
fi

if [ $SPIN == "3" ]
then
 awk ' BEGIN {
   getline; getline; getline; getline; getline; getline; getline; getline;
      }
      {while(getline == 1)
    {while($1<'$NBANDS')
  {getline;
   if($1=='$BANDNUMBER'){print $3}
  }
    }
    }' < EIGENVAL >> $OUTPUT
fi


##############################################
BANDNUMBER=$((BANDNUMBER +1))
echo "" >> $OUTPUT
echo "BAND " $BANDNUMBER >> $OUTPUT

if [ $SPIN == "2" ]
then
 awk ' BEGIN {
   getline; getline; getline; getline; getline; getline; getline; getline;
      }
      {while(getline == 1)
    {while($1<'$NBANDS')
  {getline;
   if($1=='$BANDNUMBER'){print $2}
  }
    }
    }' < EIGENVAL >> $OUTPUT
fi


if [ $SPIN == "3" ]
then
 awk ' BEGIN {
   getline; getline; getline; getline; getline; getline; getline; getline;
      }
```

```
      ␣     {while(getline == 1)
142 ␣     {while($1<'$NBANDS')
  ␣␣{getline;
144 ␣␣ if($1=='$BANDNUMBER'){print $3}
  ␣␣}
146 ␣     }
                }' < EIGENVAL >> $OUTPUT
148 fi
  ##########################################
150

152 ##########################################
  BANDNUMBER=$((BANDNUMBER +1))
154 echo "" >> $OUTPUT
  echo "BAND " $BANDNUMBER >> $OUTPUT
156
  if [ $SPIN == "2" ]
158 then
  ␣awk ' BEGIN {
160 ␣␣␣getline; getline; getline; getline; getline; getline; getline; getline;
      ␣␣     }
162       ␣     {while(getline == 1)
  ␣     {while($1<'$NBANDS')
164 ␣␣{getline;
  ␣␣ if($1=='$BANDNUMBER'){print $2}
166 ␣␣}
  ␣     }
168 ␣     }' < EIGENVAL >> $OUTPUT
  fi
170

172 if [ $SPIN == "3" ]
  then
174 ␣awk ' BEGIN {
  ␣␣␣getline; getline; getline; getline; getline; getline; getline; getline;
176       ␣     }
      ␣     {while(getline == 1)
178 ␣     {while($1<'$NBANDS')
  ␣␣{getline;
180 ␣␣ if($1=='$BANDNUMBER'){print $3}
  ␣␣}
182 ␣     }
                }' < EIGENVAL >> $OUTPUT
184 fi
  ##########################################
186

188 ##########################################
  BANDNUMBER=$((BANDNUMBER +1))
190 echo "" >> $OUTPUT
  echo "BAND " $BANDNUMBER >> $OUTPUT
192
  if [ $SPIN == "2" ]
194 then
  ␣awk ' BEGIN {
196 ␣␣␣getline; getline; getline; getline; getline; getline; getline; getline;
      ␣␣     }
198       ␣     {while(getline == 1)
  ␣     {while($1<'$NBANDS')
200 ␣␣{getline;
  ␣␣ if($1=='$BANDNUMBER'){print $2}
202 ␣␣}
  ␣     }
204 ␣     }' < EIGENVAL >> $OUTPUT
  fi
```

```
206
208 if [ $SPIN == "3" ]
    then
210 awk ' BEGIN {
    getline; getline; getline; getline; getline; getline; getline; getline;
212         }
            {while(getline == 1)
214 {while($1<'$NBANDS')
    {getline;
216  if($1=='$BANDNUMBER'){print $3}
    }
218 }
                }' < EIGENVAL >> $OUTPUT
220 fi
    ###############################################
222


224
    echo "" >> $OUTPUT
226 echo "  END_BANDGRID_3D" >> $OUTPUT
    echo "END_BLOCK_BANDGRID_3D" >> $OUTPUT
```

Bibliography

[1] P. E. Blöchl, *Physical Review B* **50**, 17953 (1994).

[2] G. Kresse and J. Furthmüller, *Phys. Rev. B* **54**, 11169 (1996).

[3] S. de Gironcoli, P. Giannozzi, and S. Baroni, *Phys. Rev. Lett* **66**, 2116 (1991).

[4] N. Marzari, S. de Gironcoli, and S. Baroni, *Phys. Rev. Lett* **72**, 4001 (1994).

[5] A. M. Saitta, S. de Gironcoli, and S. Baroni, *Phys. Rev. Lett* **80**, 4939 (1998).

[6] D. Papaconstantopoulos and W. Pickett, *Phys. Rev. B* **57**, 12751 (1998).

[7] W. E. Pickett and D. Singh, *Phys. Rev. B* **53**, 1146 (1996).

[8] T. Burkert, L. Nordström, O. Eriksson, and O. Heinonen, *Phys. Rev. Lett.* **93**, 027203 (2004).

[9] I. Turek, J. Kudrnovský, and K. Carva, *Phys. Rev. B* **86**, 174430 (2012).

[10] C. Neise, S. Schönecker, M. Richter, K. Koepernik, and H. Eschrig, *Phys. Status Solidi B* **248**, 2398 (2011).

[11] L. Bellaiche and D. Vanderbilt, *Phys. Rev. B* **61**, 7877 (2000).

[12] I. Turek, V. Drchal, V. Kudrnovský, M. Šob, and P. Weinberger, *Electronic Structure of Disordered Alloys Surfaces and Interfaces*, MA: Kluwer, 1996.

[13] L. Néel, *Comptes rendus hebdomadaires des séances de l' Académie des sciences* **237**, 1468 (1953).

[14] L. H. Thomas, *Proc. Cambridge Philos. Soc.* **23**, 542 (1927).

[15] E. Fermi, *Z. Phys.* **48**, 73 (1928).

[16] L. H. Thomas, *Proc. Cambridge Philos. Soc.* **26**, 376 (1930).

[17] E. P. Wigner, *Phys. Rev.* **46**, 1002 (1934).

[18] P. Hohenberg and W. Kohn, *Phys. Rev.* **136B**, 864 (1964).

[19] W. Kohn and L. J. Sham, *Phys. Rev.* **140A**, 1133 (1965).

[20] E. Lewars, *Computational Chemistry: Introduction to the Theory and Applications of Molecular and Quantum Mechanics*, Kluwer Academia Publishers, 2003.

[21] A. Whitaker, *Einstein, Bohr and the Quantum Dilemma*.

[22] D. Z. Albert, *Quantum Mechanics and Experience*.

[23] D. Bohm and H. B. Hiley, *The Undivided Universe*.

[24] J. Baggot, *The Meaning of Quantum Theory*.

[25] M. Jammer, *The Philosophy of Quamtum Mechanics*.

[26] R. F. W. Bader, *Atoms in Molecules*.

[27] M. Cardano and L. Ley, *Photoemission in Solids* 1, 2*; Topics Apll. Phys. Vols.* 26, 27, Springer, Heidelberg New York, 1979.

[28] B. Feueracher, B. Fitton, and R. F. Willis, *Photoemission and the Electronic Properties of Surfaces*, Wiley, New York, 1978.

[29] R. Courths and S. Hüfner, *Phys. Rep.* **112**, 55 (1994).

[30] H. Lüth, G. W. Rubloff, and W. D. Grobmann, *Solid. State. Commun.* **18**, 1427 (1975).

[31] H. Lüth, *Solid Surfaces, Interfaces and Thin Films, 4th ed.*, Springer, Berlin Heidelberg, 2001.

[32] W. J. Kaiser and L. D. Bell, *Phys. Rev. Lett.* **60**, 1408 (1988).

[33] L. D. Bell and W. J. Kaiser, *Phys. Rev. Lett.* **61**, 2368 (1988).

[34] S. Özcan, J. Smoliner, M. Andrews, G. Strasser, T. Dienel, and T. Fritz, *Appl. Phys. Lett.* **90**, 092107 (2007).

[35] S. Özcan, T. Roch, G. S. J. Smoliner, R. Franke, and T. Fritz, *J. Phys.: Conf. Ser.* **61**, 1371 (2007).

[36] S. Özcan, J. Smoliner, M. Andrews, G. Strasser, T. Dienel, and T. Fritz, *phys. stat. sol. (c)* **5**, 386 (2008).

[37] S. Özcan, J. Smoliner, A. M. Andrews, G. Strasser, T. Dienel, R. Franke, and T. Fritz, *Semicond. Sci. Technol.* **23**, 055008 (2008).

[38] S. Özcan, J. Smoliner, T. Dienel, and T. Fritz, *Appl. Phys. Lett.* **92**, 153309 (2008).

[39] H. Ibach and H. Lüth, *Festkörperphysik, Einführung in die Grundlagen*, Springer-Verlag, Berlin Heidelberg New York, 2002.

[40] C. Kittel, *Einführung in die Festkörperphysik*, Oldenburg Verlag, München Wien, 2002.

[41] G. P. Shusterman and A. J. Shusterman, *J. Chem. Educ.* **74**, 771 (1997).

[42] R. G. Paar and W. Yang, *Density Functional Theory of Atoms and Molecules*.

[43] W. J. Hehre, L. Radom, P. v. R. Schleyer, and J. A. Pople, *Ab initio Molecular Orbital Theory*.

[44] A. D. Becke, *J. Chem. Phys.* **88**, 1053 (1988).

[45] T. M. Klapötke and A. Schulz, *Quantenmechanische Methoden in der Hauptgruppenchemie*, Spektrum, 1995.

[46] W. Koch and M. C. Holthausen, *A Chemist's Guide to density functional theory*, Wiley, 2001.

[47] E. Engel and R. M. Dreizler, *Theoretical and mathematical physics: density functional theory, an advanced course*, Springer, Berlin Heidelberg, 2010.

[48] H. Eyring, J. Walter, and G. E. Kimbell, *Density functional theory: a practical introduction*, Wiley, 2009.

[49] H. H. Schmidtke, *Quantenchemie*, VCH Weinheim, 1994.

[50] H. Eyring, J. Walter, and G. E. Kimbell, *Quantum chemistry*, Wiley, New York, 1954.

[51] D. R. Hartree, *Proc. Cambridge Philos. Soc.* **24**, 89 (1927).

[52] V. Fock, *Z. Phys.* **61**, 126 (1930).

[53] C. C. J. Roothaan, *Rev. Mod. Phys.* **23**, 69 (1951).

[54] G. G. Hall, *Proc. Royal. Soc.* **205**, 541 (1951).

[55] D. R. Hartree, *Calculation of atomic structures*, Wiley, New York, 1957.

[56] V. Tschinke and T. Ziegler, *J. Chem. Phys.* **11**, 8051 (1990).

[57] J. K. Klabowski, *Density Functional Methods of Electronic Structure Theory*.

[58] I. N. Levine, *Quantum Chemistry, 5th edn.*

[59] A. D. Becke, *Int. J. Quantum Chem.* **23**, 1915 (1989).

[60] H. Stoll, E. Golka, and H. Preuss, *Theor. Chim. Acta.* **49**, 143 (1978).

[61] R. G. Paar and W. Yang, *Annu. Rev. Phys. Chem.* **46**, 701 (1995).

[62] J. P. Perdew, K. Burke, and M. Ernzerhof, *Phys. Rev. Lett.* **77**, 3865 (1996).

[63] G. Kresse, *Optimierte normerhaltende Pseudopotentiale*, Master thesis, Technische Universität Wien, 1990.

[64] J. Furthmüller, *Parameterfreie Berechnungen der elektronischen Struktur von Festkörpern: Anwendungen auf Chalkogenidstörstellen in Silizium*, PhD thesis, Universität Stuttgart, 1991.

[65] G. Kresse, *Ab-initio Molekular Dynamik für flüssige Metalle*, PhD thesis, Technische Universität Wien, 1993.

[66] G. Kresse and J. Furthmüller, *Comput. Mat. Sci.* **6**, 15 (1996).

[67] U. Barth and L. Hedin, *J. Phys. C: Solid State Phys.* **5**, 1629 (1972).

[68] K. Burke, J. P. Perdew, M. Levy, J. Seminario, and P. Politzer, *Modern Density Functional Theory: A Tool for Chemistry*, Elsevier, 1995.

[69] Wien2k, `http://www.wien2k.at/index.html`.

[70] W. Greiner, *Theoretische Physik Band* 4*, Quantenmechanik: Teil* 1 *Einführung*, Verlag Harri Deutsch, 1992.

[71] W. Greiner, *Theoretische Physik Band* 4 *A, Quantentheorie: Spezielle Kapitel*, Verlag Harri Deutsch, 1993.

[72] W. Greiner, *Theoretische Physik Band* 5*, Quantenmechanik: Teil* 2 *Symmetrien*, Verlag Harri Deutsch, 1990.

[73] H. A. Bethe and E. E. Salpeter, *Quantum Mechanics of One- and Two-Electron Atoms, Dover Edition*, Dover Publications, INC., 2008.

[74] J. M. D. Coey, *Magnetism and Magnetic Materials*, Cambridge University Press, Cambridge, 2011.

[75] P. Mohn, *Magnetism in the Solid State, An Introduction*, Springer Verlag, Berlin Heidelberg New York, 2003.

[76] C. wen Chen, *Magnetism and Metallurgy of Soft Magnetic Materials*, Dover Publications, 1986.

[77] R. R. Birss, *Series of Monographs on Selected Topics in Solid State Physics: Symmetry and Magnetism*, North Holland Publishing Company, 1964.

[78] B. Barbara, D. Gignoux, and C. Vettier, *Lectures on Modern Magnetism*, Science Press, 1964.

[79] E. Kneller, *Ferromagnetismus*, Springer-Verlag, 1962.

[80] J. M. D. Coey, *Lecture Notes for Magnetism and Magnetic Materials*, 2015.

[81] G. Mahajani, *Trans. roy. Soc. Lond.* **228 A**, 83 (1929).

[82] N. S. Akulov, *Z. Phys.* **54**, 582 (1929).

[83] W. P. Mason, *Phys. Rev.* **96**, 302 (1954).

[84] C. Guillaud, *Ann. Phys. Paris* **4**, 671 (1949).

[85] A. I. Lichtenstein, M. I. Katsnelson, V. P. Antropov, and V. A. Gubanov, *J. Magn. Magn. Mater.* **67**, 65 (1987).

[86] G. Daalderop, P. Kelly, and M. Schuurmans, *Phys. Rev. B* **44**, 12054 (1991).

[87] F. D. Murnaghan, *Proc. Natl. Acad. Sci. USA* **30**, 244 (1944).

[88] F. Birch, *Phys. Rev.* **71**, 809 (1947).

[89] `http://periodictable.com/Elements/011/data.html`.

[90] A. Kokalj, *J. Mol. Graphics Modelling* **17**, 176 (1999).

[91] A. Kokalj, *Comp. Mater. Sci.* **28**, 155 (2003).

[92] I. Ohnuma, H. Enoki, O. Ikeda, R. Kainuma, H. Ohtani, B. Sundman, and K. Ishida, *Acta Mat.* **50**, 379 (2002).

[93] T. Nishizawa and K. Ishida, *Massalski TB, editor. Binary alloy phase diagrams, vol. 2, 2nd ed*, AMS International, 1990.

[94] D. I. Bardos, *J. Appl. Phys.* **40**, 1371 (1969).

[95] F. T. Philipp Haas and P. Blaha, *Phys. Rev. B* **79**, 085104 (2009).

[96] L. Pauling, *General Chemistry*, Dover Publications, INC., 1970.

[97] J. A. Rayne and B. S. Chandrasekhar, *Phys. Rev.* **122**, 1714 (1961).

[98] K. Schwarz, P. Mohn, P. Blaha, and J. Kübler, *J. Phys. F: Met. Phys.* **14**, 2659 (1984).

[99] `http://random.org`.

[100] S. Özcan, S. Khmelevskyi, M. Marsmann, and G. Kresse, *Phys. Rev. B* **xx**, xx (2016).

[101] D. Weller and A. Moser, *IEEE Trans. on Magn.* **35**, 4423 (1999).

[102] D. Weller, A. Moser, L. Folks, M. Best, W. Lee, M. Toney, M. Schwickert, J. Thiele, and M. Doerner, *IEEE Trans. on Magn.* **36**, 10 (2000).

[103] R. Skomski, P. Manchanda, P. K. Kumar, B. Balamurugan, A. Kashyap, and D. J. Sellmyer, *IEEE Trans. on Magn.* **49**, 3215 (2013).

[104] H. M. Bertram, H. Zhou, and R. Gustafson, *IEEE Trans. on Magn.* **34**, 1845 (1998).

[105] S. H. Charap, P.-L. Lu, and Y. He, *IEEE Trans. on Magn.* **33**, 978 (1997).

[106] G. Andersson, T. Burkert, P. Warnicke, M. Björck, B. Sanyal, C. Chacon, C. Zlotea, L. Nordström, P. Nordblad, and O. Eriksson, *Phys. Rev. Lett.* **96**, 037205 (2006).

[107] B. Ujfalussy, L. Szunyogh, P. Bruno, and P. Weinberger, *Phys. Rev. Lett* **77**, 1805 (1996).

[108] A. B. Shick, F. Maca, and P. M. Oppeneer, *Phys. Rev. B* **69**, 212410 (2004).

[109] P. Blonski, A. Lehnert, S. Dennler, S. Rusponi, M. Etzkorn, G. Moulas, P. Bencok, P. Gambardella, H. Brune, and J. Hafner.

[110] M. D. Stiles, S. V. Halilov, R. A. Hyman, and A. Zangwill, *Phys. Rev. B* **64**, 104430 (2001).

[111] E. Şaşioğlu, C. Friedrich, and S. Blügel, *Phys. Rev. B* **87**, 020410(R) (2013).

[112] K. Koepernik and H. Eschrig, *Phys. Rev. B* **59**, 1743 (1999).

[113] G. Kresse and D. Joubert, *Physical Review B* **59**, 1758 (1999).

[114] F. Luo, X. Fu, A. Winkelmann, and M. Przybylski, *Appl. Phys. Lett.* **91**, 262512 (2007).

[115] T. Burkert, O. Eriksson, S. Simak, A. Ruban, B. Sanyal, L. Nordström, and J. Wills, *Phys. Rev. B* **71**, 1 (2005).

[116] C. J. Aas, L. Szunyogh, J. S. Chen, and R. W. Chantrell, *Appl. Phys. Lett.* **99**, 132501 (2011).

[117] Y. Kota and A. Sakuma, *App. Phys. Lett.* **111**, 07A310 (2012).

[118] J. B. Staunton, S. Ostanin, S. Razee, B. Gyorffy, L. Szunyogh, B. Ginatempo, and E. Bruno, *J. Phys. Cond. Matter* **16**, S5623 (2004).

[119] A. K. Arzhnikov, L. V. Dobysheva, G. N. Konygin, E. V. Voronina, and E. P. Yelsukov, *Phys. Rev. B* **65**, 024419 (2001).

[120] T. Khmelevska, S. Khmelevskyi, a. V. Ruban, and P. Mohn, *Journal of Physics: Condensed Matter* **18**, 6677 (2006).

[121] N. E. Sluchanko, V. V. Glushkov, S. V. Demishev, A. A. Menovsky, L. Weckhuysen, and V. V. Moshchalkov, *Phys. Rev. B* **65**, 064404 (2002).

[122] I. I. Pronin, M. V. Gomoyunova, D. E. Malygin, D. V. Vyalikh, Y. S. Dedkov, and S. L. Molodtsov, *J. Appl. Phys.* **104**, 104914 (2008).

[123] Chattopadhyay, S. B. Roy, and S. Chaudhary, *Phys. Rev. B* **65**, 132409 (2002).

[124] C. Issro, M. Abed, W. Püschl, B. Sepiol, W. Pfeifler, P. F. Rogl, G. Schmerber, W. A. Soffa, R. Kazubski, and V. Pierron-Bohnes, *Metallurgical and Materials Trans. A* **37A**, 3415 (2006).

[125] L. Szunyogh, J. Zabloudil, A. Vernes, P. Weinberger, B. Újfalussy, and S. Sommers, *Phys. Rev. B* **63**, 184408 (2001).

[126] S. Bahmida, A. Fnidiki, A. Laggoun, and A. Guittoum, *J. Magn. Magn. Mater.* **392**, 139 (2015).

[127] T. Mehaddene, V. Pierron-Bohnes, M. Zemirli, R. Caudron, K. Tanaka, and H. Numakura, *Journal of Alloys and Compounds* **378**, 294 (2004).

[128] J. Buschbeck, I. Opahle, S. Fähler, L. Schultz, and M. Richter, *Phys. Rev. B* **77**, 174421 (2008).

[129] A. Boufelfel, R. M. Emrick, and C. M. Falco, *Phys. Rev. B* **43**, 13152 (1991).

[130] J. Kudrnovský, V. Drchal, I. Turek, S. Khmelevskyi, J. K. Glasbrenner, and K. D. Belashchenko, *Phys. Rev. B* **86**, 144423 (2012).

[131] J. W. Cable, R. M. Nicklow, and Y. Tsunoda, *Phys. Rev. B* **36**, 5311 (1987).

[132] D. Iotova, N. Kioussis, and S. P. Lim, *Phys. Rev. B* **54**, 14413 (1996).

[133] V. V. Kokorin, S. M. Konoplyuk, A. E. Perekos, and Y. S. Semenova, *J. Magn. Magn. Mater.* **321**, 782 (2009).

[134] M. J. Macinkowski and N. Brown, *J. Appl. Phys.* **32**, 375 (1961).

[135] S. Khmelevskyi, A. B. Shick, and P. Mohn, *Phys. Rev. B* **83**, 224419 (2011).

[136] A. Paoletti, F. P. Ricci, and L. Passari, *J. Appl. Phys.* **37**, 3236 (1966).

[137] A. Paciaroni, C. Petrillo, and F. Sacchetti, *Phys. Rev. B* **52**, 3049 (1995).

[138] G. Mazzone, C. Petrillo, F. Sacchetti, and M. Scafi, *Phys. Rev. B* **46**, 11665 (1992).

[139] G. Mazzone, C. Petrillo, and F. Sacchetti, *Phys. Rev. B* **49**, 4307 (1994).

[140] D. Spišák and J. Hafner, *J. Phys.: Condens. Matter* **11**, 6359 (1999).

[141] S. Özcan, T. Khmelevska, S. Khmelevskyi, and P. Mohn, *Intermetallics* **17**, 441 (2009).

[142] H. Wei, J. J. Liang, B. Z. Sun, P. Peng, Q. Zhend, X. F. S. M. S. Dargusch, and X. Yao, *Intermetallics* **18**, 1062 (2010).